



Gran Sasso Science Institute
Scuola Internazionale Superiore di Studi Avanzati



Direct Measurements of the $^{23}\text{Na}(p,\gamma)^{24}\text{Mg}$ Cross Section at Stellar Energies

PhD thesis

submitted October 30, 2016

PhD Candidate

Axel Boeltzig

Advisors

Matthias Junker
Laboratori Nazionali del Gran Sasso

Michael Wiescher
University of Notre Dame

Tutors

Gianluca Imbriani
Università di Napoli

Andreas Best
Università di Napoli

Gran Sasso Science Institute

Ciclo XXIX – A.A 2013-2016

Abstract

Asymptotic Giant Branch (AGB) stars play a fundamental role in the determination of the observed abundances of light mass elements in the universe. In spite of great efforts, model predictions for the abundance of nuclides in AGB stars are rather uncertain due to the complex physical processes in the star. The lack of precise cross-section data, for the relevant proton capture reactions in particular, worsens the reliability of the model predictions for light element yields.

The reaction $^{23}\text{Na}(p, \gamma)^{24}\text{Mg}$ links the NeNa and the MgAl cycles of stellar burning, and is active in stars that burn at the highest temperatures (such as AGB stars), or in explosive scenarios. This link between the two cycles, in competition with the reaction $^{23}\text{Na}(p, \alpha)^{20}\text{Ne}$, makes the reaction rate of $^{23}\text{Na}(p, \gamma)^{24}\text{Mg}$ a relevant input parameter, whose precise knowledge is important for the determination of the abundances of – for example – neon, sodium, magnesium and aluminum.

The subject of this work is an experiment for direct cross section measurements of $^{23}\text{Na}(p, \gamma)^{24}\text{Mg}$ at LUNA, the Laboratory Underground for Nuclear Astrophysics. The location of this experiment, underground at the Gran Sasso National Laboratory (LNGS) allows gamma ray measurements with greatly enhanced sensitivity.

In the first chapter of this thesis, a brief introduction to nuclear astrophysics is given, with a focus on the experimental aspects of direct cross section measurement. The current knowledge about $^{23}\text{Na}(p, \gamma)$ in view of astrophysics is summarized in this chapter. Chapter two describes the experimental setup for the experiment, from the accelerator to the used detector setups. The third chapter presents the detector characterization in more detail, including Monte Carlo simulations and detector calibration. Chapter four exposes the measurements and their analyses, starting with the development and experimental study of sodium targets, and coming to the measurements with the two detector setups. The final chapter of this work discusses the possible implications on the $^{23}\text{Na}(p, \gamma)^{24}\text{Mg}$ reaction rate from the current results, and gives an outlook about the next steps and future experimental work to further improve the knowledge about this reaction.

Contents

1	Introduction	1
1.1	Stellar Evolution	1
1.2	Nuclear Astrophysics	2
1.3	Direct Cross Section Measurements	5
1.4	Experimental Challenges and Low-background Physics	7
1.5	$^{23}\text{Na}(p,\gamma)^{24}\text{Mg}$: Astrophysics and State of the Art	8
2	Setup	13
2.1	The LUNA Facility	13
2.2	Solid Target Setup at LUNA	13
2.3	HPGe Detector	15
2.4	Bismuth Germanium Oxide (BGO) Detector Setup	18
2.5	Limitations and Complementarity of the Detector Setups	21
2.6	Shielding	24
3	Detector Characterization	27
3.1	Methods	27
3.2	BGO Backgrounds	29
3.3	BGO Detector	35
3.4	HPGe Detector	37
4	Data Acquisition and Analysis	45
4.1	Sodium Target Development and Studies	45
4.2	HPGe Phase Analysis	62
4.3	BGO Phase Analysis	75
5	Conclusions	87
5.1	Results	87
5.2	Astrophysical Reaction Rates	88
5.3	Outlook	91

1 Introduction

1.1 Stellar Evolution

The variety of chemical elements in the universe originates in stars. Only hydrogen, helium and (to less extent) lithium are amongst the stable nuclides that were produced in the course of big bang nucleosynthesis. Hydrogen and helium still are by far the most abundant elements in the universe and serve as the main starting material for the formation of stars. When a star begins to form by gravitational attraction of stellar material, the gravitational energy liberated during the contraction of the material leads to an increase in temperature. When the temperature at the core of the forming star reaches several MK, first fusion reactions start to occur. The first major fusion process to set in is hydrogen burning, which creates helium from hydrogen in a multi-step process that can be summarized as $4\ ^1\text{H} \rightarrow\ ^4\text{He} + 2\ e^+ + 2\ \nu_e$. With the energy liberated in this process, hydrogen burning acts as a source of energy in the star. Eventually the gravitational energy from the contraction of the stellar material, which played the important role of initially heating the star's interior, is replaced by hydrogen burning as the main energy source in the star. The star then reaches a hydrostatic equilibrium (between thermal pressure and gravitational pull) and thermal equilibrium (as the energy created in the core is radiated away from the surface of the star).

Except for the very lightest stars that do not reach the required temperature to ignite the hydrogen burning process, hydrogen burning characterizes the first major phase in the life of a star and can be considered the transition from a "protostar" to a star. The further evolution of any star depends on its mass and its composition. In later stages in the life of stars of greater mass, helium burning and fusion processes involving heavier elements can be activated, thus creating more elements of higher mass numbers. Multiple processes can be at work at the same time in different parts of the star, which can be divided into its core and a number of shells that are characterized by different nuclear processes. The shells may, however, interact and exchange material by convection and mixing processes.

Two observable characteristics of a star are its luminosity (the radiative power it emits) and the effective surface temperature that determines the color of the star. A plot of these quantities against each other (the Hertzsprung-Russel diagram) for the stars observed in the universe reveals characteristic bands and clusters, corresponding to stars with similar properties. The development of a star in the course of its lifetime

1 Introduction

can be traced in this diagram, where stars start on the “zero age main sequence” after hydrogen burning sets in, and then proceed in characteristic curves. The precise curve characterizes the development of an individual star, passing through different phases of its life cycle.

One of the characteristic regions in the Hertzsprung-Russel diagram is the Asymptotic Giant Branch (AGB). This region is reached in the late life of stars with masses of between 0.6 and 10 solar masses. At this stage, the stars are characterized by an inert core of mostly carbon and oxygen surrounded by shells of helium and hydrogen. Helium and hydrogen burning occurs in these shells, and a complex interplay between the two shells is observed [1]. The intricate processes in AGB stars are believed to lend a major role in the enrichment of heavier elements in the interstellar medium to these stars.

The evolution of each star is closely tied to the nuclear reactions which serve as its energy source. Nuclear astrophysics studies the nuclear processes that are one of the foundations of the macroscopic evolution of a star. Amongst the goals of nuclear astrophysics are the detailed understanding of the evolution of stars (from their initial properties), and of the creation of the elements beyond helium in their abundances that are observed in the galaxy. Introductions and overviews of the field of nuclear astrophysics can be found in the books [2] and [3].

1.2 Nuclear Astrophysics

In this section the basic principles of nuclear reactions between charged particles are summarized, and the calculation of the rates of these reactions is introduced.

The nuclear cross sections of reactions between two positively charged particles, such as $^{23}\text{Na}(p, \gamma)^{24}\text{Mg}$, are strongly influenced by the Coulomb repulsion of the particles that increases with decreasing distance between the two particles. In a classical picture a nuclear reaction can only occur when the distance between these particles falls below the range of the nuclear force, where attraction dominates. Outside the range of the nuclear force, the electrostatic potential between the two particles creates the “Coulomb barrier”, which has to be overcome for a reaction to occur. If the center of mass energy of the particles is lower than the Coulomb barrier, a reaction between the particles would be forbidden in the frame of classical physics. The quantum mechanical “tunnel effect”, however, allows also particles with smaller energies to penetrate the Coulomb barrier, so that a nuclear reaction is also possible at lower energies. For s-wave processes, the tunneling probability as a function of energy is given by:

$$P(E) = \exp(-2\pi\eta) \tag{1.1}$$

Where the Sommerfeld parameter η is defined as:

$$\eta = \frac{Z_1 \cdot Z_2 \cdot e^2}{4\pi\epsilon_0 \cdot \hbar \cdot v} \quad (1.2)$$

Here Z_1 and Z_2 are the atomic charges of the two particles, and v is their relative (classical) velocity. Hence the tunneling probability is $P(E) \propto \exp(-Z_1 \cdot Z_2/\sqrt{E})$. In addition to the tunneling probability, the cross section typically shows a $1/E$ energy dependence. Hence for energies below the Coulomb barrier, the cross section drops off sharply at decreasing energies. The definition of the astrophysical S -factor yields a quantity that is linked to the cross section, but varies much more slowly with energy:

$$S(E) = E \cdot e^{2\pi\eta(E)} \cdot \sigma(E) \quad (1.3)$$

In an astrophysical scenario that is characterized by a temperature T , the particle energies follow a Maxwell-Boltzmann distribution. This energy distribution is asymmetric, peaks at $k_B \cdot T/2$ (with the Boltzmann constant K_B) and falls off in a long tail towards higher energies. As seen above, the tunneling probability increases rapidly with energy. These two opposing trends result in an energy region in which the probability for a reaction is the largest. This region is called the ‘‘Gamow peak’’, and is illustrated in Figure 1.1. Below this region the reaction probability is suppressed by the low chance to tunnel through the Coulomb barrier, at higher energies the smaller number of particles at these energies is the limiting factor for the probability to create a reaction between the two particles.

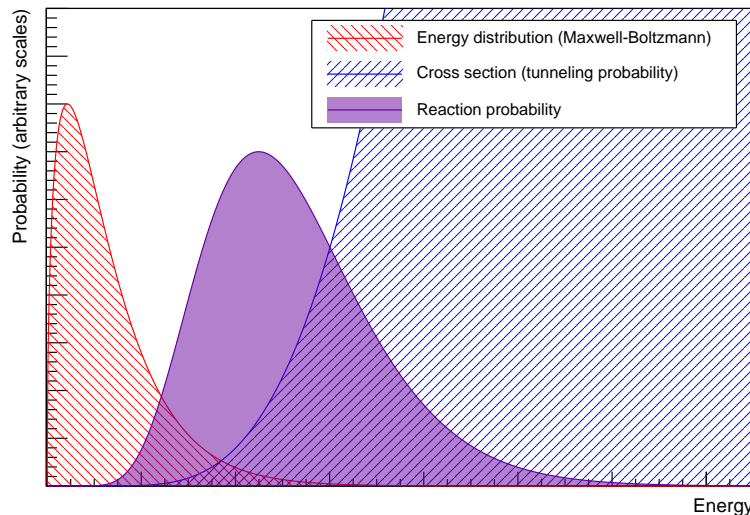


Figure 1.1: Illustration of the ‘‘Gamow peak’’ as a product of Maxwell-Boltzmann energy distribution and cross section (tunneling probability).

1 Introduction

The reaction rate r_{01} is the number of reactions per unit volume and unit time between two particles “0” and “1”. It is a key quantity in any model of stellar processes, as it determines the rate at which particle species are created and destroyed, and the power that is created by this reaction. It is calculated as:

$$r_{01} = N_0 \cdot N_1 \cdot \langle \sigma v \rangle_{01} \quad (1.4)$$

Where N_0 and N_1 are the particle densities of the two species and $\langle \sigma v \rangle_{01}$ is determined by the velocity distribution of the particles and the reaction cross section:

$$\langle \sigma v \rangle_{01} = \sqrt{\frac{8}{\pi} \cdot \frac{m_0 + m_1}{m_0 \cdot m_1} \cdot \frac{1}{(k_B \cdot T)^3}} \cdot \int_0^{\infty} E \cdot \sigma(E) \cdot \exp\left(-\frac{E}{k_B \cdot T}\right) dE \quad (1.5)$$

As can be seen from these considerations, a precise knowledge of the cross section $\sigma(E)$ is crucial to derive the reaction rates and thus describe the dynamics of the nuclear processes in a star for a given environment. In case of a cross section that is purely given by direct capture, the cross section in the energy window of the Gamow peak is most crucial for the uncertainty of the reaction rate determination.

In general, however, also resonances in the cross section $\sigma(E)$ can have a significant influence on the reaction rate or may even dominate the reaction rate completely. The cross section of a single resonance at an energy $E_{\text{res.}}$ in the reaction between two distinct particles 0 and 1 is described by the Breit-Wigner formula:

$$\sigma_{\text{BW}}(E) = \frac{\lambda^2}{4\pi} \cdot \frac{(2J + 1)}{(2j_0 + 1) \cdot (2j_1 + 1)} \cdot \frac{\Gamma_{\text{entrance}} \cdot \Gamma_{\text{exit}}}{(E_{\text{res.}} - E)^2 + \Gamma_{\text{total}}^2/4} \quad (1.6)$$

Where λ is the de Broglie wavelength, J is the spin of the resonance, j_0 and j_1 are the spins of the two particles. Γ_{entrance} and Γ_{exit} are the partial width of the channels, and Γ_{total} is the total width of the resonance. If the total width of the resonance is large (i. e. the resonance is broad), also the energy-dependence of the partial widths has to be taken into account.

If the total width of the resonance is small so that the partial widths and the factor $\exp(-E/k_B \cdot T)$ can be approximated as constant over the width of the resonance, the strength of this narrow resonance can be characterized by the quantity $\omega\gamma$:

$$\omega\gamma = \underbrace{\frac{2J + 1}{(2j_0 + 1)(2j_1 + 1)}}_{\omega} \cdot \underbrace{\frac{\Gamma_{\text{entrance}} \cdot \Gamma_{\text{exit}}}{\Gamma_{\text{total}}}}_{\gamma} \quad (1.7)$$

With the definition of this resonance strength $\omega\gamma$, the reaction rate corresponding to

the narrow resonance can be calculated analytically and yields the expression:

$$\langle\sigma v\rangle_{01} = \left(\frac{2\pi}{k_{\text{B}}T} \cdot \frac{m_0 + m_1}{m_0 \cdot m_1}\right)^{\frac{3}{2}} \cdot \hbar^2 \cdot \exp\left(-\frac{E_{\text{res.}}}{k_{\text{B}}T}\right) \cdot \omega\gamma \quad (1.8)$$

The total cross section for a given reaction is the result of the contributions from the non-resonant component, narrow resonances and broad resonances. The cross section contributions (and therefore the reaction rates associated with these components) can be added incoherently if there are no, or only negligible, interference effects between them. Interference effects between resonances are determined by the resonance spins and parities. Interference between resonances and the non-resonant component is linked to the incoming orbital angular momenta [3]. Incoherent summation of the components is used for all following considerations regarding $^{23}\text{Na}(p, \gamma)^{24}\text{Mg}$, in analogy e. g. to [4].

1.3 Direct Cross Section Measurements

The aim of nuclear cross section measurements for astrophysics is to obtain cross section data $\sigma(E)$ for the calculation of reaction rates in stellar models, which then can serve as input data to stellar modeling. Direct cross section measurements utilize particle beams to bombard a target and determine the reaction yield by detecting one or multiple reaction products. Direct cross section measurements can be challenging or even practically impossible to conduct in the energy range that is relevant for astrophysics, because of the low expected yields following from the energy dependence of the cross section. Measurements at higher energies can be used to extrapolate the S -factor to the region of interest, which, however, introduces an additional uncertainty to the values in the Gamow window. If resonances are suspected to have an influence on the reaction rate, a determination of their contribution to the total cross section will require measurements of their strength (i. e. cross section measurements at the resonance energy).

Indirect measurements, e. g. experiments studying transfer reactions with the same compound nucleus (for example $^{23}\text{Na}(^3\text{He}, d)$ instead of $^{23}\text{Na}(p, \gamma)$), may provide information that can be used to infer cross section information for the reaction of interest. Owing to the additional information that has to be incorporated for these analyses, such indirect methods are more prone to systematic uncertainties. For some reactions this may be the only way to obtain information in an energy region of interest, however, as the reaction cross sections in the Gamow window can be extremely small, or resonances be very weak.

For the cases where direct cross section measurements are feasible, they are highly desirable, as they provide a direct source of cross section data, so that the results from indirect experiments can be checked and complemented. The sensitivity limit of an experimental setup determines the energy range in which direct cross section

1 Introduction

measurements are feasible. With the importance of reliable cross section data with small uncertainties, there is the demand to push the energy limit for direct cross section measurements towards lower values.

In a direct cross section measurement, the reaction yield (i. e. the number of reactions per projectile) is linked to the cross section of the reaction, and can be determined experimentally by detecting the reaction products. In the following discussion, protons will be considered as projectiles, but the considerations apply to ion beams in general. Consider a homogeneous target that is bombarded by a proton beam of energy E_0 . As the beam traverses the target material, it loses energy due to electromagnetic interaction with the target. Although the energy loss occurs randomly in many individual interactions, it can be approximated as a continuous process due to the large number of these interactions. This energy loss is then characterized by the stopping power ε , which is defined as:

$$\varepsilon(E) = -\frac{1}{N} \cdot \frac{dE}{dx} \quad (1.9)$$

where N is the number density of the target nuclei. The stopping power is a function of material and projectile energy. In this work, tabulated values for the stopping power were taken from the software package SRIM 2013 [5]. To account for the transformation between center of mass and laboratory system, the stopping powers obtained from SRIM should be multiplied by the factor $m_{\text{target}}/(m_{\text{projectile}} + m_{\text{target}})$ before the use in the following equations to derive the reaction yields.

For a target of finite thickness, in which a projectile of initial energy E_0 loses an energy ΔE while traversing the target, the yield is given by:

$$Y = \int_E^{E+\Delta E} \frac{\sigma(E)}{\varepsilon(E)} dE \quad (1.10)$$

In the special case of a single narrow resonance at $E_{\text{res.}}$, the experimental yield from the resonance vanishes for proton energies below $E_{\text{res.}}$. Above $E_{\text{res.}}$ it has the value:

$$Y = \frac{\lambda^2}{2} \cdot \frac{\omega\gamma}{\varepsilon(E_{\text{res.}})} \quad (1.11)$$

If the target material consists of other nuclides than the active nuclide that is under study, either because of inactive isotopes or because of other elements in a compound, the stopping power has to be replaced by an effective stopping power when deriving the yields:

$$\varepsilon_{\text{eff}} = \varepsilon_{\text{active}} + \sum_i \frac{N_i}{N_{\text{active}}} \cdot \varepsilon_i \quad i \in \{\text{inactive nuclides}\} \quad (1.12)$$

As the inactive components of the target contribute to the effective stopping power,

they decrease the reaction yield. The choice of a target material with a small effective stopping power can therefore be an important factor to consider for measurements of small cross sections and weak resonances. For the same reason, a precise determination of the target stoichiometry is of great importance. See section 4.1 for the discussion about ^{23}Na targets in this work.

1.4 Experimental Challenges and Low-background Physics

For a successful measurement of very small cross sections, such as the reactions between two charged particles at low energies, the sensitivity of the experiment is the key element. Two factors can prohibit the detection of the signal from the reaction under study: either the signal rate is too low to detect a significant number of reactions in a feasible run time of an experiment (either because of a small experimental reaction rate or a low detection efficiency), or the background rate is too high compared to the signal of interest so that the signal is masked by background.

The experimental reaction rate can be increased by optimizing the experimental parameters that influence that rate. An increased intensity of incident projectiles directly reflects in an increased reaction rate. Apart from the technical limitations regarding the accelerator, however, the feasible beam current can also be limited by the maximum power of the target cooling system that prevents the target from thermal damage. Similarly, a smaller effective stopping power can increase the yield, but as various other practical considerations are important for the choice of the target material (cf. section 4.1), the target material with the lowest effective stopping power is not always a viable option. Improvements in detection efficiency typically imply detectors with larger active volumes, or greater numbers of detectors. Increasing the detection efficiency is thus a major economic factor and also limited by practical considerations, such as laboratory space.

If the sensitivity of an experiment is limited by a background signal, various methods of background reduction can be applied to reduce this unwanted contribution. Measures against environmental and cosmic backgrounds include passive shielding and active veto systems. In setups with multiple detectors, coincidence techniques can also be effective to distinguish background events from signal events (cf. for example, [6]). The background signal induced by cosmic rays, either directly depositing energy in the detector or producing (often highly energetic) secondary radiation, can be a significant limitation. Cosmic rays are difficult to shield in an experimental setup, owing to the penetrative nature of highly energetic cosmic rays, in particular muons.

An effective way to reduce the cosmic ray background is to conduct experiments underground, where the natural overburden – typically several hundreds of meters of rock – acts as a massive passive shielding. The Laboratory for Underground Nuclear

Astrophysics (LUNA) is located in the Gran Sasso National Laboratory (LNGS), where an overburden of 1400 m of rock provides a shielding equivalent to about 3400 m of water, and greatly reduces the flux of cosmic radiation. The cosmic muon flux, for example, is reduced by six orders of magnitude compared to the flux on surface [7].

For the experiments at LUNA, this reduction directly reflects in drastically lowered gamma ray backgrounds at energies above the energy range of natural radioactivity (cf. e.g. [8], see also Figures 2.9 and 3.1 for background spectra of the detectors used in this work). Furthermore, as the production of secondary radiation by cosmic rays on the materials of the experimental setup is strongly reduced, more massive shielding setups can be employed effectively underground. They can for example be used to reduce gamma ray backgrounds from natural radioactivity. Whilst typically the gamma ray background reduction has been the most significant advantage exploited in experiments at LUNA, also the neutron background underground is reduced by several orders of magnitude compared to the surface [9], and reduced background levels in a detector setup for α particles have been observed [10] as well.

With this advantage, LUNA provides a opportunity for the measurement of reactions that are limited by environmental backgrounds in a typical surface experiment. After the installation of the 400 keV accelerator in 2000, several reactions have been studied at LUNA, providing cross section data at significantly lower energies than previously available, see [11, and other articles in this issue].

1.5 $^{23}\text{Na}(p,\gamma)^{24}\text{Mg}$: Astrophysics and State of the Art

The reaction $^{23}\text{Na}(p,\gamma)^{24}\text{Mg}$ has a Q value of 11692.69(1) keV [12]. Considering proton-induced reactions on ^{23}Na , another reaction with a positive Q value is $^{23}\text{Na}(p,\alpha)^{20}\text{Ne}$, with $Q = 2376.13$ keV. In stellar scenarios there is a competition between the two reactions as illustrated in Figure 1.2. Whilst the reaction $^{23}\text{Na}(p,\alpha)$ closes a loop of reactions and radioactive decays which is known as the NeNa-cycle, $^{23}\text{Na}(p,\gamma)$ provides a transition to ^{24}Mg , which in turn can be part of a set of reactions that forms the MgAl-cycle. The ratio of the rates of the two reactions in the astrophysical scenario determines whether a NeNa cycle forms, or whether material is directly processed further towards the MgAl cycle, see for example [13, 14] for a discussion. The extent to which these cycles form, affects the yields of the involved nuclides in the star. In [15], $^{23}\text{Na}(p,\gamma)^{24}\text{Mg}$ was identified as one reaction whose rates would need to be constrained better in order to obtain more reliable yields for the elements Ne, Na, Mg and Al from intermediate mass AGB stars.

Table 1.1 shows the levels of ^{24}Mg above the Q value of $^{23}\text{Na}(p,\gamma)$, indicating the properties of (p,γ) resonances corresponding to these levels. Few of the resonances are of relevance for the astrophysical reaction rate. In stellar scenarios up to temperatures

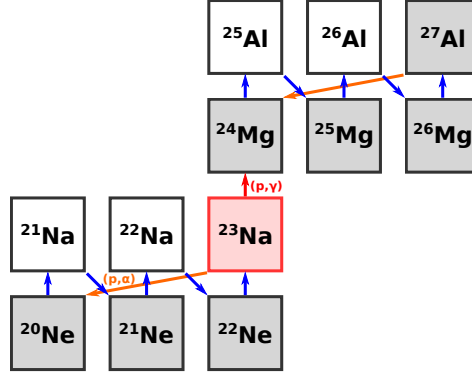


Figure 1.2: Reaction network with $^{23}\text{Na}(p,\gamma)$ as connection between the NeNa and MgAl cycles. Stable nuclides in gray.

Table 1.1: Levels in ^{24}Mg above the Q value of $^{23}\text{Na}(p,\gamma)$, with (p,γ) resonance properties where known. Energies and widths are in keV. Level data is taken from [16], and resonance properties are from [17, and references therein], unless indicated otherwise. $S = 8 \cdot \omega\gamma$ in eV. The $E_{\text{res.}}^{\text{c.m.}}$ and $E_{\text{res.}}^{\text{p}}$ are calculated from level energy and Q value and thus may differ from experimentally observed values $E_{\text{res., exp.}}^{\text{p}}$.

Level	J^π	BR	Γ_{total}	$S(p,\gamma)$	$\Delta S/S$	$E_{\text{res.}}^{\text{c.m.}}$	$E_{\text{res.}}^{\text{p}}$	$E_{\text{res., exp.}}^{\text{p}}$
11695.6	4^+	yes	0.0016			2.9	3.0	
11728.1	0^+	yes	10.			35.4	36.9	
11827.		no		$< 6.46 \cdot 10^{-9}$ [18]		134.3	140.1	
11862.		yes				169.3	176.7	178
11864.9	1^-	yes	7.			172.2	179.7	
11904.		no	5.5			211.3	220.5	
11931.2		no	< 0.02	$4.20 \cdot 10^{-3}$	33%	238.5	248.9	250.9(2)
11969.6	2^+	yes	1.8	$< 4 \cdot 10^{-3}$		276.9	288.9	285.9(5)
11987.72	2^+	yes	< 0.002	$8.40 \cdot 10^{-1}$	18%	295.0	307.9	308.75(6)
12002.3		yes				309.6	323.1	
12015.2	3^-	no	0.7	$< 1 \cdot 10^{-2}$		322.5	336.5	338.6(6)
12049.1	4^+	yes	< 0.02	$1.10 \cdot 10^{-2}$	27%	356.4	371.9	374.3(4)
12119.5	$(2,3,4)^+$	yes	$< 2.$			426.8	445.4	445(1)

1 Introduction

of 1 GK, the reaction rate is mostly determined by the non-resonant cross section and two or possibly three narrow resonances at low energies. The influence of the different contributions as a function of temperature is shown in Figure 1.3, created using input values as compiled in [4]. For simplicity, the resonances will be referred to by their approximate proton energy in the text. First the current state of the input data for the individual contributions will be presented briefly.

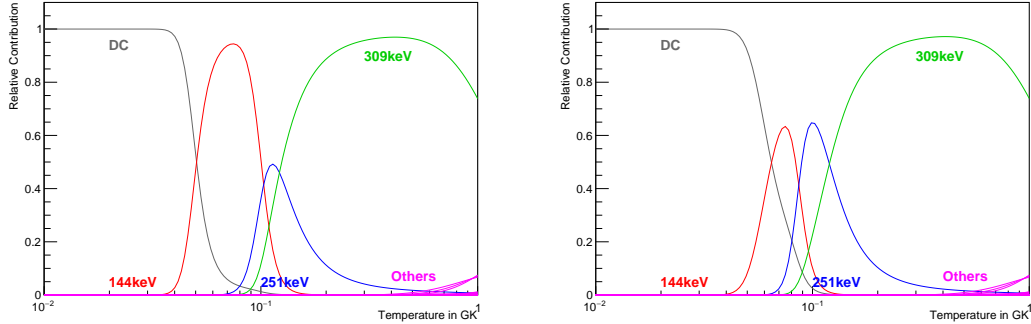


Figure 1.3: Fractional contributions of the direct capture and resonant components to the reaction rate as a function of temperature, assuming the upper limit from [18] (left), or 1/10 of this value (right) as the strength of the 144 keV resonance.

The narrow resonance at a proton energy of $E_p = 308.75(6)$ keV [19] has a strength of $\omega\gamma = 105(19) \cdot 10^{-3}$ eV. The resonance strength, quoted in [17] was obtained from a value determined by a direct experiment with bombardment of an oxidized sodium solid target and a sodium iodide detector [20]. The results of this experiment were normalized to match the results for another resonance at a proton energy of 512 keV that was measured in [21, 22]. In the experiments used for the normalization, various targets were bombarded to measure the $^{23}\text{Na}(p, \gamma)$ resonance strengths relative to resonances in $^{27}\text{Al}(p, \gamma)$, $^{31}\text{P}(p, \gamma)$ and $^{35}\text{Cl}(p, \gamma)$ with a setup consisting of a Ge(Li) and a NaI detector.

Another narrow resonance at $E_p = 250.9(2)$ keV [17, and references therein] has a strength of $\omega\gamma = 0.525(175)$ meV, determined by the same experiments as for the 309 keV resonance. Compared to the 309 keV resonance, the strength of this resonance is known with a larger uncertainty.

A potential (p, γ) resonance corresponding to a level at $E_x = 11827$ keV can not yet be excluded to have a significant influence on the reaction rate, based on the current upper limit on its strength. Results for the energy of this level obtained in different experiments are shown in Table 1.2, with the most recent value from [14] being higher than the two previously determined values, but compatible given the uncertainty of the results. The uncertainty quoted by [14] is 1.8 keV, and combining this result with [23]

the authors adopted a level energy of 11830.7(15) keV. This level energy corresponded to a resonance energy of 138.0(15) center of mass energy, or 144.0(16) keV proton energy. This value will be used to refer to this resonance in this work.

Table 1.2: Energy of the level for the “144 keV” resonance and corresponding proton energies that follow with the Q -value derived from [12].

Reference	Measurement	Level Energy	$E_p^{\text{c.m.}}$ in keV	E_p^{lab} in keV
[23]	$^{24}\text{Mg}(p,p')$	11828(3)	135.3(30)	141.2(31)
[24]	$^{12}\text{C}(^{16}\text{O},\alpha)$	11827(4)	134.3(40)	140.1(42)
[14]	$^{23}\text{Na}(^3\text{He},d)$	11831.7(18)	139.0(18)	145.1(19)
[14, adopted]		11830.7(15)	138.0(15)	144.0(16)

This lack of precise information about the strength of the 144 keV resonance results in a large uncertainty of the reaction rate for the temperature range in which the resonance has the potential to be the dominant contribution.

Multiple attempts were made at a direct search for this 144 keV resonance. The most recent experiment was conducted at the Laboratory for Experimental Nuclear Astrophysics (LENA) [25, 18]. In that experiment, solid targets of evaporated Na_2WO_4 were bombarded by a proton beam. The gamma radiation detector setup used a high-purity Germanium (HPGe) detector facing the target, surrounded by an annulus of a sodium iodide (NaI) scintillation detector. The experiment was conducted on surface, and measures to reduce environmental backgrounds included a lead-shielding around the detector setups, the use of coincidence techniques between HPGe and NaI detectors and an additional muon veto of plastic scintillators surrounding the setup. The coincidence and anti-coincidence between the detectors were a central element of this approach. As the gamma ray branching ratios for this level are unknown, assumptions had to be made and the influence of different possible branching ratios had to be studied. See [25] for details of the work at LENA and subsection 4.3.2 in this work for a discussion of this issue in the context of the present work at LUNA.

As a result of the experiment at LENA, an upper limit of the resonance strength of 5.17 neV could be established. A slight excess of the signal over background has been observed in this experiment, which, if interpreted as a signal, yielded a resonance strength of 2.15(129) neV. Assuming this strength, the resonance would be the leading contribution to the reaction rate in the temperature range of approximately 50-90 MK.

For the direct capture cross section, measurements at low energies are hindered by the strong influence of the Coulomb barrier ($Z_{\text{Na}} = 11$). At higher energies, the direct-capture component of the cross section is overshadowed by a number of strong resonances. Information on the direct capture cross section has been obtained with indirect

1 Introduction

measurements [14], and the results for the direct capture process S factor as given in [4] were used throughout this work.

2 Setup

2.1 The LUNA Facility

For almost 25 years now, LUNA has provided the opportunity to study nuclear reactions underground at the Gran Sasso National Laboratory (LNGS), located in the Gran Sasso massif in Abruzzo, Italy. Initially using a 50 keV accelerator, in 2000 a new commercial electrostatic accelerator with a radiofrequency ion source was installed underground.

This “LUNA 400” accelerator can deliver protons and alpha particles with energies up to 400 keV, with a high accuracy and reproducibility of the beam energy, a beam energy spread of 0.1 keV and excellent stability of the beam energy over time [26]. The achievable proton beam currents on target at LUNA typically are on the order of 100-400 μA . The LUNA facility has two beamlines for different experiments. One of them is currently dedicated for experiments with solid targets, whereas the other beamline hosts a windowless gas target system. Figure 2.1 gives an overview of the scale of the accelerator and the two setups at LUNA.

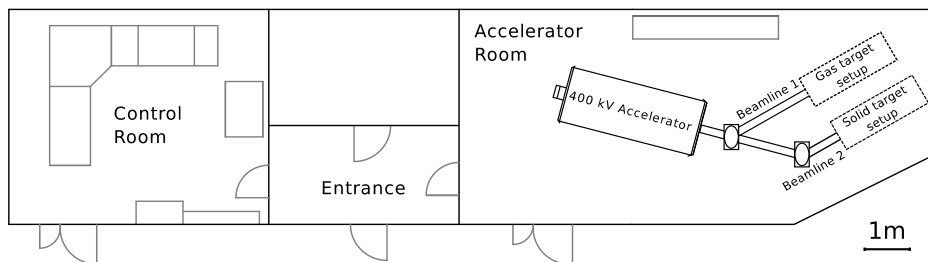


Figure 2.1: Sketch of the floor plan of the LUNA facility underground at LNGS [27].

2.2 Solid Target Setup at LUNA

The experiments on ^{23}Na were conducted with solid targets, with an active layer containing ^{23}Na deposited onto a Tantalum backing. The targets will be described in section 4.1. In the course of these experiments, two different detector setups, both located on the solid target beamline, were used. As the beam is stopped in the target, its power dissipates in the target material. Currents on the order of few hundred μA and energies of few hundred keV correspond to a heating power on the order of 10-100 W. As

2 Setup

this power is focused on a fairly small area, active cooling is required to avoid excessive heating of the target. Too high temperatures can deteriorate the target properties (e. g. by evaporation or diffusion of the active material). To limit the increase in target temperature, the back side of the target was water cooled in both setups. The target chambers were mounted electrically isolated on the beamline, so that the number of impinging protons per unit time could be directly measured as an electric current. A current integrator converted the accumulated charge into a series of pulses, where each pulse corresponded to a fixed amount of charge. Impinging beam on any other part of the target chamber than the active target has to be strictly avoided, as this would lead to the measurement of larger values for the accumulated charge than the charge that actually reached the active target, and thus would systematically decrease the reaction yield determined in the experiment. Water-cooled tantalum apertures in the beamline were used to restrict the beam diameter in order to avoid stray beam hitting other parts than the active target.

Another possible source for a systematic error in the determination of the intensity of impinging protons by current measurements are electrons that can be emitted from the target as an effect of the proton beam interaction with the target material. If these secondary electrons were not collected, the measured (positive) current would be larger than that corresponding to the flux of protons. Hence accumulated charges would be over- and yields underestimated. To counter this effect, a copper tube was installed inside the beamline, isolated from the target chamber and the other parts of the beamline. The tube was installed closely in front of the target, and put on a potential of -300 V in order to deflect electrons emitted from the target back onto the target. This system is referred to as secondary electron suppression.

As the tube was mounted close to the target, another possibility to distort the current reading on the target would be protons from the beam impinging on the tube of the secondary electron suppression. If secondary electrons are emitted from the tube and consequently pushed towards the target chamber, the measured accumulated charge would be smaller than that of the protons that reached the target, and the yield determined from the measurement was consequently higher. This effect was again limited by defining the beam with the help of the aforementioned apertures. In addition, the current provided by the power supply connected to the tube is closely monitored while tuning the beam to notice when part of the beam would impinge the tube.

The tube of the secondary electron suppression also served a second purpose. In thermal contact with a bath of liquid nitrogen, it worked as a cold trap to catch organic vapors in the beamline volume. With this setup, a deposition of carbon on the target surface was avoided. Such a deposition would be unfavorable for different reasons. On one hand, the deposition of additional material in front of the active target corresponds

to an energy loss of the protons before they reach the active layer. Hence if the carbon layer builds up with time, the energies observed in the active layer will change (e.g. a narrow resonance will appear to “move” towards higher energies in time). On the other hand, proton-induced reactions on carbon, such as $^{12}\text{C}(\text{p}, \gamma)$ can be a source of beam-induced backgrounds (cf. subsection 4.1.9), which is to be avoided if possible.

2.3 HPGe Detector

2.3.1 Detector Setup

A high-purity germanium (HPGe) detector was used for the gamma-ray spectroscopy of $^{23}\text{Na}(\text{p}, \gamma)^{24}\text{Mg}$. A HPGe detector exploits the semiconductive properties of germanium: an energy deposition from ionizing radiation creates free charge carriers (electrons and holes), which can be registered as an electronic signal when a voltage is applied [28]. The quoted relative efficiency of the coaxial p-type germanium detector (ORTEC GEM120225-P-ST) at 1.33 MeV was 121% in 2001 [29]. A more recent measurement by the manufacturer in 2016 determined a value of 104% for the same efficiency [30]. For a discussion of the detector efficiency, see section 2.3.

The detector setup is illustrated in Figure 2.2. In the setup for this detector, the target disk was placed at an 55° angle with respect to the proton beam. The detector was positioned with its front surface parallel to the target. The position at 55° is chosen to limit the influence of possible angular correlations of the gamma ray emission with respect to the beam axis, as the Legendre polynomial P_2 vanishes for $\cos^2 \theta = 1/3$.

To increase the detection efficiency for gamma rays following reactions in the target, the detector is placed close to the target (about 7 mm in front of the target holder, corresponding to about 20 mm distance to the beam spot).

2.3.2 Summing Effects

When detecting a single gamma ray, typically the full energy peak (FEP) in the energy spectrum is considered. For a gamma ray of a certain energy $E_{\gamma 1}$, events in this peak correspond to the deposition and detection of the full gamma ray energy $E_{\gamma 1}$ in the detector. The probability for an emitted gamma ray to yield an event in the full energy peak is given by the full energy peak efficiency ε^{FEP} . The probability for the gamma ray to deposit any amount of energy in the detector is called the total efficiency ε^{tot} .

The increased detection efficiency for a single gamma ray that is achieved by a close detector geometry comes at the cost of an increased influence of summing effects for the detection of gamma ray cascades. Summing effects occur when multiple gamma rays of one cascade reach the active volume of the detector and the energies of more than one gamma ray are completely or partially deposited in the active volume. The detector is

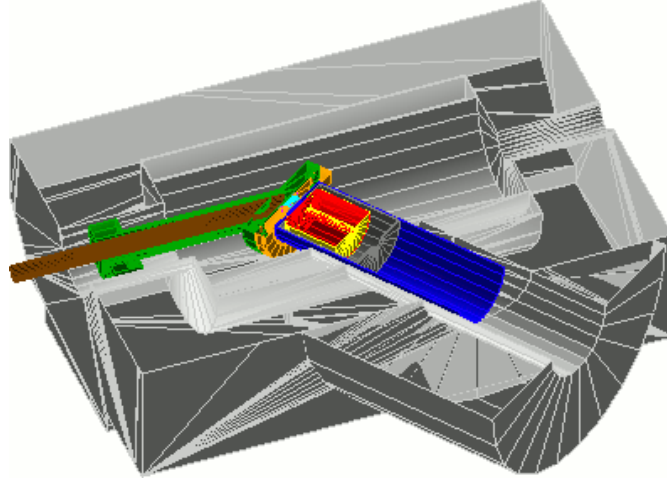


Figure 2.2: Sketch of the HPGe setup (cut open horizontally for visualization). The target chamber is shown in green, the active detector volume in red. The target is located behind the visible cyan volume of the water cooling. The secondary electron suppression tube is shown in brown. The part of the beamline upstream of the target chamber is not shown here.

not able to resolve the different depositions and registers a signal that corresponds to the total deposited energy, summing the contributions from the different gamma rays.

In the simplest case of a single gamma ray, if ε^{FEP} for a given gamma ray energy and detector setup is known, the number of events in the FEP can be directly related to the number of emitted gamma rays (and hence the number of reactions, if the gamma ray intensities are known). For a cascade of gamma rays, however, the probability to obtain an event in the FEP for E_{γ_1} will be modified by summing effects. To obtain an event in the FEP, not only will E_{γ_1} have to deposit all its energy in the detector, but all other gamma rays of the cascade (E_{γ_2} etc.) should not deposit any energy to avoid increasing the total deposited energy, which would yield an event outside the FEP region. As this effect decreases the number of events in the FEP, it is called summing out. A special case of summing occurs, if two gamma rays E_{γ_1} and E_{γ_2} both deposit their complete energy in the detector. If these gamma rays correspond to consecutive transitions in the cascade of nuclear de-excitations, such an event at $E_{\gamma_1} + E_{\gamma_2}$ can mimic a full energy event of E_{γ_3} , corresponding to the direct transition (see Fig. 2.3 for an illustration). As these summing effects increase the number of events in the FEP of E_{γ_3} , they are called summing in.

With this kind of detector, summing effects are generally unwanted. The influence of summing effects increases with the detection efficiency, so that it is generally a trade-off between sensitivity (efficiency) and susceptibility for summing effects. As most of the gamma ray sources (e.g. reactions) used in this work result in gamma ray cascades,

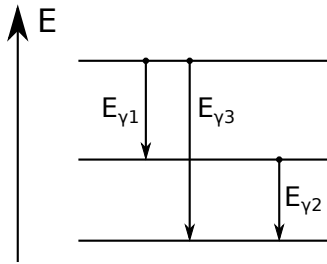


Figure 2.3: Example level scheme with three levels to illustrate summing in. A deexcitation via the cascade $E_{\gamma 1} \rightarrow E_{\gamma 2}$ can, if the energy of both gamma rays is deposited fully in the detector, lead to the detection of an event that is indistinguishable from $E_{\gamma 3}$ depositing its full energy.

summing effects need to be carefully considered in any analysis of full energy peaks in spectra. The treatment of summing effects for the efficiency calibration is described in more detail in section 3.4.

2.3.3 Electronics & Data Acquisition Setup

A CAEN N1471HET module supplied the +4900 V bias voltage for the detector. The signal from the preamplifier integrated into the detector was amplified by an ORTEC Model 671 spectroscopic amplifier, and fed into the input of an ORTEC A^{SPEC}-927 Multi-Channel Analyzer (MCA) with 16,384 channels. The second input of the MCA was connected to a pulse generator that was triggered by the signal of the current integrator, so that an event in the second MCA channel corresponded to a fixed amount of charge on target and thus allowed to record the charge on target together with the gamma ray spectrum. A scheme of the electronic setup is shown in Figure 2.4.

ORTEC's MAESTRO software for Windows was used to acquire the spectra. The saved data comprises the counts for the binned spectrum, live time and real time. The live time is the duration in which the detector setup was sensitive to detect events. The difference between real time and live time is called dead time. It is a consequence of the fact that owing to effects intrinsic to the detector or to the signal processing electronics, the detection of a physical event in the detector is followed by a period in which no second event can be registered. In this setup, the dead time is determined and calculated internally by the MCA.

The described configuration does not provide list mode capability, i. e. an event-by-event recording. For longer runs, intermediate spectra were automatically saved in fixed time intervals. This allowed to obtain some information on the evolution of the spectrum during the measurement.

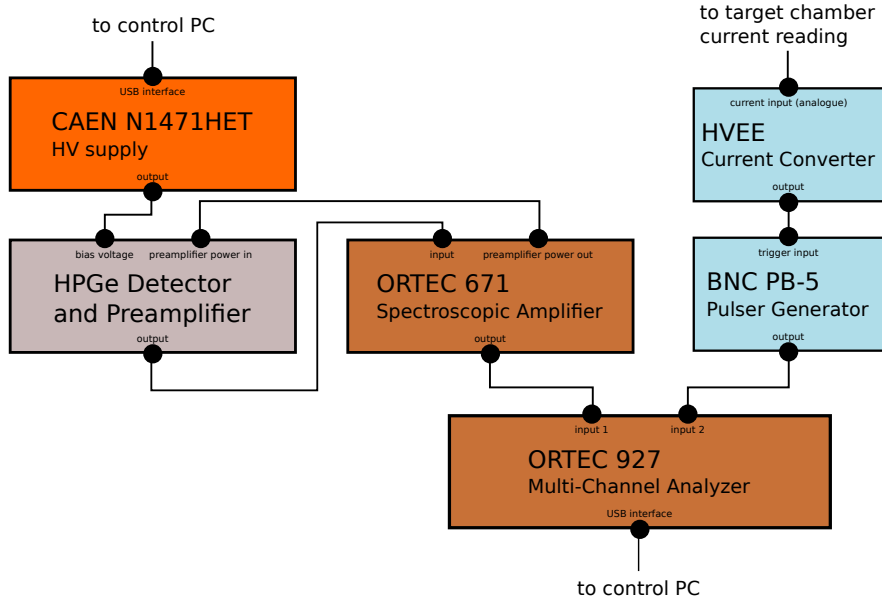


Figure 2.4: Scheme of the HPGe electronics chain.

2.4 Bismuth Germanium Oxide (BGO) Detector Setup

2.4.1 Detector Setup

Bismuth Germanium Oxide (BGO) is an anorganic scintillator, i. e. a material in which the energy deposition of an ionizing particle leads to the emission of light. The light output is related to the amount of energy deposited, and the detection of the amount of this faint light, e. g. by using photomultiplier tubes (PMTs), allows to exploit this effect for the detection and spectroscopy of gamma rays. Owing to the high atomic charge number of Bi and large mass density of BGO, the cross section for gamma ray interactions is high, compared to lighter materials (such as germanium).

The detector used in this setup had six prismatic (approximately $58 \text{ cm}^2 \times 28 \text{ cm}$) BGO segments located around a cylindrical borehole, as shown in Fig. 2.5. The six crystals are arranged to maximize the angular coverage of a target at the center of the borehole. The aim of this detector is to maximize the detection efficiency for gamma rays, exploiting the beneficial properties of BGO for highly efficient gamma ray detection and covering a large solid angle with sensitive detector volume. The large detection efficiency for individual gamma rays leads to strong summing effects. The basic principle of summing is identical to that discussed in the previous section, but for this detector, summing is a fundamental principle. The detection of all or most of the energy released as gamma rays in a $(*, \gamma)$ reaction can help to place the region of interest in the energy

spectrum towards higher energies, avoiding the majority of detector backgrounds. The backgrounds for this detector will be discussed in more detail in section 3.2.

The crystals were optically isolated and read out separately by photomultiplier tubes located at one end of the bars, with the other end covered by a plastic light reflector. This segmentation of the detector offered the possibility to regain some information about the individual gamma rays in the cascades, while adding the single crystal signals of one coincident event maximizes the summing efficiency, similar to having a detector with one large crystal.

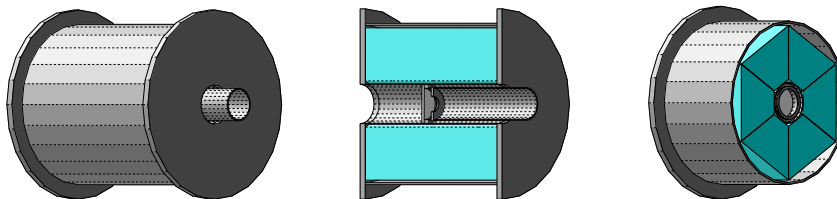


Figure 2.5: Sketches of the BGO detector with parts of the target chamber shown in the center of the detector. [31]

The detector is described in [32], and has been used for several campaigns in at LUNA in the past [33, 34, 35] with one of its main strengths being the detection of weak (\ast, γ) reactions with large Q values, for the reasons elaborated above.

2.4.2 Electronics & Data Acquisition Setup

The configuration of the electronics is shown schematically in Figure 2.6. The six PMTs (Hamamatsu R1847-07) for the detector segments were fed by a programmable VME high voltage supply (CAEN V6533). The module had six independent channels, so that the voltage for each PMT could be set individually. This allowed to set the gain of each channel to such values that the relation between the amplitude of the electronic signal of the PMT and the gamma ray energy deposited in the detector was approximately the same for each channel (gain matching). The cathode output of each PMT was connected to an ORTEC Model 113 preamplifier. A pulser signal was supplied to the test input of these six PMT preamplifiers as well as the test input of a seventh preamplifier.

In the course of this work, a new digital data acquisition system has been set up for the use with this BGO detector. This setup utilized a CAEN V1724 digitizer, which had 8 channels, a resolution of 14 bit and a sampling rate of 100 MS/s. The digitizer firmware supported pulse height analysis [36, 37] of the digitized signal on the internal FPGA. The software “MC² Analyzer” by CAEN was used for the acquisition of list mode data, acquiring and saving information event by event. Each saved event consisted of a trigger timestamp, energy and some additional information to indicate special events

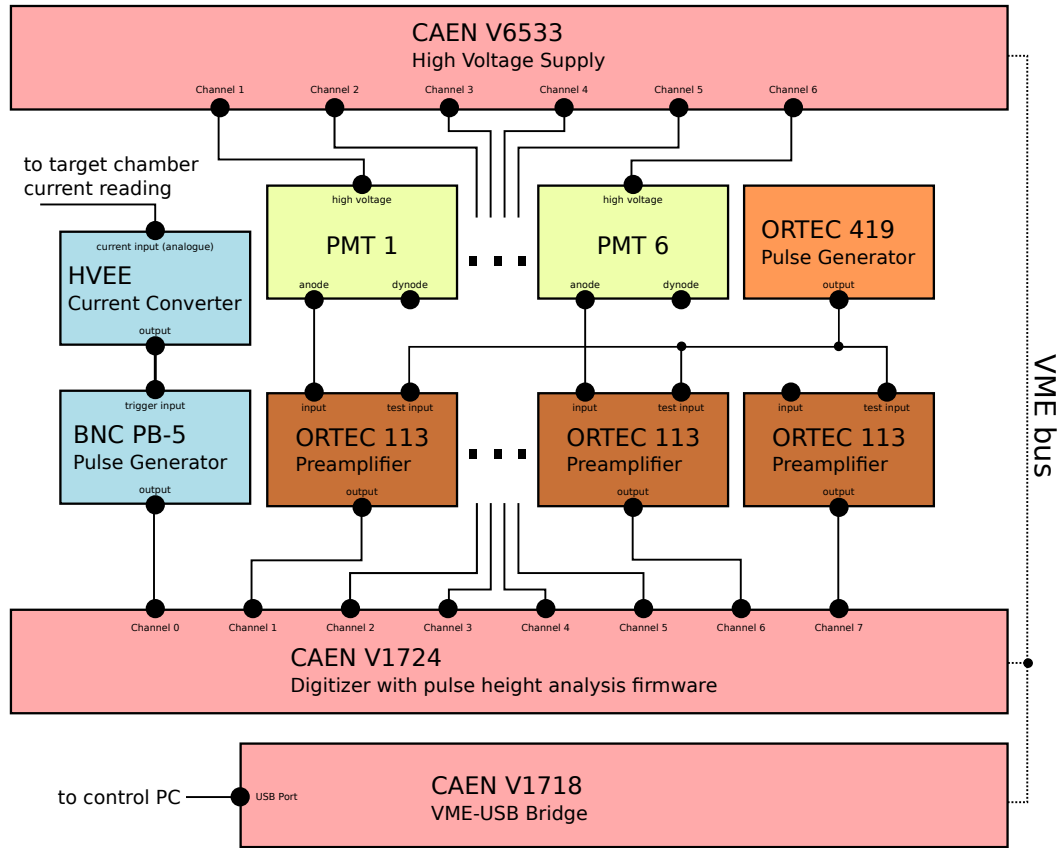


Figure 2.6: Scheme of the BGO electronics chain.

and conditions (such as an ADC overflow).

Channels 1-6 of the digitizer were connected to the preamplifiers with the PMT signals, and channel 7 to the preamplifier that had its input disconnected and only the pulser signal supplied to the test input. The remaining channel 0 was connected to a pulse generator that is triggered by the current integrator to record the current on target. In this configuration the number of pulses is proportional to the charge that was registered in the current integrator. By virtue of the list mode capability, the development of the acquired spectra and the current on target over the course of the measurement (i. e. in time or with accumulated charge) can be traced.

Each channel was set to trigger independently. Hence, the acquired data consisted of list mode data for each channel, with time stamp and (uncalibrated) energy information for each event. The synchronization of the timestamps in the different channels was provided internally by the digitizer.

2.4.3 Data Processing

To fully benefit from the capabilities of the summing detector, the first step of data processing dealt with the identification of coincidences between events in the seven channels that were connected to the preamplifiers. First the events were merged into a stream of events ordered by time stamp. Next, events were grouped into coincidences. Events were considered to be in coincidence if their time stamps fell within a given time window after the first event. If a signal was detected in the channel that had only the pulser connected to it (channel 7), the coincidence event was flagged as a pulser event. The time window for coincidence events has to be long enough to account for a variation of the trigger timestamps of the channels within one event, but should not be larger than necessary to limit accidental coincidences (random summing). A time window of $3.5 \mu\text{s}$ was chosen for the given setup.

The events that are caused by signals provided by the pulse generator and fed to the test input of the preamplifiers need to be efficiently removed from the energy spectrum, as they do not correspond to a physical interaction in the detector. A separate analysis of these events can, however, yield a handle on the dead time of the data acquisition system during the measurement. The seventh preamplifier that had only the test input connected served as the indicator for these “pulser events”.

In the next step to process the physical events, the energy information of the single events was converted from an ADC value to a physical energy, where the energy calibration was determined from the single crystal spectra obtained in measurements of known radioactive sources or (p, γ) reactions. The calibrated energy information was then used to create histograms of the event energies for each individual crystal, and of the total energy of the coincidence events (i. e. the sum of the energies of all events within a coincidence event). The histograms will be referred to as single and sum histograms in the following. The histograms were saved for further analysis. Depending on the requirements of the analysis, also a list of coincidence events with the information of the involved single events (before and after energy calibration) and the pulser flag were saved for further processing.

2.5 Limitations and Complementarity of the Detector Setups

The two detector setups have very different strengths and weaknesses and serve distinct purposes. The HPGe detector setup has an excellent energy resolution (few keV at MeV energies). Its limited size and the physical properties of germanium limit its detection efficiency for gamma rays. With these properties the HPGe detector is well-suited for gamma ray spectroscopy, i. e. the identification of individual gamma ray lines in the spectrum by their energy, which allows to relate them to transitions in the nuclear level

scheme of the compound nucleus. The disadvantage of this detector setup is its relatively low efficiency, which can be prohibitive for the detection of very low reaction yields. The BGO detector on the other hand provides a superior detection efficiency. Due to the size of its six segments, even a single crystal can show significant summing effects for gamma ray cascades, and summing is considered the elementary feature of this detector. A disadvantage of BGO is the low energy resolution of this scintillation detector, which can be about a factor of 30 worse than for the HPGe detector, i. e. around a hundred keV at lower MeV energies. These properties make it very difficult to resolve individual gamma lines in the spectrum, except for situations with few strong lines that are well-separated in energy. If the contributions to the spectrum are known, however, the detector response can be described well (cf. chapter 3) and the large summing efficiency allows the detection of very weak reactions.

To compare the two detector setups side by side, one can consider the deexcitation of the $E_x = 11987.72$ keV level in ^{24}Mg as an example. This state corresponds to the 309 keV resonance in $^{23}\text{Na}(p, \gamma)$, which is strong enough to be detected with both setups. Figure 2.7 shows spectra measured with the two detector setups. Whilst the HPGe setup allows a detailed identification of the transitions in ^{24}Mg (and other transitions from spurious reactions), only the strongest transitions are visible by eye in the BGO detector spectrum for a single crystal spectrum. The BGO sum spectrum on the other hand shows a strongly enhanced signal at E_x as an effect of the increased summing probability.

For this experiment, the main task of the BGO detector setup was the search for the 144 keV resonance as well as the study of the two major resonances at 251 keV and 309 keV. While the efficiency of the BGO detector allows the detection of weak resonances, it is not well-suited to distinguish the gamma rays from closely-spaced narrow resonances such as those that are present towards higher energies in $^{23}\text{Na}(p, \gamma)$. At a proton beam energy of $E_0^p = 340$ keV, for example, the main visible $^{23}\text{Na}(p, \gamma)$ signal would come from a resonance at $E_{\text{res.1}}^p = 336.5$ keV, from reactions occurring at a depth in the target that corresponds to an energy loss of $E_0^p - E_{\text{res.1}}^p$, which will be within the main sodium target layer. Owing to the small but non-negligible sodium content also at greater depths, however, another contribution from the $E_{\text{res.2}}^p = 309$ keV resonance will typically be present. The sodium contents at this depth will be much smaller (i. e. the effective stopping power larger), but with its much greater strength, the yield from the 309 keV resonance in the low-sodium part of the target can be significant in comparison to the 336.5 keV resonance yield in the main target layer. As the excited states in ^{24}Mg that correspond to these two resonances differ by less than 20 keV in energy, the energy resolution of the BGO detector is not well-suited to distinguish primary gamma rays from the two resonances (to the same state in ^{24}Mg), or the total gamma ray energy

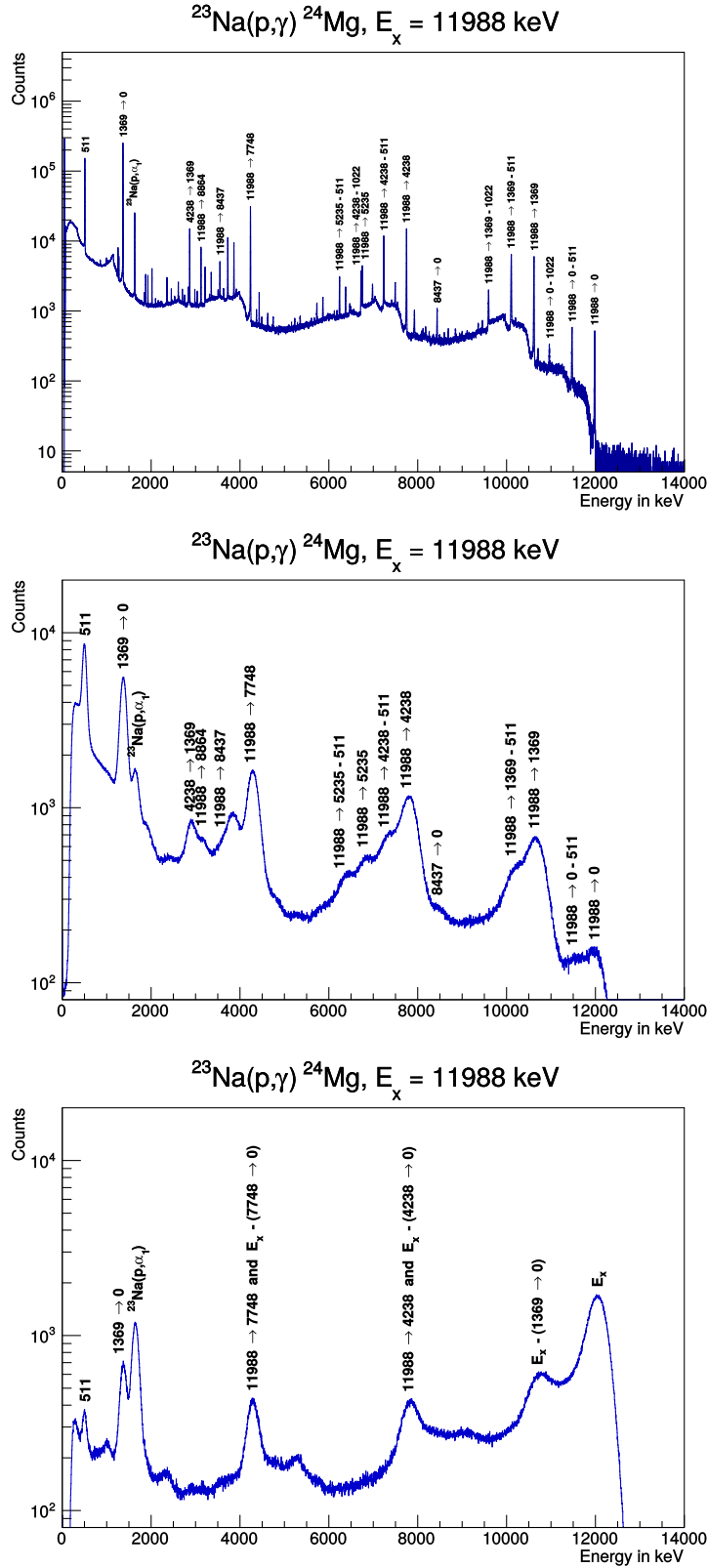


Figure 2.7: Gamma spectra for measurements of $^{23}\text{Na}(p,\gamma)^{24}\text{Mg}$ with E_p slightly above the excitation energy for $E_x = 11987.72$ keV, acquired with the HPGe detector (top), the single crystals in the BGO detector (center) and the sum of all crystals in the BGO detector (bottom).

peaks of both resonance contributions in the sum spectrum. The same limitation applies for the detection of a possible non-resonant component, which cannot be distinguished from the contributions from narrow resonances at proton energies slightly below the beam energy E_0 . The HPGe detector, on the other hand, is well suited for that purpose. It is used to study the same two major resonances as with the BGO detector, as well as the minor resonances at higher energies that are still sufficiently strong to be detectable with the sensitivity of the HPGe setup. In these cases, the energy resolution of the HPGe detector allows a study of the branching ratios of the resonances. With its limited efficiency, however, a study of the 144 keV resonance (for example) could only be considered reasonable to attempt with the HPGe detector if the resonance signal shows up strongly in the BGO detector measurements.

2.6 Shielding

To reduce environmental backgrounds, both detector setups employ a lead shielding. The shielding, shown in Figure 2.9, is modular with the main parts shared by both setups. The configuration with the BGO detector is shielded by 10 cm of lead, the HPGe detector by 15 cm of lead. The two (BGO) or three (HPGe) parts of the shielding are mounted on rails, to provide easy access to the target, e. g. to exchange the target, which is required regularly.



Figure 2.8: Lead shielding in the BGO and HPGe configuration.

The effect of the shielding on the BGO setup will be discussed in more detail in section 3.2. A comparison between an environmental background spectrum acquired with the same HPGe detector with and without the shielding is shown in Figure 2.9. The suppression of the environmental gamma ray lines and the continuum caused by them is evident. For comparison the figure also includes a background spectrum acquired on surface, where the continuous background induced by cosmic rays is prominent above 3 MeV in the surface spectrum, and massively suppressed for the detector in the underground location.

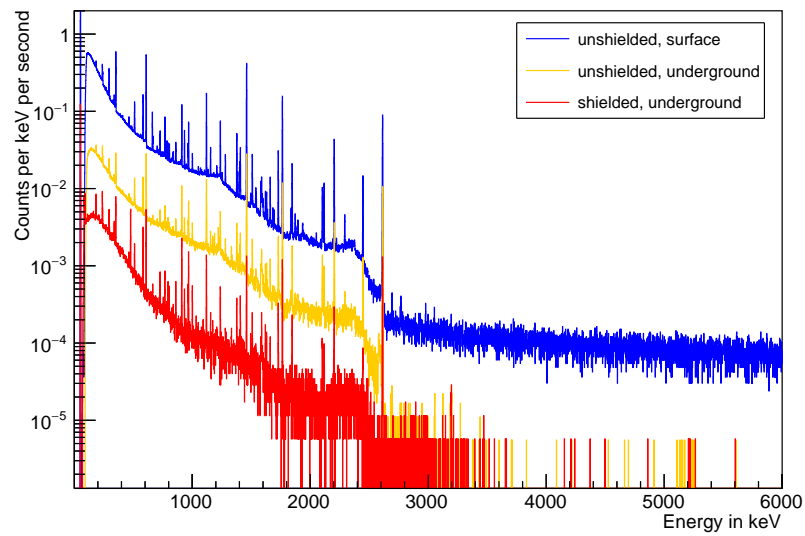


Figure 2.9: Comparison of background spectra with the HPGe detector setup on surface without shielding, underground without shielding, and underground with the shielding that was used in this work.

3 Detector Characterization

3.1 Methods

3.1.1 Monte Carlo Simulation

A Monte Carlo particle transport simulation can be a valuable tool to study the influence of different parameters of the setup on the detector response to radiation. To this end, a simulation based on the Geant4 toolkit [38, 39], version 4.10.02, was implemented. To simulate the detector responses to gamma rays, electromagnetic interactions were included in the physics model of the simulation by the “G4EmLivermorePhysics” class. In the case of the neutron-induced background study described in section 3.2, the “Shielding 2.1” physics list was used, which also includes neutron interactions.

A simplified geometry of the BGO detector without the PMTs already existed and had been compared successfully to experimental measurements in the past [35]. The geometry is based on the technical drawing provided by the manufacturer. The scheme in Figure 2.5 was created on the basis of this geometry.

The HPGe detector geometry was initially implemented as given by a drawing that was provided with the detector when it was acquired in 2001. An accurate description of HPGe detectors with Monte Carlo simulations often require an adjustment of the geometry with respect to the nominal geometry in order to accurately reproduce the detector response. This can be an effect of different geometric properties (e. g. shape, size and location of the germanium crystal) which can be directly obtained by imaging techniques such as radiography [40]. On the other hand, also microscopic effects such as the dead layers of the detector can significantly influence the detection efficiency. Dead layers describe the regions of the detector in which the charge collection is not effective, so that an energy deposition is not registered as a detector signal. Hence these layers effectively shield the detector and reduce its sensitive volume. To allow to make such changes the detector geometry was implemented using a number of parameters (material thicknesses, crystal dimensions, distances, etc.) that could be customized to tune the simulation as flexibly as possible. Tuning of the simulation parameters is described in section 3.4.

3.1.2 Sources and Reactions Used for Calibration

To determine the efficiency and energy calibration of the detector setups, different gamma ray sources were used. Table 3.1 lists the main properties of the radioactive

3 Detector Characterization

calibration sources ^{60}Co and ^{137}Cs , which were used. The decays of both nuclides are well-known, and their use to calibrate gamma ray detectors is well-established. ^{60}Co yields cascade of two gamma rays, whereas ^{137}Cs emits only a single gamma ray and thus avoids coincidence summing effects.

Nuclide	Gamma Energy / keV	Gamma Intensity / %
^{137}Cs	661.657(3)	85.1 0(20)
^{60}Co	1173.228(3)	99.85(3)
	1332.492(4)	99.9826(6)

Table 3.1: Main gamma lines of the well known calibration nuclides ^{60}Co and ^{137}Cs . [16]

With the large Q -value of $^{23}\text{Na}(p, \gamma)$, the energy of the emitted gamma rays following this reaction is expected to be as high as 12 MeV. No practical (long-lived) radioactive sources can provide gamma rays of this energy. Therefore, nuclear reactions are used to extend the detector calibration to this energy range. In this work narrow resonances in the reactions $^{14}\text{N}(p, \gamma)$ ($Q = 7296.78$ keV) and $^{27}\text{Al}(p, \gamma)$ ($Q = 11585.02$ keV) were studied. For $^{14}\text{N}(p, \gamma)$, the targets consisted of TiN on tantalum as used in [41]. The targets to study $^{27}\text{Al}(p, \gamma)$ were produced by evaporation of metallic aluminum onto tantalum.

$^{14}\text{N}(p, \gamma)$ has a narrow resonance at a proton energy of 277.9(3) keV, and the gamma ray branching ratios of the excited state corresponding to this resonance are well-established [41]. The gamma ray cascades for this excited state provide an interesting test case insofar as that there is a weak transition from the excitation energy to the ground state, and de-excitation occurs mainly in two-step cascades otherwise. Therefore summing in effects are prominent for the ground state transition.

The reaction $^{27}\text{Al}(p, \gamma)$ has multiple narrow resonances at proton energies that are accessible at LUNA [17]. Two resonances at 292.6(4) keV and 326.6(4) keV were chosen for the calibration. Another resonance at 222.7(4) keV was neglected, as contributions from another resonance at 202.8(9) keV were visible in the gamma ray spectra and the gamma ray branchings are not well known, so that further studies would have been required to disentangle the signals of these resonances. Detailed gamma ray branching information for the selected resonances is available [42].

The measurements with ^{14}N and ^{27}Al allow absolute measurements, i. e. the number of gamma rays of a certain energy that were emitted can be derived according to (1.11), knowing the target stoichiometry, accumulated charge and gamma ray intensities for the excited states. In addition to these reactions, gamma ray spectra acquired on the 309 keV resonance of $^{23}\text{Na}(p, \gamma)$ were used to extend the efficiency data towards higher gamma ray energies. As the strength of this resonance is subject to study in this work,

it cannot be used for an absolute measurement. But with the branching ratios of the excited state in ^{24}Mg known, these measurements can be used to relate the detection efficiency at high and low energies, constraining the shape of the efficiency curve.

3.2 BGO Backgrounds

3.2.1 A BGO Detector Underground

Before studying the BGO detector using external gamma ray sources, the background spectrum measured with the BGO detector in an underground location can be analyzed in order to learn about the detector response and to study the sources of background in this detector. With this knowledge, measures to further reduce this background can be assessed, for example when planning for a concrete experiment.

Sum spectra of background measurements with the BGO detector in different locations are shown in Figure 3.1. The underground location at LUNA and the strongly reduced flux of cosmic rays greatly improves the background in the energy region above 3 MeV. Whereas the background spectrum on surface is smooth and only slowly falling in this energy region, the background spectrum underground drops off more steeply until about 5-6 MeV, followed by a plateau up to approximately 10 MeV, then dropping down to even lower values.

Adding a lead shielding to the detector setup underground further reduces the background, in the region below 3 MeV. The peaks corresponding to the gamma lines of ^{40}K and ^{208}Tl at 1460 keV and 2615 keV respectively are apparent in the two unshielded spectra, but not visible in the shielded spectra. Instead the shielded spectra exhibits two features corresponding to the 2340 keV and 1633 keV states in ^{207}Pb that are populated by the electron capture of ^{207}Bi , which is known intrinsic background to BGO detectors [43, 44] and decays by electron capture with a half-life of 31.55(4) years.

Comparing the two background spectra for unshielded detectors in Figure 3.1, they largely agree, except for a divergence in the energy range between 3 and 6 MeV. The reason for this discrepancy is attributed to the data acquisition systems used in these measurements. The setup that was used for the $^{25}\text{Mg}(p, \gamma)$ measurements used a list mode data acquisition system, to acquire the energy information for each channel separately and create the sum spectrum by adding the single crystal energies. Presumably the time window in which single crystal events were grouped into coincidence events was set to a larger value, increasing the probability for accidental coincidences, i. e. the summing of the energy deposition of two independent physical events. For the $^{14}\text{N}(p, \gamma)^{15}\text{O}$ campaign, the analog sum of the six PMT signals was amplified and recorded with a multichannel analyzer as described in [45], leading to a short time window for accidental coincidences.

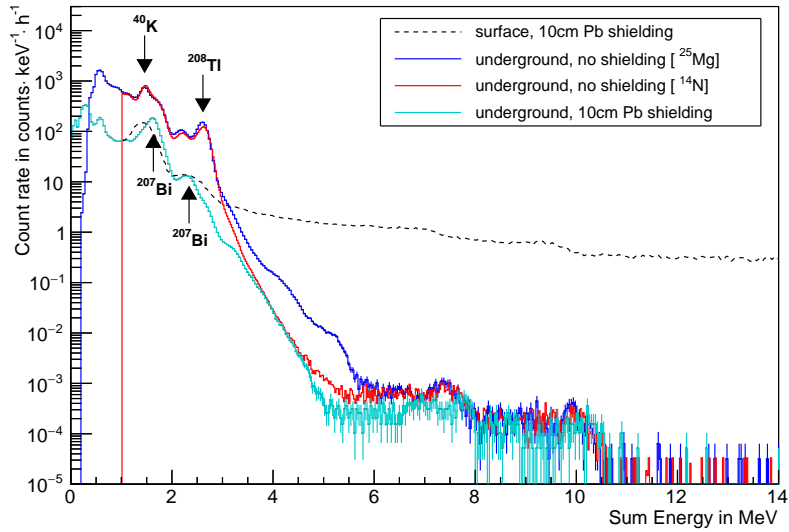


Figure 3.1: Background (sum) spectrum of the BGO detector on surface (shielded by lead) [8], underground without shielding (measured during the $^{25}\text{Mg}(p, \gamma)$ studies [35], and during the $^{14}\text{N}(p, \gamma)$ studies [45]), and with the new lead shielding and data acquisition system in this work.

The fact that the unshielded background spectrum acquired in the $^{14}\text{N}(p, \gamma)^{15}\text{O}$ campaign and the shielded background in the course of this work agree in the region around 4 MeV is an indication that this background level is associated with intrinsic backgrounds rather than pile-up. Without a precise model about the intrinsic background contributions, it can also not be ruled out completely that a combination of a larger random coincidence probability and lower background event rates compensate by chance, but it appears unlikely, given that the background rate below 3 MeV was reduced by almost one order of magnitude, and the accidental pile-up rate scales with the background rate to the power of two.

Figure 3.2 shows a simplified model from a simulation of the main contributions to the sum background spectrum of an unshielded detector. In general, the spectral shape appears to be described very well by this model. On closer inspection, intrinsic backgrounds are overestimated as can be seen when comparing their contribution in this model to the background spectrum later acquired with shielding. The model prediction is larger compared to the measurement in the energy region of 1 MeV, and smaller around 3.5 MeV and 5.5 MeV. The intrinsic background uses a fixed Birks' constant for α quenching (from [46]). The radioactive decay chains are assumed to be in equilibrium, but coincidence summing effects of bismuth polonium events (with very short Po half lives) are not considered. These coincidences could provide an explanation for the deficit

in the 3.5 MeV region. As the 3.5 MeV energy region in the sum spectrum also constrains the intrinsic background contribution from steel, a correct treatment of the coincidences could reduce the assumed intrinsic background of the detector casing. The challenges of describing the intrinsic backgrounds are elaborated in more detail later in this section.

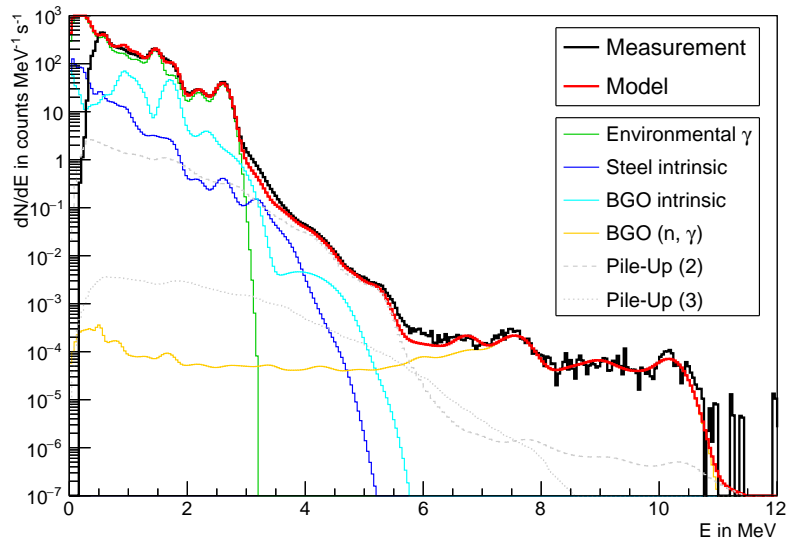


Figure 3.2: Approximate model for the unshielded background (sum) spectrum of the BGO detector underground.

3.2.2 Backgrounds from Radiative Thermal Neutron Capture

To confirm that the background in the region between approximately 6 and 11 MeV is dominated by events from radiative neutron capture, the aim was to develop a model to describe the spectrum in this energy region.

For this model, thermal neutrons were considered as the main contribution to the background signal. The radiative capture, (n, γ) , has large Q values for many of the materials that are used in the detector, and the gamma rays emitted following that reaction can be registered as events with large sum energies.

At the heart of the model is a Monte Carlo simulation that consists of two steps. The first step determines where thermal neutron capture occurs in the setup. To this end, neutrons with a thermalized energy distribution were generated with isotropic directions, homogeneously on the surface of a sphere around the detector geometry. These neutrons were then propagated until they were captured or left the global volume of the simulation. For each (n, γ) capture event, the position of the capture vertex and the nuclide on which the capture reaction occurred was saved. The second step then used these capture vertices to simulate gamma rays from the deexcitation of the

3 Detector Characterization

daughter nucleus, and save the energy deposition in the sensitive detector volume that was caused by this decay. For this step, a custom particle generator was written that simulates the gamma rays from deexcitation according to the level scheme and gamma ray branchings of the daughter nucleus. The level schemes were implemented as far as known, using the Nuclear Data Sheet compilations for the respective elements (as collected in [16]). In case of unknown branchings for single levels, a direct transition to the ground state was assumed.

In a last step, the energy spectra were summed up and smeared with the energy resolution of the detector. A global scale factor was applied to the resulting sum spectrum, to match it to the measured spectrum. Figure 3.3 shows the comparison of the measured (unshielded) background spectrum with the simulation, showing good agreement in the energy region above 8 MeV. With the results taken directly from the simulation, there is a deficit of counts in the 7.5 MeV region, where the contribution of $^{56}\text{Fe}(n,\gamma)$ ($Q = 7.65$ MeV) is most prominent. Scaling the contribution of iron by a factor of two yields a much better agreement of the fit with the data. The origin of this discrepancy has not been determined. One possibility would be contributions from other steel components close to the setup during the measurement, which was not included in the simulation.

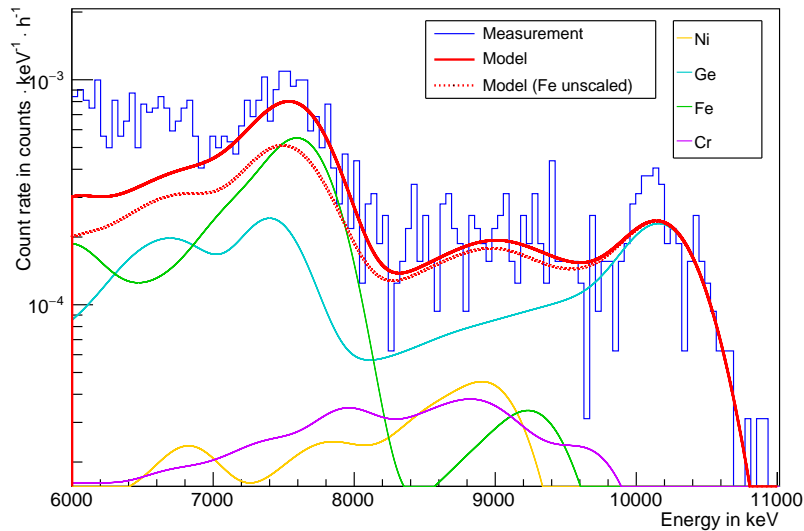


Figure 3.3: Comparison between the measured background (sum) spectrum for an unshielded detector and the simulated background induced by thermal neutrons.

With the simulation in agreement with the measurements, the influence of shielding options on the neutron background can be studied. Three cases are considered here:

a lead shielding as installed and described in section 2.6, a 22 mm thin layer of (5% w/w) borated polyethylene around the side of the cylinder (filling the rim, i.e. not extending the outline of the detector), and the combination of both. The results are shown in Figure 3.4. Adding the lead shielding reduces the number of neutron capture events by a factor of 2.2 in the simulation, which is consistent with the observation of the background spectra (Fig. 3.1). The background reduction affects all elements by approximately the same way, as the lead shielding encloses the detector and hence the neutron flux from all directions is attenuated. The contribution from neutron capture on lead to the gamma spectrum is minor. The shielding with borated polyethylene is much more effective, given its size compared to the massive lead shielding. With the simple geometry that the shielding only covers the side of the detector, the shielding reduces the captures on germanium more strongly than on steel (where the front and the back part of the detector are exposed). Hence the background suppression is more noticeable at high gamma ray energies. The overall reduction between 6 and 11 MeV is about a factor of 3.1. If required, a more elaborate geometry could also partially cover the front and back sides, further reducing the number of neutron captures on the detector housing. The combined shielding of lead and borated polyethylene has the largest reduction of the thermal neutron capture background, with a factor of 6.3.

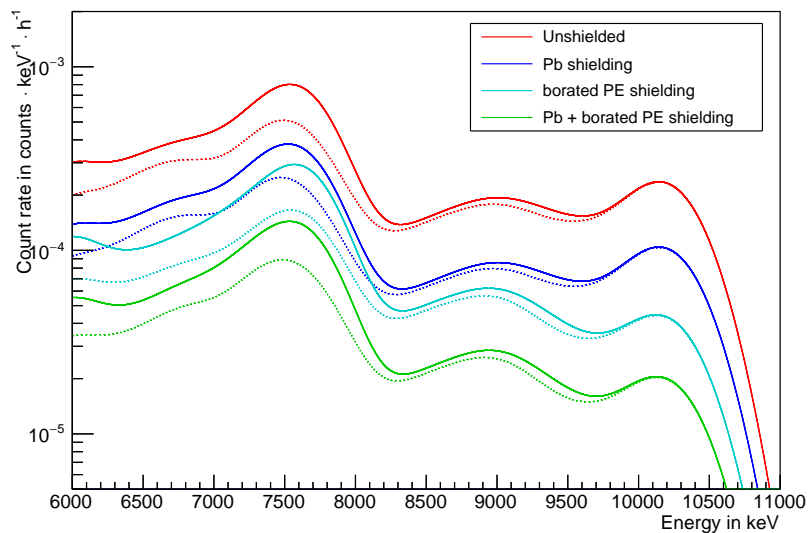


Figure 3.4: Comparison of the simulated neutron background spectra for different shielding options.

3.2.3 Towards a Model for Intrinsic Backgrounds

A full description of the observed background spectra would be desirable to assess the possibilities and limitations of further background reduction for this detector. For this, intrinsic radioactive backgrounds in the materials of the detector need to be considered. Apart from ^{207}Bi , which was already discussed above, nuclides from the primordial decay chains and ^{40}K would be prime candidates to be considered. The model of the detector response will need to take into account that the light output of the detector in response to the energy deposition from an alpha particle or heavier ions is lower than that observed for electrons. Birks' law has been successfully applied to measurements with BGO crystals [46, 47], although these experiments typically do not measure in the low-energy regime of few MeV as it occurs in case of the radioactive decay of intrinsic backgrounds.

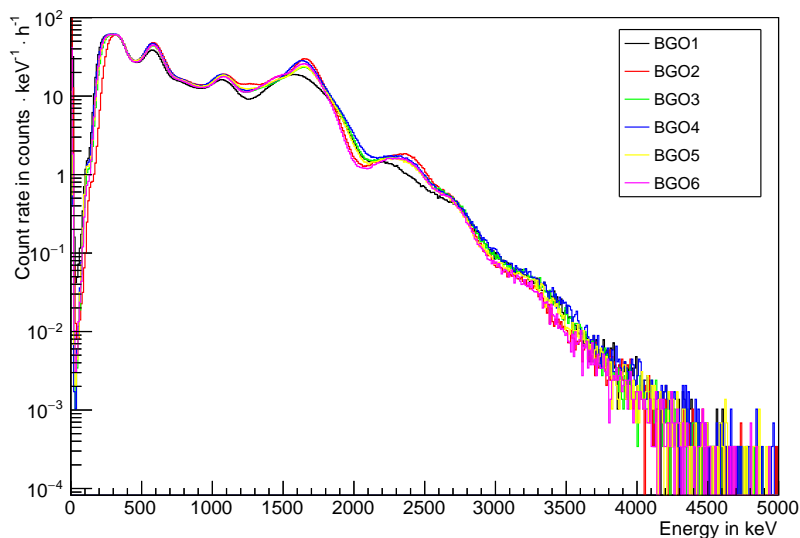


Figure 3.5: Comparison of single crystal background spectra for environmental background run with the BGO detector shielded by 10 cm of lead.

Considering intrinsic backgrounds, a description is further complicated by the apparently different characteristics of the crystals of the detector. Figure 3.5 shows a comparison of the spectra of six single spectra in a shielded background run. Crystal number one in particular shows much less prominent peaks in the energy regions associated with ^{207}Bi , implying a lower intrinsic contamination of this nuclide in this detector. A full model will need to accommodate for such differences, which, however, will largely increase the number of parameters in the model. Another issue can be nuclide concentrations out of equilibrium in the decay chains [48].

3.2.4 Consequences and Outlook

The 10 cm of lead shielding appear to provide sufficient shielding against environmental gamma rays for the underground location, with the features of intrinsic ^{207}Bi backgrounds clearly visible by in the spectrum. These intrinsic background from the BGO crystals will be irreducible when using this detector, except for the contribution from ^{207}Bi that will decay slowly in time.

In the context of $^{23}\text{Na}(p, \gamma)$, the Q value of the reaction places the region of interest above the region of background from thermal neutron capture. For other experiments, however, where a background reduction between approximately 6 and 11 MeV could enhance the experimental sensitivity significantly, a shielding against thermal neutrons (e. g. with borated polyethylene or boron carbide) should be taken into consideration. On a side note, shielding thermal neutrons with cadmium would not be efficient to reduce the gamma ray background, due to the large Q -value of $^{113}\text{Cd}(n, \gamma)$ of about 9 MeV, and the gamma rays following the neutron capture on cadmium; depending on the geometry it might actually increase the detector sensitivity to thermal neutrons.

The origin of the background in the intermediate energy region could be resolved precisely only by a full background model that takes the intrinsic background, and the differences in this background from crystal to crystal, properly into account. With such a model, one could then infer whether further efforts to improve the background rates are feasible (e. g. replacing the casing of the detector with a more radiopure material), or whether the intrinsic radioactivity of the BGO crystals is the limiting factor for the background in this energy region.

3.3 BGO Detector

In the calibration of the BGO detector, calibration measurements with the radioactive sources and the (p, γ) reactions discussed in section 3.1 were compared to the simulated efficiencies to validate the simulation. The detection efficiencies at the full energy peak in the sum spectrum were found to be in good (5-10%) agreement with the simulated values, considering the uncertainties of the resonances and precise source location used for calibration.

For a better understanding of the characteristics of the detector, the graph in Figure 3.6 shows different gamma ray detection efficiencies with this detector (and the solid target setup) as a function of gamma ray energy. The total efficiency, i. e. the probability to get a non-zero energy deposition in any of the crystals rises sharply to reach a maximum at about 1 MeV. Below this energy, absorption in the material between the target and the active detector volume is the dominant influence on the total detection efficiency. Towards higher energies, this efficiency has only a weak energy dependence, due to the

3 Detector Characterization

large thickness and gamma ray interaction cross sections of the BGO crystals. The difference in total efficiency between this “plateau” and 100% is mostly due to the solid angle coverage of the target with active detector material. Regardless of their energy, gamma rays can escape through the borehole and go completely undetected. The full energy deposition efficiency in the complete active detector volume also peaks at around 1 MeV but then falls off slowly, owing to the decreasing gamma ray interaction cross section. Comparing the full energy deposition efficiency with the probability to deposit the full gamma ray energy in one crystal or two adjacent crystals, it is apparent that the majority of the full energy deposition events are of this type. The difference between the two efficiencies, i. e. the probability that a single gamma ray deposits its full energy in three or more different crystals, is small but increases with energy. Correspondingly, the probability for a full energy deposition in a single one of the crystals relative to the full energy deposition efficiency for the full detector decreases with gamma ray energy.

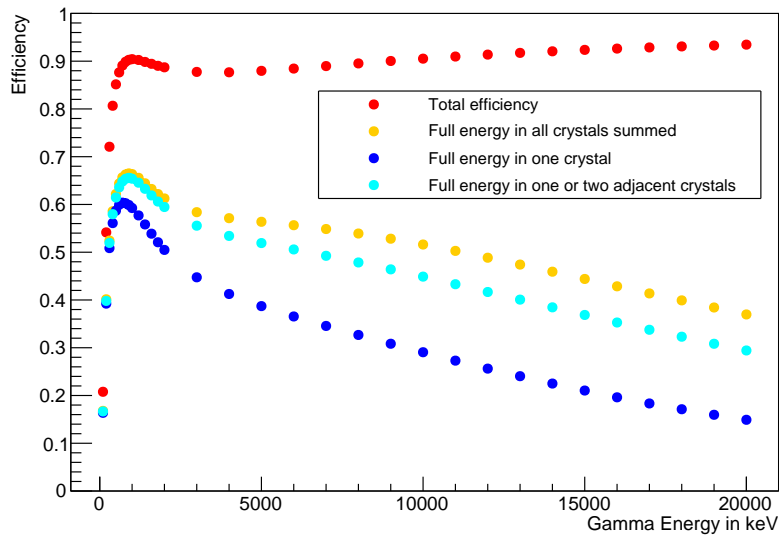


Figure 3.6: Gamma ray detection efficiency of the BGO detector as obtained in the Monte Carlo simulation.

The main signature for the measurement of a (p, γ) reaction with the BGO detector is the full energy deposition of all gamma rays in a cascade. For example, searching for a resonance populating a level E_x which deexcites through a gamma ray cascade, the expected signal is at E_x in the sum spectrum. As a consequence of the relatively weak energy dependence of the full energy deposition efficiency above a certain threshold, the full energy deposition probability for gamma ray cascades of a fixed total energy E_x is less sensitive to the energies of the single gamma rays (except for the case in which at least one has a very low energy), but more to the number of gamma rays. The detection

efficiency is the largest for a direct transition to the ground state, i. e. a single gamma ray, and decreases with an increasing number of gamma rays. If the branching ratios of a level that is under study are unknown, which is the case for the level corresponding to the 144 keV resonance in $^{23}\text{Na}(p, \gamma)$, the uncertainty of the detection efficiency in the sum spectrum is fairly large, depending on the assumed multiplicity distribution of the gamma ray cascades in the deexcitation of this level.

Another aspect of the detector response that can be studied in the simulation is the detection efficiency as a function of the beam spot. Figure 3.7 illustrates the position dependence of the full energy peak detection efficiency for single gamma rays of different energies, and for the deexcitation of the ^{24}Mg excited state that is populated in the 309 keV resonance in $^{23}\text{Na}(p, \gamma)$. For a single crystal, the total gamma ray efficiency shows a characteristic position dependence, with the difference between positions towards and away from the crystal about $\pm 15\%$ with respect to the center of the target. Considering the average full energy deposition efficiency of all six crystals, the position dependence becomes more radially symmetric. The maximum efficiency is realized for events at the center of the target, and falls off slightly towards the edge of the target. For a single gamma ray of 1 MeV energy, the efficiency at the very edge of the target is about 7% lower, relative to the center of the target. For higher energies, the position dependence is weaker, with the efficiency at the edge about 4% lower than at the center. For the single gamma rays, the full energy peak efficiency for the full crystal shows a behavior very similar to the average of the single crystal efficiencies. For gamma ray cascades, as a result of the multiplicity of the gamma rays, the position dependence is increased. The variation in the single crystal full energy deposition efficiency is very large for a cascade, but also not the typical scenario in the detection of cascades. The position dependence of the sum spectrum full energy deposition efficiency is also enhanced for the cascade with respect to the single gamma ray. In the cascade considered in the example, the efficiency decreases by up to 10% towards the edge of the target. Considering the typical extension of the beam spot, imprecise knowledge of the beam spot position may lead to variations of the detection efficiency on the order of 5%.

3.4 HPGe Detector

Calibration measurements for the HPGe detector were performed with the radioactive calibration sources, the resonance in $^{14}\text{N}(p, \gamma)$, and the two resonances in $^{27}\text{Al}(p, \gamma)$. The calibration measurements were performed for different detector distances. The closest distance, which was used for most measurements, is referred to as “0 cm” position in the following. For the other positions, the distances to this reference position (measured along the rails under the detector setup) were 5 cm, 10 cm, 15 cm and 20 cm.

For the description of the full energy peak efficiency ε_{FEP} and total efficiency $\varepsilon_{\text{total}}$ for

3 Detector Characterization

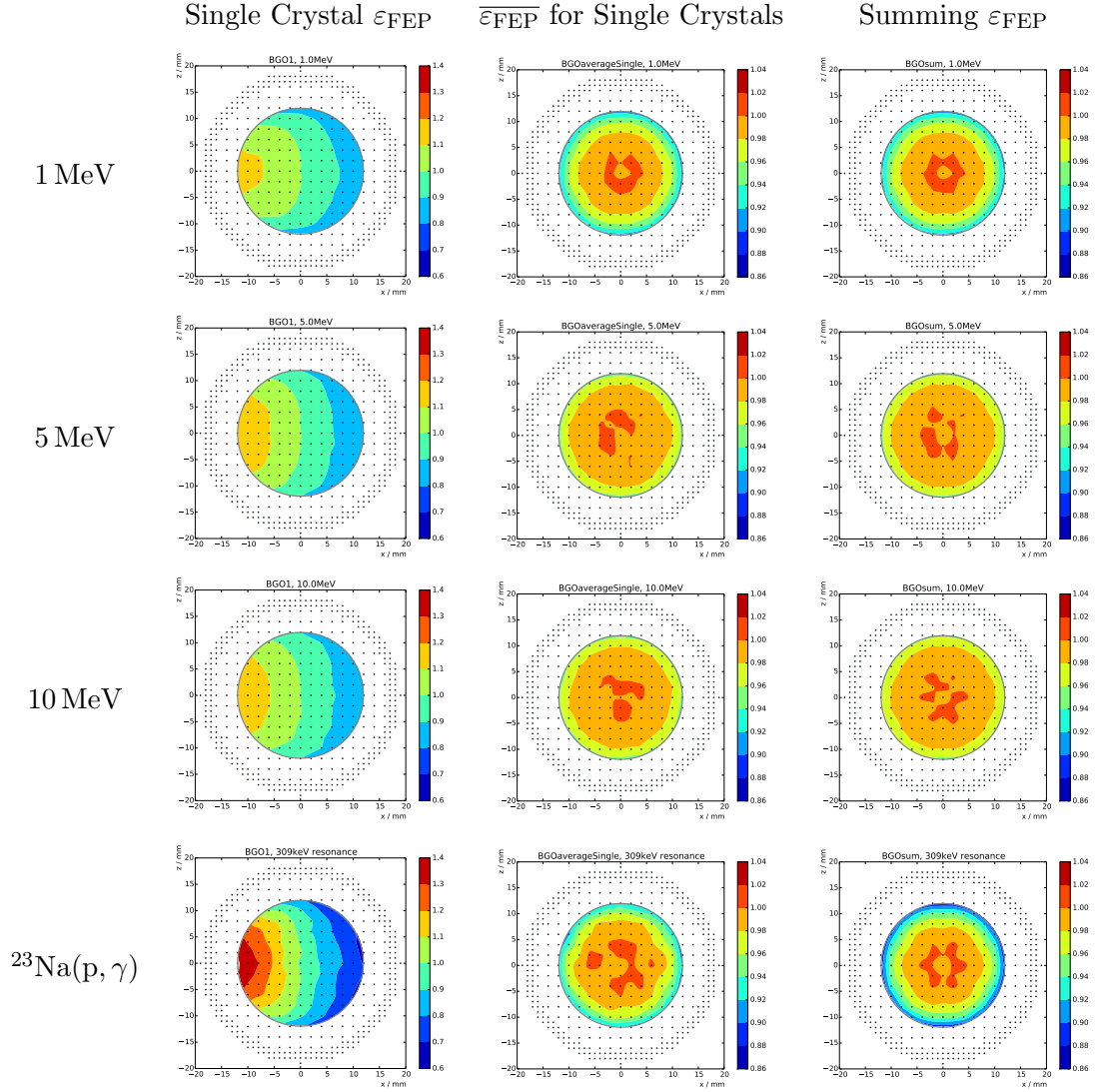


Figure 3.7: Position dependence of the full energy deposition efficiency for single gamma rays and the gamma cascades from the deexcitation of the 11987.72 keV level of ^{24}Mg ($E_p = 309$ keV resonance in $^{23}\text{Na}(p, \gamma)$). Left: single crystal (in $-x$ direction), Middle: average of the efficiency of the six crystals, Right: full energy peak efficiency for all crystals (sum spectrum). Note the different scale in the left column of plots.

a single gamma ray of energy E with the detector at a distance d , an empirical model is used, which has already been applied to a setup with the same detector in the past [41]:

$$f(E, d) = \frac{1 - \exp\left(\frac{d+d_0}{a_0+b_0\cdot\sqrt{E/\text{keV}}}\right)}{(d+d_0)^2} \quad (3.1)$$

$$\varepsilon_{\text{FEP}}(E, d) = f(E, d) \cdot \exp(a + b \cdot \ln(E/\text{keV}) + c \cdot (\ln(E/\text{keV}))^2) \quad (3.2)$$

$$\varepsilon_{\text{total}}(E, d) = \varepsilon_{\text{FEP}} \cdot \exp(-k_1 - k_2 \cdot \ln(E/\text{keV}) - k_3 \cdot (\ln(E/\text{keV}))^2) \quad (3.3)$$

This model has 9 free parameters: $a, b, c, a_0, b_0, d_0, k_1, k_2, k_3$, which were determined in a fit to the measured data as described in the following.

Few additional parameters were introduced: for the calibration sources, which were mounted on top of a backing, the active volume is not exactly on the surface of the backing as for the nuclear reactions, but at slightly larger distances from the detector. This was reflected by introducing additional parameters D_0^{Cs} and D_0^{Co} to the fit, which were set to the values estimated from the geometry of the source, but allowed to vary to some extent to account for the uncertainty of the position of the activity within the source. A scale factor was introduced for the activity of each radioactive source, to allow to account for the uncertainty of the activity calibration. These factors, however, were found to be very close to unity in the end, as the vendor data sheets of the sources state an uncertainty of the activities of only 3 % (95% confidence level), much smaller than the uncertainty of the resonance strengths or the influence of the position uncertainty of the radioactive sources at close distances. For the reactions used in the calibration, a scale factor on the reaction yield was introduced and allowed to vary from unity, considering the uncertainty of the resonance strength of each reaction.

The parameters of the model were determined by a maximum likelihood fit. For the selected lines of the gamma spectra, the full energy peak detection probability was determined by:

$$P_{\text{FEP}}^{\text{measured}} = \frac{N_{\text{FEP}}^{\text{measured}}}{\text{Number of reactions or decays during the measurement}} \quad (3.4)$$

Where $N_{\text{FEP}}^{\text{measured}}$ is the number of counts in the full energy peak of the spectrum, and the denominator is the number of reactions (derived from charge and yield) in the case of a resonance, or the number of decays (derived from starting time and duration of the measurement) in case of a radioactive source. To derive the model prediction for P_{FEP} , the gamma ray branching scheme has to be considered to properly account for

3 Detector Characterization

summing effects. Two types of cascades can contribute to the full energy peak detection probability of a gamma ray with energy E_γ . The typical case are cascades that include the transition with the energy E_γ , which yield a full energy event if no other gamma ray deposits any energy in the detector. For such a cascade C_o , the probability for a full energy deposition is thus given as:

$$P_{E_\gamma}^{C_o} = \varepsilon_{\text{FEP}}(E_\gamma) \cdot \prod_{E_j \neq E_\gamma} (1 - \varepsilon_{\text{total}}(E_j)) \quad (3.5)$$

Here, the product j includes all gamma rays in the cascade except for the one with E_γ . The second type of cascades that can contribute to the full energy peak of E_γ are those where the energies of two other transitions add up to E_γ , which is typically the case for situations as shown in Figure 2.3, where the transition corresponding to E_γ can also occur as a two-step process. To obtain a full energy event with such a cascade, the two participating gamma rays must deposit their full energy, all other gamma rays in the cascade may not deposit any energy. The probability for a Cascade C_i follows as:

$$P_{E_\gamma}^{C_i} = \varepsilon_{\text{FEP}}(E_1) \cdot \varepsilon_{\text{FEP}}(E_2) \cdot \prod_{E_j \notin \{E_1, E_2\}} (1 - \varepsilon_{\text{total}}(E_j)) \quad (E_1 + E_2 = E_\gamma) \quad (3.6)$$

In principle this consideration can be generalized to the summation of more than two gamma rays. In practice, however, this effect is usually negligible due to the small values of ε_{FEP} .

The sum of these probabilities for all cascades C_o affected by summing out and all cascades C_i contributing via summing in, weighted by their respective probabilities to occur in the decay scheme, yields $P_{\text{FEP}}^{\text{model}}$ predicted by the model.

Uncertainties in the branching ratios of the level scheme reflect in uncertainties of these model predictions. They are determined by a Monte Carlo approach. The transition probabilities are sampled according to the given mean values and uncertainties, and the resulting value for $P_{\text{FEP}}^{\text{model}}$ is calculated. Repeating this procedure many times, a distribution for $P_{\text{FEP}}^{\text{model}}$ is obtained, from which a central value and an uncertainty can be derived.

Considering the (statistical) uncertainty of $P_{\text{FEP}}^{\text{measured}}$ and the uncertainty of $P_{\text{FEP}}^{\text{model}}$, the likelihood \mathcal{L} of the calibration data set can be derived for a set of model parameters. The parameter set minimizing $-\log \mathcal{L}$ was determined by numerical minimization.

The results for the model with these parameters are shown in Figure 3.8. The solid line represents the full energy peak efficiency as a function of energy, predicted by the model. The data points correspond to P_{FEP} divided by the intensity of the respective gamma ray. Data points under the solid curve are thus primarily affected by summing out, whereas the points above the curve are largely determined by summing in. The data

point at 10088 keV (^{27}Al , 293 keV resonance) for example is dominated by summing in at 0 mm detector distance. Hence this data point depends more on the full energy peak efficiency at the lower energies of the two contributing gamma rays, rather than ε_{FEP} at 10088 keV.

The full energy peak efficiency can also be determined directly from the Monte Carlo particle transport simulation. Comparing the results from the simulation of the detector response to a source at the center of the target yields efficiencies that are systematically too high, as shown in Figure 3.9, when using the nominal geometry. Increasing the dead layer in the front and outside of the detector from the nominal 0.7 mm to 1.6 mm improves the agreement between simulation and empirical fit to $\pm 5\%$ in the energy range between 1 and 12 MeV. There appears to be a systematic difference in the energy dependence of the efficiency taken from the simulation and the empirical formula. This also shows, if one tries to fit the empirical model, equations (3.1) and (3.2), to data sets from simulations at different distances (e. g. the distances present in the measured calibration data set): the empirical fit function does not describe the simulated data well at all distances, and systematic deviations similar to those in Fig. 3.9 are visible. Hence the empirical model might not be completely adequate for the description of the efficiency as a function of energy and distance. Within the uncertainty range of the calibration data set, however, these differences cannot be distinguished.

The reproduction of the energy spectrum outside the full energy deposition peaks is illustrated in Figure 3.10, comparing the simulated spectrum for $^{14}\text{N}(p, \gamma)$ calibration measurements with simulated spectra. The features of the spectrum are well reproduced, and the difference between simulation and measurement are comparable to the differences in between experimental runs.

The simulation allows to systematically study the dependence of the full energy peak efficiency on different parameters. One interesting parameter is the dependence on the position of the gamma ray source. As already discussed in the section about the BGO detector simulations, the beam spot is not a single point at the center of the detector but rather spread out over an area of several millimeters in diameter. Simulating gamma ray sources at various points on the target surface allows to study the variation of the full energy peak efficiency, for example relative to the central position. Results for gamma ray energies of 1, 5 and 10 MeV are visualized in Figure 3.11. Moving away from the center, the FEP efficiency decreases. This is plausible, as a gamma ray emitted at an off-center position has a higher probability to traverse the brass target holder, as opposed to the water cooling behind the target, before reaching the detector and is thus more prone to interactions in the holder material. The effect is the strongest at lower gamma ray energies. For an energy of 1 MeV, the efficiency changes by up to 10% when moving very close to the edge of the accessible target area. The variation in the central area

3 Detector Characterization

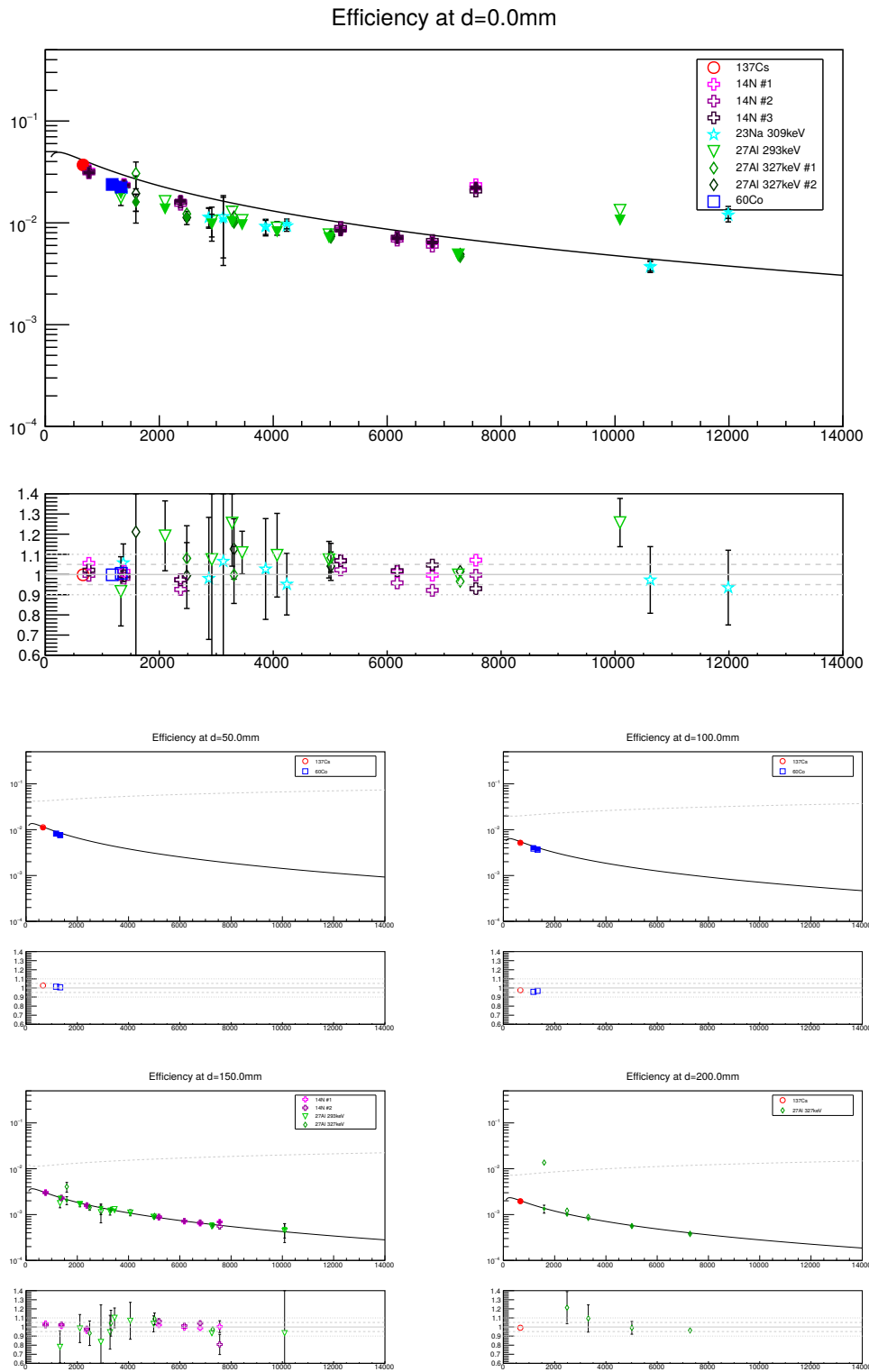


Figure 3.8: Results of the empirical efficiency calibration: The solid line is the full energy peak efficiency for a single gamma as a function of energy for the different energies. The hollow markers are data points, the full markers model predictions. The bottom halves of the plots show the relative deviation of the data points with respect to the model prediction.

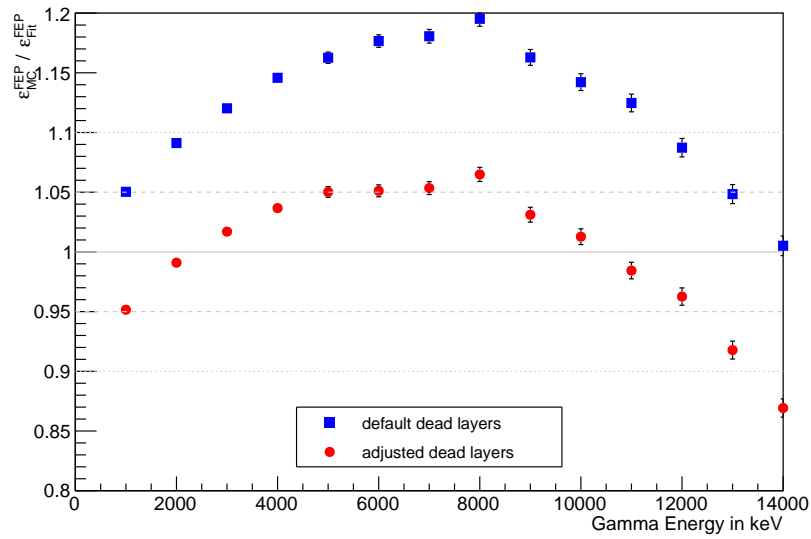


Figure 3.9: Comparison between full energy peak efficiency for single gamma rays according to the empirical fit shown in Fig. and results obtained with a Monte Carlo Simulation.

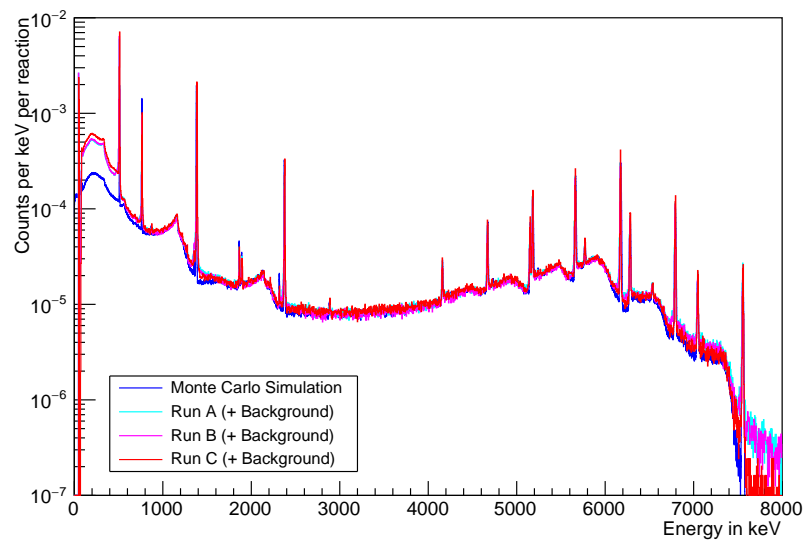


Figure 3.10: Simulated and measured spectra for the resonance in $^{14}\text{N}(p, \gamma)$ that was used for the calibration.

3 Detector Characterization

is more on the order of 5%, though. The observed lower experimental FEP efficiency, compared to the Monte Carlo simulation for a source at the center of the target, could hence also be in part due to the extension and position of the beam spot. The effect can also be an explanation for the slightly different spectra observed for measurements of the same $^{14}\text{N}(p, \gamma)$ resonance that were observed in Figure 3.10.

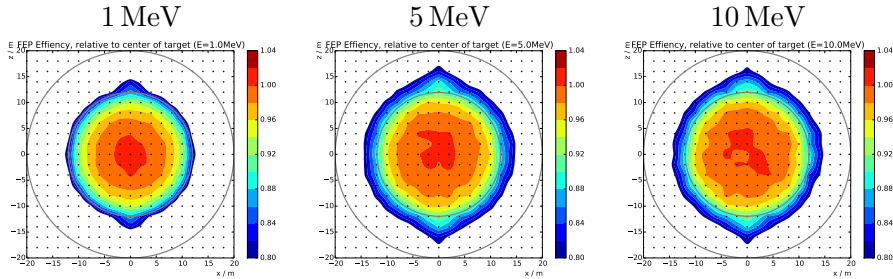


Figure 3.11: Variation of the full energy peak efficiency for gamma rays of different energies, as a function of position on the target surface, as obtained from simulation. The two circles indicate a metal ring holding the target, i. e. only the inner part of the smaller circle may be exposed to the beam.

It is interesting to note, that also the efficiencies determined in the $^{14}\text{N}(p, \gamma)$ calibration measurements at 0 mm detector distance vary by about 5-10%, which gives an impression of the systematic uncertainty of the efficiency in a (p, γ) measurement with this setup. Finally, the empirical fit was adopted for the analysis in this work, and a relative uncertainty of 10% was assumed for the full energy peak efficiency over the full energy range.

4 Data Acquisition and Analysis

4.1 Sodium Target Development and Studies

4.1.1 Requirements

Proper targets are an essential part of a successful direct cross section measurement. Such targets need to meet a number of requirements. They need to have a well-defined stoichiometry, and preferably a large contribution of Na to the effective stopping power (eq. (1.12)). Another requirement is that the stoichiometry as a function of depth (e. g. defining the thickness of the target) needs to be known. The stoichiometry also needs to be stable, i. e. it should only change little under the bombardment with an intense proton beam, and the changes should be slow and continuous. For practical purposes, the targets should withstand accumulated charges of several Coulomb before the changes in stoichiometry become too rapid or too large. In practical terms, the target should conduct heat well enough to allow for effective cooling. The electrical resistance also needs to be sufficiently low, to measure the beam current and avoid charging the target electrically.

4.1.2 Previous Experiments

A variety of sodium targets has been used in previous experiments that studied reactions on ^{23}Na . The natural abundance of ^{23}Na is 100% (it is the only stable isotope of sodium), so that isotopic enrichment is not required. Table 4.1 gives examples for past studies for which different types of sodium targets have been used.

Target Type		Example Works
Implantation	Implanted Na	[49], [50], [51]
Evaporation	Oxidized Na	[20]
	NaOH	[52]
	NaCl	[52], [53], [54]
	NaCl + Al	[21], [22]
	NaBr	[53], [55], [20]
	Na ₂ WO ₄	[56], [55]
	Na ₂ P ₄ O ₇ + Al	[21], [22]
	Na ₂ SO ₄	[57]

Table 4.1: Target production techniques used in previous experiments on ^{23}Na .

One group of targets is produced by evaporation of sodium compounds onto backing materials (such as tantalum or copper). As an alkali metal, elemental sodium oxidizes when exposed to air and reacts strongly with water. A number of sodium salts are easier to handle than elemental sodium. One disadvantage the majority of these salts share is that they are hygroscopic, i. e. when exposed to humidity (for example in the air), their stoichiometry changes.

Another group are targets produced by implantation of sodium ions into a backing material. The production of targets with favorable properties has been reported [49], and the stability of such targets under proton bombardment was studied in [51]. However, recent attempts to produce targets by implantation [25] yielded targets with low sodium contents or inhomogeneous target profiles.

4.1.3 Choice of Target Type and Material

As a large sodium content and stability are key issues for this experiment in which low reaction yields are expected, evaporated targets were chosen. Taking the experience from earlier sodium experiments into account, three compounds were studied in more detail in the course of this experiment: NaCl, Na₂SiO₃ and Na₂WO₄.

NaCl is convenient as it is readily available, less hygroscopic than the other two compounds and comparably easy to evaporate. The stoichiometry is favorable as well, with only one inactive atom and $Z_{\text{Cl}} = 17$ per sodium atom. The downside is its limited stability under intense beams, which would have only allowed to use rather thick targets for limited times per target.

Na₂WO₄ is a material proven in previous experiments [25]. Unfavorable in this compound is the larger effective stopping power due to the contributions of four oxygen ($Z_{\text{O}} = 8$) and one tungsten ($Z_{\text{W}} = 74$) atom for every two atoms of sodium. Sodium tungstate is hygroscopic – typically the material is commercially available as sodium tungstate dihydrate, Na₂WO₄·2 H₂O.

Compared to Na₂WO₄, sodium metasilicate Na₂SiO₃ has the advantage of a slightly smaller effective stopping power. It appears to be more hygroscopic and needs to be heated up very carefully during evaporation to achieve a controlled evaporation. Due to the difficulties during evaporation, only a few thick targets have been produced, which however showed favorable characteristics in terms of durability and yield.

Considering all the factors, the large majority of the measurements presented in this work have been performed with Na₂WO₄ targets, very few with Na₂SiO₃. Examples for the behavior of targets for the three different materials under irradiation are shown in subsection 4.1.6.

Material	Na	Na ₂ O	NaCl	NaBr
$\varepsilon_{\text{eff.}}$ in eV/10 ¹⁵ $\frac{\text{atoms}}{\text{cm}^2}$	14.5	19.9	32.0	36.9
Material	Na ₂ SiO ₃	Na ₂ SO ₄	Na ₂ WO ₄	Na ₂ P ₄ O ₇
$\varepsilon_{\text{eff.}}$ in eV/10 ¹⁵ $\frac{\text{atoms}}{\text{cm}^2}$	38.5	46.0	52.1	86.7

Table 4.2: Effective stopping power at $E_p = 300$ keV for sodium in different compounds as calculated from stopping power tables produced with SRIM2013 [5].

4.1.4 Backing Material and Treatment

Tantalum has been used and established as a reliable backing material in various past experiments at LUNA and other facilities, providing the mechanical support for the target material. With its atomic number of $Z_{\text{Ta}} = 73$, the Coulomb barrier of tantalum is so high that spurious reactions on Ta are not of concern at the low energies at LUNA. The low heat resistivity of tantalum allows to cool the target effectively by water cooling the back side of the target.

Backings were made out of 0.4 mm thick tantalum sheets, and had the form of discs of about 40 mm diameter with a ring of holes towards the outer rim of the disc to mount the targets. After machining, the target surface was cleaned chemically with isopropyl alcohol to remove substances on the surface. In most cases the backing was additionally etched with either citric acid, a mixture of sulfuric, hydrofluoric and nitrous acid, or with sodium hydroxide. The treatment involving hydrofluoric acid was avoided for targets used at higher energies, when beam-induced backgrounds on ¹⁹F were a concern. The backings were then transferred to the evaporation facility.

4.1.5 Target Production Procedure

The evaporation of the target material onto the backing was performed at the Institute for Nuclear Research (MTA Atomki) in Debrecen (Hungary). In a first step, the backing was heated up under vacuum by driving an electric current through it. This resistive heating served the purpose to facilitate the evaporation of possible remaining impurities on the backing.

For the evaporation, the sample material was placed in a crucible and electrically heated under vacuum, with the backing mounted over the crucible. Initially the backing was covered to avoid premature deposition of materials in the initial phase of heating up the raw material. The crucible was heated up slowly, while watching the sample material. For the hygroscopic sodium salts where hydrates serve as raw material, first the water of crystallization was driven out by the increasing temperature. When this process finished visibly and a steady stream of evaporation had been achieved, the temperature was kept constant and the cover over the backing was removed to begin depositing the

evaporated material. The deposition was monitored using a quartz crystal microbalance close to the target. When the desired grammage of target material on the surfaces had been reached, the target was covered again and the heating was stopped.

After the target had cooled down, it was transferred to a vacuum storage container to avoid deterioration of sodium sample surface, e. g. by hydration on contact with humidity.

4.1.6 Target Analysis In Situ

The standard method used to evaluate the target composition in situ in this experiment was by nuclear resonance analysis. The narrow resonances in $^{23}\text{Na}(p, \gamma)$, typically the one at 309 keV, occasionally also the one at 251 keV, were used to repeatedly scan the profile of the targets. Repeated scans in between longer measurements were used to monitor the changes in target composition during bombardment.

The principle of a resonance scan is as follows: consider a single narrow resonance at a proton energy of $E_{\text{res.}}$. If a target is bombarded with protons with an energy of $E_p = E_{\text{res.}} + \Delta E$, the proton will penetrate the target material, losing energy in the process. When the proton has lost ΔE , the resonance cross section peaks sharply. Therefore the observed resonance yield is determined by the reactions at a depth d in the target that corresponds to the energy loss ΔE . As the resonance yield depends on the effective stopping power, resonance scans can provide indirect composition information. Determining the resonance yield as a function of the proton energy E_p , one can probe the effective stopping power as a function of depth. Although the effective stopping power yields only indirect information about the target composition (as no direct information is obtained on the passive components), they are a valuable tool to study the homogeneity (in depth) and stability of the target composition in situ. Ideally the resonance scan shows a sharp rising edge, followed by a plateau region (homogeneous target region). Usually these profiles finish with a smooth tail, indicating that the contribution of the resonance does not drop off sharply, but fades out more slowly. This effect can be caused by energy straggling of the beam in the target material, or the diffusion of active target material into the backing. A surface roughness of the backing (before the evaporation of the target material) is another possible influence that can contribute to the observed shape of the tail of the resonance scan.

The profile shape changed as a consequence of the bombardment of the target. Often a small and relatively fast improvement in the front of the target plateau (i. e. a steeper rise) was observed in the initial phase of bombardment. In the further course of the irradiation, the length of the plateau decreased continuously, and at later stages the plateau yield decreased. Occasionally, however, also an increase in plateau yield was observed with decreasing target thickness. Repeated scans of the same target typically

yielded plateau heights that could vary by about 5-10%, even with little charge deposited on the target in between runs. Possible explanations for this could be based on slight movement of the beamspot (revealing inhomogeneities of the target composition as a function of position on target, and leading to changes in detection efficiency as discussed previously), or relatively fast changes in target composition induced by the beam.

Figures 4.1 and 4.2 show the target profiles from 309 keV resonance scans for sodium tungstate and sodium silicate targets at different stages of proton bombardment.

The profile of Na_2WO_4 targets was very sensitive to the evaporation procedures. In particular, thicker targets were found to be more difficult to produce reliably with the described evaporation procedures and often found to have an irregular profile at the beginning of the bombardment. Often these profiles initially showed a lower yield in the front of the target, reaching a yield close to the value that was expected towards the end of the profile. Usually the targets became more regular during irradiation, as illustrated in Figure 4.3.

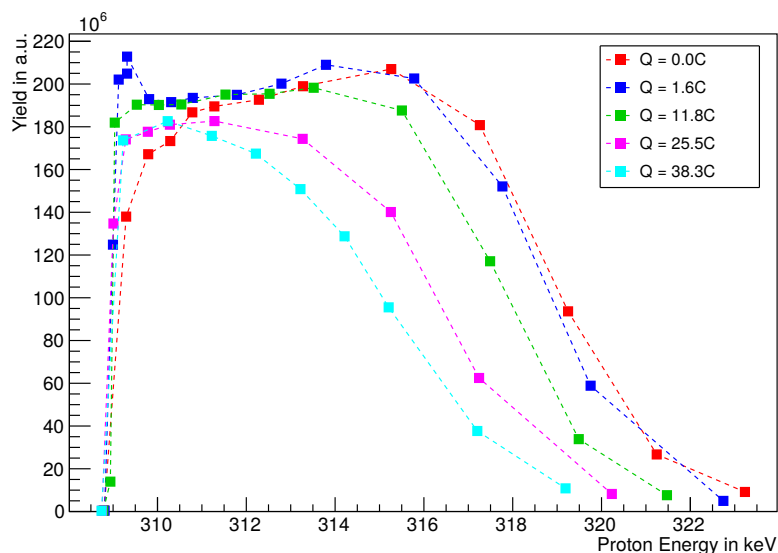


Figure 4.1: 309 keV resonance scans for a Na_2WO_4 target at different stages of the bombardment.

4.1.7 Target Analyses Ex Situ

Rutherford Backscattering

To evaluate the viability of the evaporation procedure and check that the stoichiometry is not affected in the process, Na_2WO_4 was evaporated onto a carbon backing. The resulting target was then studied by means of Rutherford Backscattering (RBS) of He^+

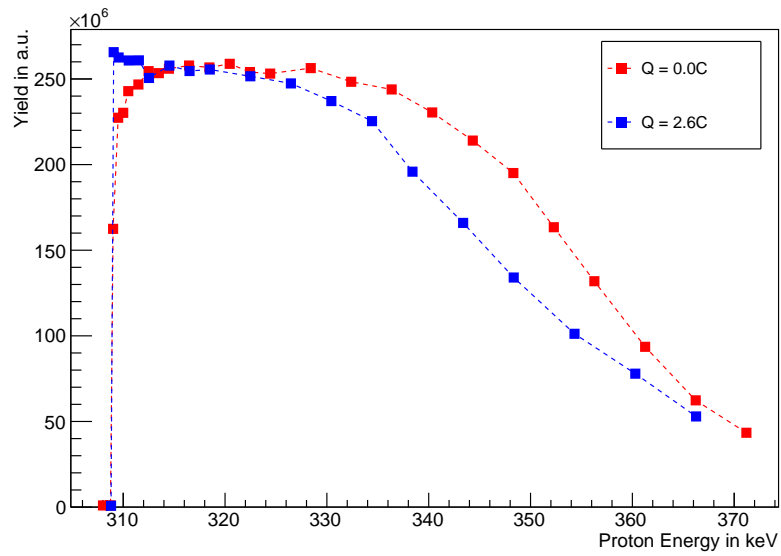


Figure 4.2: 309 keV resonance scans for a Na_2SiO_3 target at different stages of the bombardment.

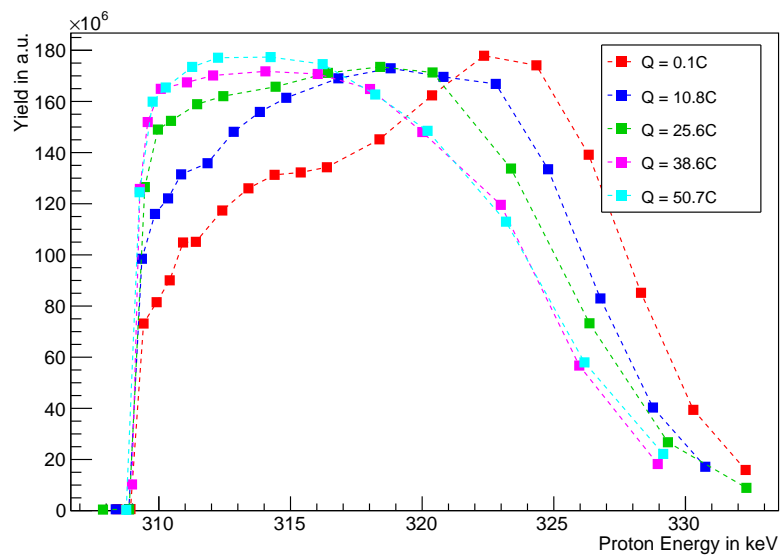


Figure 4.3: 309 keV resonance scans for a Na_2WO_4 target at different stages of the bombardment, showing an improvement in target profile in the course of the first phase of bombardment.

ions with an energy of 1.6 MeV. The measurements were performed at MTA Atomki [58], with a setup as described in [59]. The results taken with a detector located at an angle of 165° in Cornell geometry are shown in Figure 4.4. Also shown in this plot, for comparison are the results for a simple model of a layer of $\text{Na}_{2.00}\text{W}_{0.73}\text{O}_{3.93}$ on the carbon backing – a stoichiometry that is close to Na_2WO_4 . The simulated curve was determined using the program SIMNRA, version 6.06 [60]. Even if a more elaborate model (with different layers of sodium tungstate, or a transition region between sodium tungstate and tantalum) could likely provide a more faithful reproduction of the measured spectrum (e. g. at the low-energy end of the W region), this measurement supports the hypothesis that no drastic change of the Na_2WO_4 stoichiometry occurs during the evaporation (e. g. by dissociation of the salt).

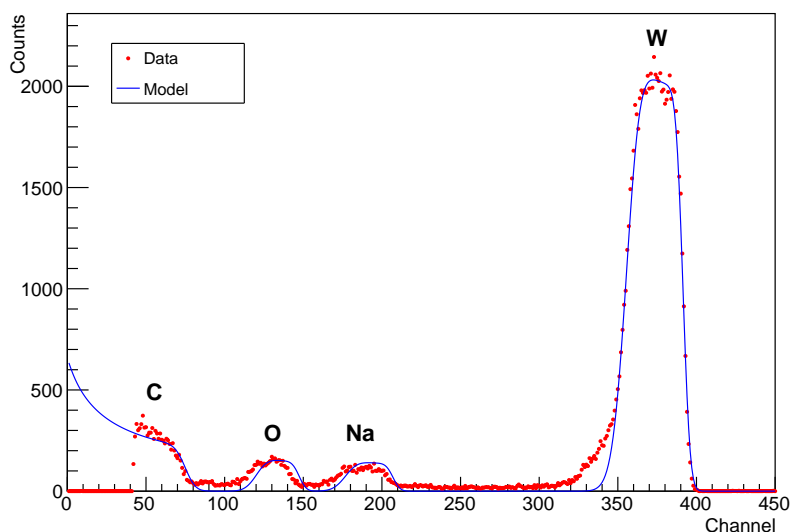


Figure 4.4: Spectrum obtained by Rutherford Backscattering for Na_2WO_4 evaporated onto carbon, compared to a model fit. The composition in the model is very close to the expected stoichiometry of the compound before evaporation.

An actual target from the measurements at LUNA could not be studied with this technique on the present setup, due to the large backscattering contribution of the tantalum backing. Furthermore, elements lighter than carbon are not detected, due to a low-energy cut-off.

Elastic Recoil Detection

The limitations of RBS can partially be overcome by the technique of Elastic Recoil Detection Analysis (ERDA). In this type of analysis, targets are bombarded with an ion beam, and recoil ions from the sample are detected. Sodium tungstate targets on

4 Data Acquisition and Analysis

tantalum backings, the same type as used in LUNA, were studied with this technique.

In a first analysis, two targets were studied with ERDA. Target Na_2WO_4 -#17 which had previously been bombarded with about 1.8 C of protons at LUNA, and Na_2WO_4 -#9 which had not been bombarded. The nominal area density of the targets determined during the evaporation was $170 \mu\text{g}/\text{cm}^2$ and $130 \mu\text{g}/\text{cm}^2$ respectively, corresponding to layer thicknesses of about 410 and $310 \mu\text{m}$ (assuming a mass density of $4.129 \text{g}/\text{cm}^3$ for the anhydrate), or column number densities of 350 and $270 \cdot 10^{15} \frac{\text{molecules}}{\text{cm}^2}$. Both targets were part of an early batch, which had not been permanently stored under vacuum. Multiple spots on the sample surfaces were analyzed: visually different spots of the irradiated target (expecting to cover irradiated and less irradiated parts), and two spots on the target that had not been bombarded with protons. The spots are shown qualitatively in Figure 4.5. The typical size of one of the analyzed spots is about $1.5 \times 1.5 \text{mm}^2$.



Figure 4.5: Targets Na_2WO_4 -#9 and -#17 which were analyzed with ERDA. The red squares qualitatively indicate the positions of the different analyzed spots (the actually analyzed spots may have been slightly displaced).

Measurements were performed and analyzed at the Ion Beam Center of the Helmholtz Center Dresden-Rossendorf (HZDR) [61]. The samples were bombarded with Cl^{7+} ions at an energy of 43 MeV. The angle of incidence of the beam was 70° with respect to the surface normal, and the scattering angle was 31° . Recoil ions were detected with a Bragg Ionization chamber. A visualization of the measured ΔE over E data is shown in Figure 4.6. A dedicated solid state detector at a scattering angle of 41° was used to detect hydrogen. This detector was fitted with an $18 \mu\text{m}$ Al foil to stop ions heavier than hydrogen. The acquired spectra were saved at fixed dose intervals, to monitor the total yield of the different elements and correct for target deterioration due to the ion beam bombardment.

The measurements on these targets were challenging due to several reasons. The high Z of the backing leads to strong Rutherford backscattering of the chlorine ions, so that the beam current had to be reduced in order to limit the dead times of the detector setup, which in turn reduces the statistics of the acquired data. The atomic numbers of tantalum in the backing and tungstate in the target layer differ only by a value of one, so that they are not clearly distinguishable in the analysis. Further complications arose from the surface structure of the samples, which visibly resembled a slightly brushed metal surface. Although attempted to consider in the analysis with a roughness model, this increases the uncertainty of the results.

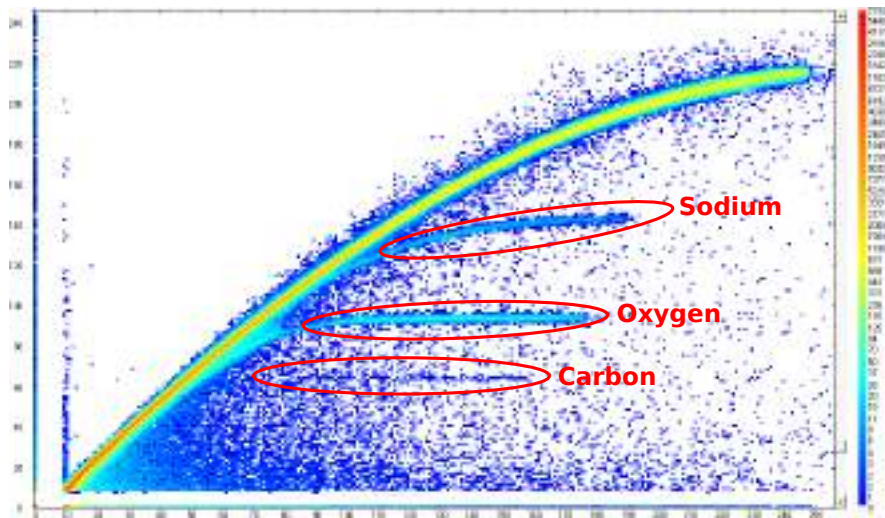


Figure 4.6: Acquired spectrum corresponding to ΔE over E as shown in the acquisition software MPANT [62], with the elements corresponding to the bands added.

The acquired data of recoiled ions (ERDA) and chlorine scattering (RBS) were analyzed simultaneously with the program NDF [63]. In parallel, also elemental depth profiles based on the raw data were provided.

The results [61] are shown in Table 4.3, which contains the fitted target compositions at the different spots, and the effective stopping powers derived for this composition. The spot A1 is a repeated measurement with a different target orientation to check for the influence of the surface roughness orientation. The last two columns show the values for average composition and stopping powers from all analyzed spots and the nominal composition for Na_2WO_4 . The average effective stopping power derived from the compositions of all spots is 15% larger than the effective stopping power for Na_2WO_4 . The effective stopping powers of the individual spots differ by up to 7% from the average values. The ratio of the effective stopping powers at 251 keV and 309 keV is much less sensitive to the variations in the results for the target compositions. For the different

points on the target, the ratio varies by less than 0.2% from the average value, and the average is 0.6% larger than the value for the nominal composition.

Table 4.3: Results of the ERDA on targets #9 and #17 [61]. Composition in atomic percentage. Stopping powers in 10^{-15} eV cm²/atom.

Composition from ERDA Analysis (Fit)								
	17-A	17-A1	17-B	17-C	9-A	9-B	Average	Na ₂ WO ₄
C	1.1	1.2	2.3	1.4	1.2	1.1	1.4	0.0
H	4.9	6.3	5.9	4.3	7.4	7.5	6.0	0.0
Na	24.0	23.4	23.6	22.5	20.6	20.6	22.5	28.6
O	59.2	58.4	57.8	62.7	60.8	60.6	59.9	57.1
W	10.8	10.7	10.5	9.1	10.0	10.2	10.2	14.3
$\epsilon_{\text{eff.}}$ for Na from Composition								
	17-A	17-A1	17-B	17-C	9-A	9-B	Average	Na ₂ WO ₄
$\epsilon(251 \text{ keV})$	61.4	62.2	61.7	63.8	69.0	69.1	64.5	56.3
$\epsilon(309 \text{ keV})$	55.9	56.6	56.1	58.0	62.7	62.9	58.7	51.5
$\frac{\epsilon(251 \text{ keV})}{\epsilon(309 \text{ keV})}$	1.098	1.099	1.100	1.100	1.100	1.099	1.099	1.093

Figure 4.7 shows an example for the depth profile obtained from ERDA, and gives an impression of the scatter of the data points owing to low statistics, and possibly also surface roughness effects.

After the first ERDA measurements, the target handling procedures were improved (e. g. consequently keeping the targets under vacuum for storage and transportation) and some changes were made to the parameters of the production process, as it was found to yield thinner targets with more regular resonance scans and fewer targets with irregular target profiles. Such targets, with nominal thicknesses of about $35 \mu\text{g}/\text{cm}^2$ (corresponding to an energy loss of about 7 keV at 300 keV proton energy), were used for the majority of the measurements in the later stages of the experimental campaign.

The ERDA measurements were repeated on two Na₂WO₄ targets, shown in Figure 4.8, produced and handled with these procedures: Target Na₂WO₄-#44 had been bombarded with 17.1 C of protons, Na₂WO₄-#45 had not been bombarded prior to the ERDA. The two targets were produced on the same day. Their nominal thicknesses determined during the evaporation were $35 \mu\text{g}/\text{cm}^2$ and $30 \mu\text{g}/\text{cm}^2$ respectively. The targets and the selected spots for the analysis are shown in Figure 4.8. Target #44 shows a distinct beam spot, with points A and C placed in and at the edge of the beam spot. Target #45 is mostly regular, with some discolorations of unknown origin. Point A was chosen for analysis of the homogeneous target area. Point B was placed on a discolored patch on the target surface.

The analysis of the thin target layers was more challenging than that of the thicker

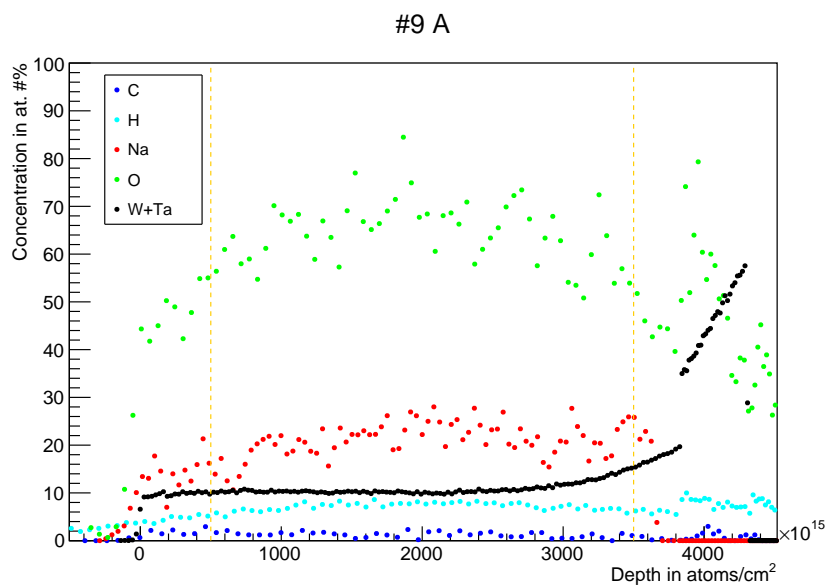


Figure 4.7: Example depth profile obtained with ERDA [61]. The vertical lines approximately mark the region that is assumed to be the homogeneous target layer.

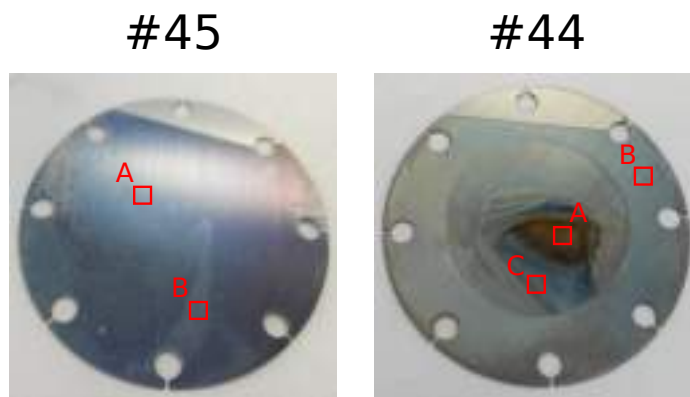


Figure 4.8: Targets Na_2WO_4 -#44 and -#45 which were analyzed with ERDA. The red squares qualitatively indicate the positions of the different analyzed spots (the actually analyzed spots may have been slightly displaced).

target analyzed previously. For these targets, the thickness of the active layer was on the order of the ERDA depth resolution, which is affected by the surface roughness of the samples. With the thinner layers target degradation from the chlorine bombardment during the ERDA measurements was much more influential, so that each analyzed spot on the target was analyzed in multiple shorter measurements, moving the beamspot slightly each time, to limit the detrimental influence of local target degradation.

Table 4.4: Results ERDA measurements on targets #44 and #45 [64]. Composition in atomic percentage. Stopping powers in 10^{-15} eV cm²/atom.

Composition from ERDA Analysis (Fit)						
	44-A	44-B	44-B3	44-C	45-A	45-B
C	4.0	3.5	8.4	4.2	–	–
H	5.7	21.3	15.5	4.2	20.0	21.3
Na	11.6	14.2	11.0	17.3	18.5	14.4
O	48.0	46.9	55.3	64.6	51.2	53.6
W	18.4	14.0	9.9	9.7	10.2	10.7
$\epsilon_{\text{eff.}}$ for Na from Composition						
	44-A	44-B	44-B3	44-C	45-A	45-B
$\epsilon(251 \text{ keV})$	123.1	95.2	118.2	82.4	70.5	89.5
$\epsilon(309 \text{ keV})$	113.1	86.9	107.4	74.9	64.1	81.5
$\epsilon(251 \text{ keV})/\epsilon(309 \text{ keV})$	1.088	1.096	1.101	1.100	1.100	1.098

The results are summarized in Table 4.4, where 44-B3 names a repeated measurement of point 44. In the case of target Na₂WO₄-#44, a significant depletion of sodium is observed in the beam spot (A), but also the two other analyzed spots. Whilst the target degradation in the beamspot is not unexpected, given the large accumulated charge of proton bombardment for this target, the process that could lead to a reduced sodium content in spot B, close to the edge of the target, is unknown. Target #45 shows an increased content of sodium, slightly lower than those found in 4.3 and than expected for the nominal composition. The discolored spot B shows a slightly reduced content of sodium in comparison.

Due to the target degradation, the results obtained for target #44 will not correspond to the target composition at the beginning of the proton bombardment, when the 251 keV and 309 keV resonance measurements were performed. Therefore the results of the analysis for #45-A were used as the reference composition for the analysis of the measurements of target #44. The effective stopping power for Na, given the composition as determined from the ERDA, are shown in the Table for the two ²³Na(p, γ) resonance energies. An uncertainty of 2 atom. % was assumed for each component of

the determined composition. The uncertainty of the effective stopping power was then determined by randomly sampling compositions according to these uncertainties (assuming normal distributions with 2 atom. % standard deviation) and calculating the effective stopping power. The average effective stopping powers and their variance were determined:

$$\begin{aligned}\varepsilon_{\text{eff.}}(251 \text{ keV}) &= (71.2 \pm 7.4) \text{ eV}/10^{15} \text{ atoms}\cdot\text{cm}^2 \\ \varepsilon_{\text{eff.}}(309 \text{ keV}) &= (64.7 \pm 6.8) \text{ eV}/10^{15} \text{ atoms}\cdot\text{cm}^2 \\ \varepsilon_{\text{eff.}}(309 \text{ keV})/\varepsilon_{\text{eff.}}(251 \text{ keV}) &= 0.9094 \pm 0.0019\end{aligned}$$

These values were assumed as the reference composition for target #44, after adding 10% (in quadrature) to the uncertainty, which is to account for the uncertainty from inferring the composition of target #44 based on #45. This error is estimated on the basis of the observed variation in yields in the 309 keV resonance scans between different targets. This results in a relative uncertainty of the effective stopping powers of 14.5% at both resonance energies. The relative uncertainty of the ratio of the stopping powers is much smaller, and amounts only to about 0.2%.

4.1.8 Yield Estimates

With the target properties as described above, the expected reaction yields for $^{23}\text{Na}(p, \gamma)^{24}\text{Mg}$ can be estimated for the different measurement scenarios. For the narrow resonances at 251 keV and 309 keV, the yield is calculated by equation (1.11). For the non-resonant contribution, the yield is calculated from (1.10) using the cross section given by the S -factor of [14].

Table 4.5 lists the yields for the nominal composition of Na_2WO_4 . Considering the ERDA results, the experiment yield is expected to be slightly lower.

Table 4.5: Yield estimates for a Na_2WO_4 target assuming an effective stopping power corresponding to the nominal composition.

Contribution	Yield in Reactions / C
309 keV Resonance	$1.92 \cdot 10^8$
251 keV Resonance	$1.08 \cdot 10^6$
144 keV Resonance	upper limit
	hint
Direct Capture	$E_p = 400 \text{ keV}, \Delta E = 300 \text{ keV}$
	$E_p = 400 \text{ keV}, \Delta E = 20 \text{ keV}$
	$E_p = 400 \text{ keV}, \Delta E = 10 \text{ keV}$

4.1.9 Beam-induced Backgrounds

Another important consideration for the target selection are beam-induced backgrounds. These backgrounds are caused by spurious reactions in the target material on nuclides different than the target nucleus. These spurious reactions can occur on nuclides that are a regular part of the target material (such as ^{18}O in Na_2WO_4), or on chemical contaminants.

As for the contaminants, light elements are a particular concern, because of their lower Coulomb barrier. Resonances in the cross sections of the spurious reactions can make a particular background contribution only relevant in a limited energy range. Nuclides with large Q -values for (p, γ) reactions (comparable or larger than the studied reaction) are particularly critical for a summing detector.

Apart from the expected background from $^{18}\text{O}(p, \gamma)$ in targets that contain oxygen (with a natural abundance of ^{18}O of 0.205%), few other backgrounds have been observed in the course of the described experiments.

The presence of small amounts of carbon has been established in the ERDA measurements, and $^{12}\text{C}(p, \gamma)$ ($Q = 1943.49(27)$ keV) has been observed in the HPGe spectra. Due to its low Q value and a purely non-resonant cross section in the proton energy range of this experiment, the background from this reaction was uncritical.

The reaction $^{19}\text{F}(p, \alpha\gamma)$ ($Q = 8113.61$ keV) has a resonance at a proton energy of 340.5 keV, which leads to the emission of three distinct gamma rays at 6.13, 6.92 and 7.12 MeV [65]. For measurements above (in particular, close to) this resonance energy, the background from this reaction can be critical. In HPGe measurements, the reaction increases the continuous background in the energy region below 7.12 MeV. In the BGO summing detector, the random coincidence of two gamma rays from $^{19}\text{F}(p, \alpha\gamma)$ can sum up to an energy that is very close to the $^{23}\text{Na}(p, \gamma)$ sum energy peak, given the BGO detector resolution. To avoid additional fluorine contaminations during the preparation of the targets, the backings for targets dedicated to measurements at higher energies were etched without the use of hydrofluoric acid.

Another contaminant which has occasionally been observed in the course of target development was $^7\text{Li}(p, \gamma)$. With a Q -value of 17254.4(4) keV and a broad excited state at 3.04 MeV in ^8Be , this reaction can contribute significantly to the region of interest for the measurement of $^{23}\text{Na}(p, \gamma)$. Figure 4.9 shows the sum energy spectrum acquired at $E_p = 145.0$ keV, showing a significant background contribution from a ^7Li contamination.

An ubiquitous source of beam induced background was boron, via the proton capture reaction $^{11}\text{B}(p, \gamma)$. The reaction has a Q value of 15956.85(42) keV and a resonance at $E_p = 162$ keV, which has a width of 5.2 keV (center of mass energy) [66]. With this broad resonance close to the investigated 144 keV resonance in $^{23}\text{Na}(p, \gamma)$, ^{11}B turned out to be the most critical source of beam-induced background for the 144 keV resonance

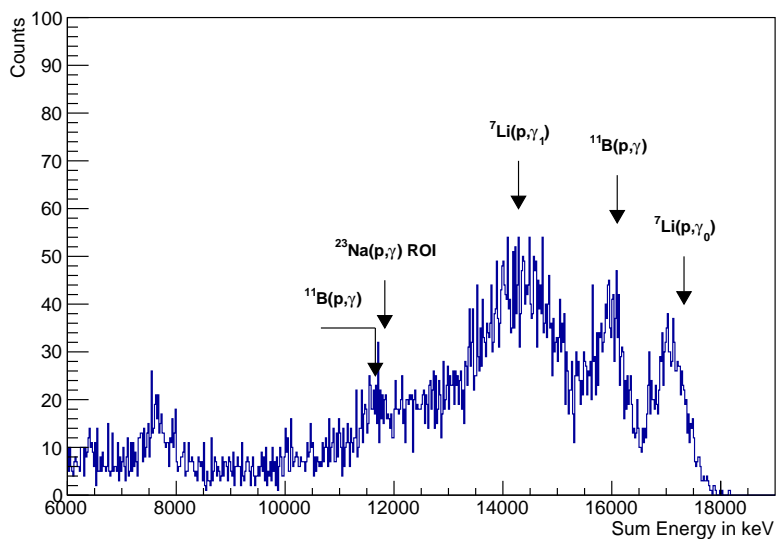


Figure 4.9: BGO sum energy spectrum for a proton energy of 145.0 keV with a target showing a significant beam-induced background from ${}^7\text{Li}$ plus background from ${}^{11}\text{B}(p, \gamma)$.

search with the BGO detector. Not only is the Q value of the reaction larger than that of ${}^{23}\text{Na}(p, \gamma)$, but also the radiative deexcitation of the compound nucleus ${}^{12}\text{C}$ proceeds mostly via the first excited state, i. e. in a cascade of two gamma rays with energies of 11.67 MeV and 4.44 MeV. If only the first gamma ray is detected (and the second gamma ray escapes), the signal at 11.67 MeV is very close to the expected signal from the 144 keV ${}^{23}\text{Na}(p, \gamma)$ resonance with $E_x = 11830.7$ keV, given the energy resolution of the BGO detector. Figure 4.10 shows a spectrum acquired during the bombardment of a blank backing with protons of an energy of 160.0 keV. The large boron peak at 16.11 MeV and the smaller peak at 11.67 MeV can be clearly seen. The ${}^{23}\text{Na}(p, \gamma)$ region of interest is indicated, even though the backing had no active sodium target layer.

Clear lithium backgrounds were only observed in few targets during the early phases of target development. In the course of this development, targets were produced from raw Na_2WO_4 (or typically a hydrated form of it) supplied by different manufacturers, and a material showing no visible beam-induced background from ${}^7\text{Li}$ was chosen.

To estimate the order of magnitude of the boron contamination needed to induce a signal that will be of concern for the 144 keV resonance search, Figure 4.11 shows the expected reaction yield as a function of proton energy for an infinitely thick target of tantalum with a 1 ppm contamination of natural boron (80.1% ${}^{11}\text{B}$). It is visible that a boron contamination on the level of ppm can cause a ${}^{11}\text{B}(p, \gamma)$ reaction rate that is

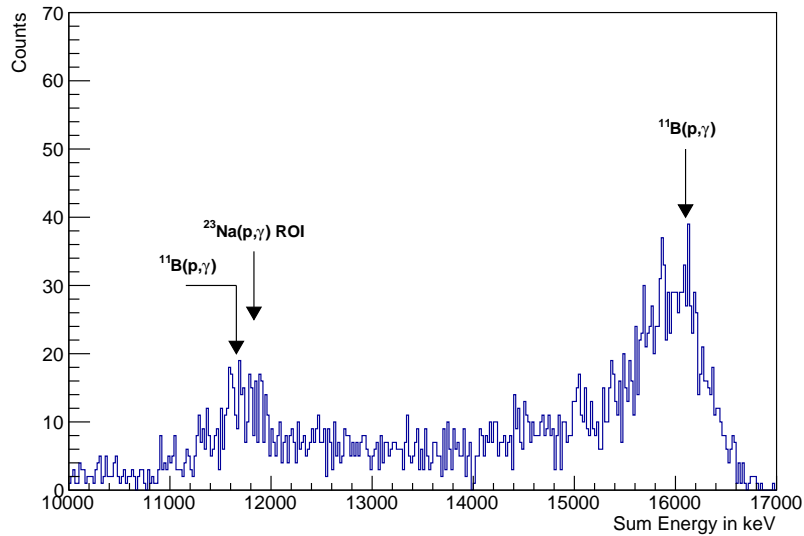


Figure 4.10: BGO sum energy spectrum for a proton energy of 160.0 keV with a blank backing (no sodium target layer), showing a significant beam-induced background from $^{11}\text{B}(p, \gamma)$.

comparable to the expected rate from the 144 keV resonance in $^{23}\text{Na}(p, \gamma)$.

As in the case of ^7Li , raw materials from different suppliers were used to produce targets, and the contribution of ^{11}B was measured, bombarding with proton energies slightly below the 162 keV resonance. The boron signal rate was found to vary over a wide range for the different targets. Whilst some of the tested targets showed an increased boron rate, many had boron rates close to a lower threshold at a value similar to that observed with a blank backing. One possible explanation for this is the presence of boron in the backing material, another one would be boron contaminations in beam line parts that are hit by stray beam. Owing to the large cross section for $^{11}\text{B}(p, \gamma)$, also minuscule amounts of stray beam hitting other parts than the active target surface could yield an appreciable rate of boron reactions. Assuming that the active target layer has a lower background content than the backing material, thick targets would yield a lower boron background rate. This was not observed systematically. The studies were difficult, however, as the level of the boron background rates was low, so that measurements to characterize the level of beam-induced background required an appreciable accumulated charge on surface. As shorter measurements had too few counts to distinguish the spectral shape, the number of counts per accumulated charge in the energy region above 14 MeV was considered as an indicator for the beam-induced backgrounds.

As an additional complication, the background rate in this energy region was not only a function of target and beam energy, but appeared also to depend on the parameters

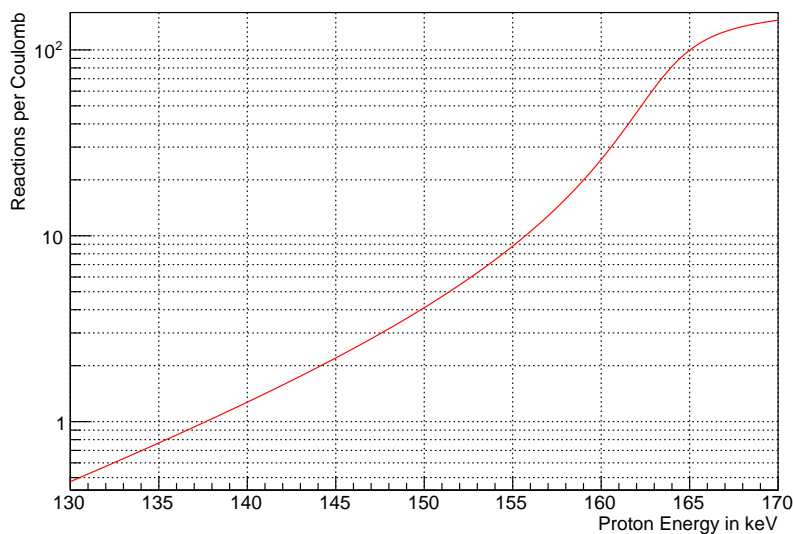


Figure 4.11: Yield in $^{11}\text{B}(p, \gamma)$ derived for an infinitely thick tantalum target with a content of 1 ppm of (natural) Boron. S -factor from [67].

of beam tuning. This would support the hypothesis of backgrounds induced by stray beam. However, no clear correlation was observed between the current on the secondary electron suppression pipe and the high energy background rate. Chemically cleaning the copper pipe, or plating it with nickel did not change the background rate significantly (within the usual variations).

The shape of the boron signal in the sum spectrum depends on the position of the origin of the reactions. In off-center positions, the summing probability can be decreased, which decreases the 16.11 MeV sum peak, enhancing the 11.67 MeV single gamma peak. A comparison of the spectral shape of the boron signal with simulated spectra for $^{11}\text{B}(p, \gamma)$ at different positions along the beam axis, shown in Figure 4.12, suggest an origin of the boron not too far upstream, although a precise determination remains difficult for a typical background run, as it has much lower numbers of counts (the example shown here was measured at 160.0 keV and corresponds to an accumulated charge of 2.5 C).

In conclusion, a systematic investigation would be required to determine the precise origin of the boron background contribution and reduce this background. Such a study needed to systematically investigate beam line parts, the active target material and target backings.

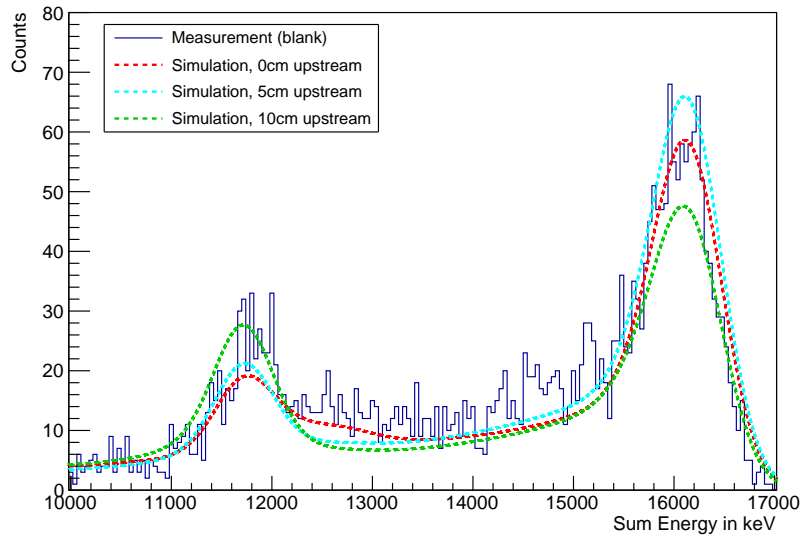


Figure 4.12: Comparison of the measured beam-induced background for a blank backing with simulated spectra for $^{11}\text{B}(p, \gamma)$ at different distances on the beam axis, upstream of the target.

4.2 HPGe Phase Analysis

4.2.1 Measurements Overview

About 250 C of integrated charge on target were spent on $^{23}\text{Na}(p, \gamma)$ measurements in the HPGe detector phase. The measurements focused on scans and measurements of the 309 keV and 251 keV resonances. Other data points were acquired mostly at energies above the 309 keV resonance. Few measurements were taken for the maximum proton energy achievable at LUNA, searching for the direct capture component.

4.2.2 251 keV Resonance

The 251 keV resonance was scanned multiple times with different targets. Three spectra (on three different targets) were acquired with appreciable accumulated charges during the measurements: Runs A and B were acquired at a proton energy of 253.0 keV (accumulated charges 2.7 and 2.9 C), run C was acquired at $E_p = 255.0$ keV (11.5 C accumulated).

The spectrum of the longest run C was analyzed, searching for possible primary transitions from the resonance state at $E_x = 11931.2$ keV. Ten possible primary transitions could be identified. The numbers of counts for the gamma lines corresponding to the ten transitions were determined for the three spectra of runs A, B and C. To derive

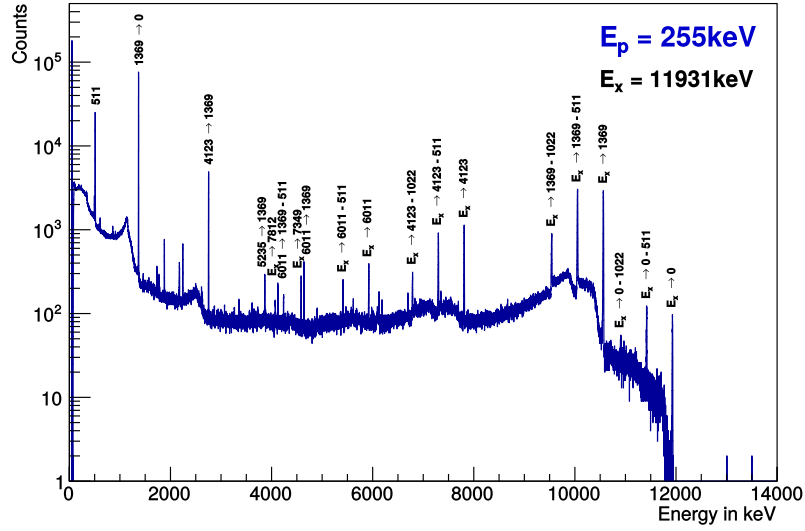


Figure 4.13: HPGe spectrum acquired on the 251 keV resonance, with the main identified transitions indicated. Not all observed (possible) primary transitions are visible at this scale (and indicated in this plot).

the branching ratios, summing effects are again important to consider carefully. As the branching ratios for the levels reached by the suspected primary transitions were known, the cascades following from each primary transition could be derived. Using full energy peak and total efficiencies from the empirical efficiency calibration, the probabilities for each suspected primary transition to contribute to the full energy peak efficiency corresponding to its own energy or to other primary transitions with larger energies (via summing in) could be determined. These probabilities can be written in matrix form. Be P_{ij} the probability that the primary transition with index j contributes to the full energy peak of primary transition i , B_i the branching ratio of the primary transition i , N_i the number of counts in the full energy peak corresponding to the primary transition i and $N_{\text{reactions}}$ the total number of reactions, the following equations hold in the case of n primary transitions:

$$N_{\text{reactions}} \cdot \begin{pmatrix} P_{11} & \dots & P_{1n} \\ \vdots & \ddots & \vdots \\ P_{n1} & \dots & P_{nn} \end{pmatrix} \cdot \begin{pmatrix} B_1 \\ \vdots \\ B_n \end{pmatrix} = \begin{pmatrix} N_1 \\ \vdots \\ N_n \end{pmatrix} \quad (4.1)$$

$$\sum_i B_i = 100\% \quad (4.2)$$

For n (potential) primary transitions this is a set of $n + 1$ equations that can be

solved to determine the unknown B_i and $N_{\text{reactions}}$. A Monte Carlo approach was used to determine the statistical uncertainty of the branching ratios determined in this way. The observed N_i were sampled from normal distributions according to the N_i and their uncertainties determined from the spectrum analysis. Determining the B_i and $N_{\text{reactions}}$ for these samples N_i and repeating this process, a distribution for B_i and $B_{\text{reactions}}$ is obtained. The mean and RMS values of these distributions were taken as value and (statistical) uncertainty of the branching ratios. The results for the three runs are shown in Table 4.6. For the ground state transition, a slightly negative mean value of the branching ratio is found, which is an indication that this peak is dominated by summing in, and summing in is slightly overestimated in this case by the efficiency model. Also the branching ratios for the transitions to the states at 9299.77 keV and 4238.24 keV are compatible with 0 at the two sigma level. The branching ratio for the transition to the the 8864.29 keV level is low and has a rather large statistical uncertainty. This transition, however, cannot be the result of summing in (as no primary transition to a higher level was observed). Therefore its existence was accepted.

The adopted values are the weighted average of the branching ratios determined from the three runs, renormalized after canceling the three transitions discussed above, and with a 10% systematic uncertainty added to account for uncertainties of the efficiency calibration.

Table 4.6: Derived branching ratios (in percent) for possible primary transitions from $E_x = 11931$ keV with their statistical uncertainties for three data sets, and branching ratios adopted for this work (calculated as the weighted average) including systematic uncertainty. (The adopted branching ratios sum up to 100.1% as an effect of rounding.)

$E_x \rightarrow$	Run A	Run B	Run C	Adopted
9299.77	0.50 ± 0.15	0.16 ± 0.12	0.07 ± 0.06	—
8864.29	0.23 ± 0.13	0.25 ± 0.11	0.27 ± 0.06	0.3 ± 0.1
7812.35	1.25 ± 0.16	1.21 ± 0.17	1.00 ± 0.08	1.1 ± 0.2
7349	1.10 ± 0.21	1.42 ± 0.17	1.19 ± 0.10	1.2 ± 0.2
6010.84	3.53 ± 0.33	3.68 ± 0.28	3.07 ± 0.15	3.3 ± 0.5
5235.12	1.66 ± 0.38	0.98 ± 0.32	0.83 ± 0.17	1.0 ± 0.2
4238.24	0.74 ± 0.37	0.36 ± 0.28	0.31 ± 0.17	—
4122.889	17.71 ± 0.55	17.91 ± 0.47	18.73 ± 0.25	18.5 ± 2.1
1368.672	73.88 ± 0.79	74.35 ± 0.67	74.31 ± 0.35	74.7 ± 7.8
0	-0.61 ± 0.30	-0.32 ± 0.24	-0.28 ± 0.09	—

For an absolute determination of the resonance strength, the target stoichiometry needs to be well-known. The analysis thus focused on target #44 which, together with

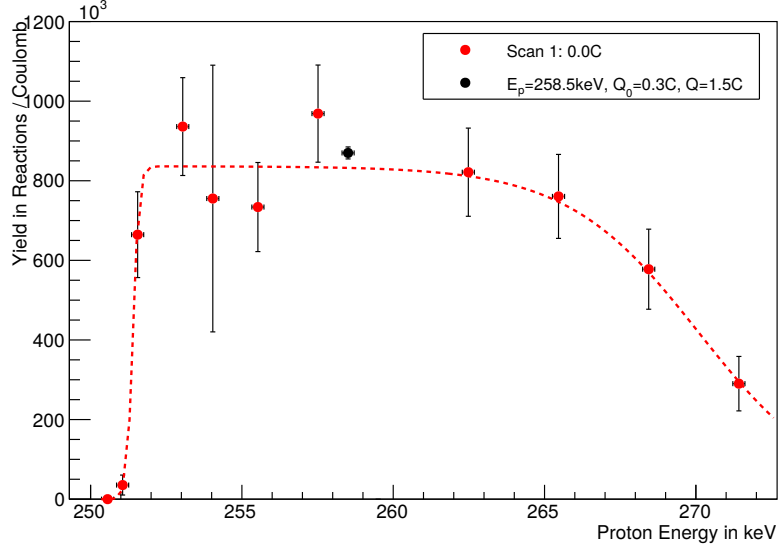


Figure 4.14: 251 keV resonance scan of target #44, with yield derived from transition $E_x \rightarrow 1368.672$ keV, and longer run on the plateau.

its sister target #45, was analyzed by ERDA as described in the previous section.

A resonance scan of the 251 keV resonance on this target is shown in Figure 4.14. As an empirical fit function, the difference of two sigmoid functions (one for the rising, one for the falling edge) was fitted to the resonance profile:

$$Y(E) = Y_{\text{plateau}} \cdot \left(\frac{1}{1 + \exp((E_{\text{res.}} - E)/w_1)} - \frac{1}{1 + \exp((E_{\text{res.}} + \Delta E - E)/w_2)} \right) \quad (4.3)$$

In this parametrization, Y_{plateau} is the height of the plateau, $E_{\text{res.}}$ the half-height point of the rising edge and ΔE a measure of the length of the plateau. The parameters w_1 and w_2 determine the width of the rising and falling edges.

The height of the plateau obtained in the fit is $8.4(6) \cdot 10^5$ reactions/C, compatible with the $8.70(15) \cdot 10^5$ reactions/C (statistical uncertainty only) obtained from a single longer run on top of the resonance profile.

Using the yield from the data point of the long run, with the effective stopping power determined from the analysis of target #45 as described in the previous section, this yields a resonance strength of $\omega\gamma = 535(96) \mu\text{eV}$, compared to the literature value of $525(175) \mu\text{eV}$. The uncertainty budget includes 14.5% from the stopping power composition, 10% for the efficiency / branching ratio determination of the gamma line used for the yield calculation, 3% for the target current determination, 2% statistical uncertainty for the peak area in the long run. Added in quadrature this yields a reduction in relative

uncertainty of almost a factor of two, from 33% to 18%.

4.2.3 309 keV Resonance

Immediately before the 251 keV resonance scan that was presented in the previous subsection, a 309 keV resonance scan had been performed on the same target. A similar analysis can be used to determine the 309 keV resonance strength from this target scan, only that in this case the gamma ray branching ratios are known so that the reaction yield can be obtained directly from the yield of a primary gamma ray. Summing effects were considered as described in the section of detector calibration.

The resonance scan for the yield, derived from the $E_x \rightarrow 1368.672$ keV gamma line, is shown in Figure 4.15. The plateau height obtained in the fit is $1.64(3) \cdot 10^8$ reactions/C. This results in a resonance strength of 113(20) meV, in excellent agreement with the literature value of 105(19) meV. The uncertainty budget is identical to the 251 keV resonance, except for a slightly lower uncertainty of the resonance yield. The relative uncertainty of the result obtained in this work and the result in literature are both 18%.

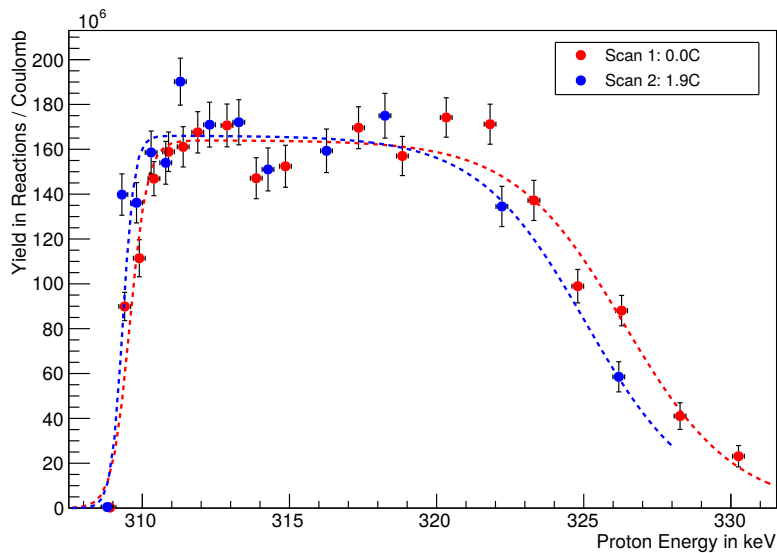


Figure 4.15: 309 keV resonance scans of target #44. Scan 1 was used for the resonance strength determination, but the fitted plateau height of both runs are very similar.

4.2.4 Relative Resonance Strength Determination

The major source of uncertainty for the absolute resonance strength determinations in this work is the effective stopping power from the uncertainty of the target composi-

tion. This systematic uncertainty strongly affects the determination of both resonance strengths that were presented here.

Calculating the ratio of two resonance strengths, the systematic uncertainty of the target composition does translate to a much lower uncertainty of this ratio than it does to the uncertainty of the individual values. The reason for this is the qualitatively similar energy dependence of the stopping power for the elements that have similar atomic mass numbers (see also the description in the next section).

With the same sampling method as that used to determine the distributions of $\varepsilon_{\text{eff.}}(251 \text{ keV})$ and $\varepsilon_{\text{eff.}}(309 \text{ keV})$, a distribution for the ratio $\varepsilon_{\text{eff.}}(309 \text{ keV})/\varepsilon_{\text{eff.}}(251 \text{ keV})$ can be determined. The variation (RMS) of this ratio obtained with the sampling algorithm is only about 0.2%, whereas the individual effective stopping powers vary by as much as 10%.

As both resonance strengths in this work were determined with a comparable or better uncertainty than the presently available literature values, the more precise knowledge of their ratio is of limited use. If a future experiment, however, would yield a more precise determination of the stronger resonance at $\omega\gamma(309 \text{ keV})$, a more precise value of $\omega\gamma(251 \text{ keV})$ could be determined using the ratio of the resonance strength values presented in this work.

4.2.5 Non-resonant Component

The detection of a non-resonant component is challenging, not primarily because the number of expected reactions is low per se (cf. subsection 4.1.8), but because of the contributions from resonant reactions. The resonances with $E_{\text{res.}} < 400 \text{ keV}$ are expected to be rather narrow, but owing to the slowly fading sodium content with target depth (cf. the “tails” of the 309 keV resonance scans), gamma ray peaks associated with resonances at energies significantly below the beam energy are observed, even in the case of thin targets. Although the primary gamma rays of these resonant reactions (occurring at a depth in which the protons are slowed down to the resonance energy $E_{\text{res.}}$) are lower in energy than the gamma ray energy of the direct capture to the ground state of ^{24}Mg , they can overlap with the region of interest due to the energy resolution of the detector (for $E_{\text{res.}}$ not far below the proton beam energy), and can pose a background in particular for the direct capture transitions to excited states in ^{24}Mg .

Even though a thin target would be preferable to reduce the contribution of resonances at lower energies, the target thickness should not be too small in order to achieve an appreciable non-resonant signal. Thicker targets, however, often exhibited irregularities in profile shape as discussed in section 4.1, which often evened out after initial bombardment. In this first phase of the bombardment the profile shape may change considerably, which introduces significant uncertainties in the evaluation of any spectra

acquired during this phase.

Considering the energy dependence of the direct capture cross section, the chances for detection of the resonance increase with proton energy. Considering the (p, γ) resonances for ^{23}Na , the most promising approach at LUNA400 appears to be at the maximum LUNA energy to increase the direct capture yield and stay as far above the narrow resonance at 372 keV proton energy.

In this work, measurements with a thick target (initial thickness of about 40 keV energy loss at 309 keV) are analyzed. The development of the target profile as seen in the 309 keV resonance scans is shown in Figure 4.16. The initial profile does not show a single flat plateau, but rather a reduced yield in the front, and an increased yield in the back of the target. The second and third scans of the target show a much more regular profile. The fourth scan starts to show an increased plateau yield. The thickness of the target decreases steadily with bombardment.

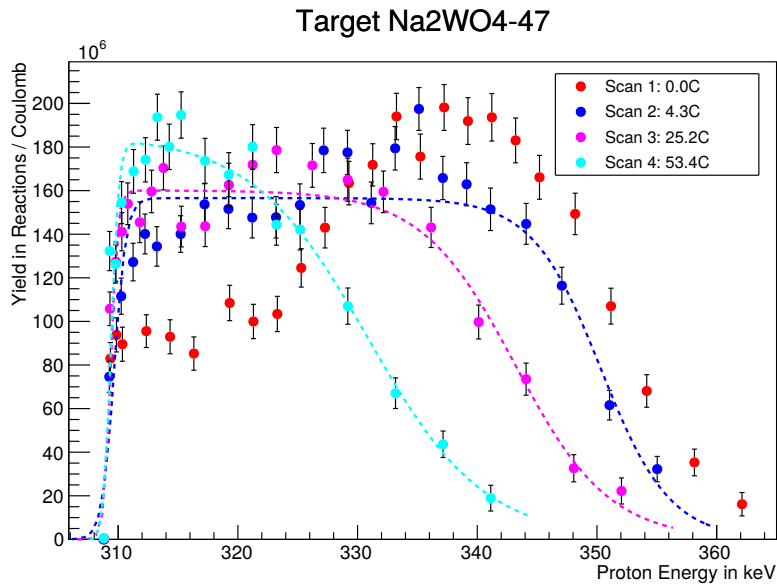


Figure 4.16: Resonance scans of the $E_p = 309$ keV resonance in $^{23}\text{Na}(p, \gamma)$ for a thick target used in the search for a non-resonant cross section contribution.

Two long runs at high proton energies were performed in between Scans 2, 3 and 4. The first run was performed at a proton energy of $E_p = 396.0$ keV, with an accumulated charge of 20.86 C. In the second run, 28.17 C were accumulated on target, at a proton energy of $E_p = 399.6$ keV.

The number and energy distribution of gamma rays emitted in the direct capture

process depends on the target composition (via the stopping power):

$$Y = \int_0^{E_0} \frac{\sigma^{\text{DC}}(E)}{\varepsilon_{\text{eff.}}(E)} dE \quad (4.4)$$

where the effective stopping power at the energy E is a function of depth in the target, and the depth (traversed area density of effective nuclei) is given by:

$$d(E) = \int_{E_0}^E -\frac{1}{\varepsilon_{\text{eff.}}}(E) dE \quad (4.5)$$

The information on the composition is only indirectly accessible in situ, via the yield observed in the ^{23}Na resonance scans that provides information of the effective stopping power at the resonance energy in a depth that corresponds to an energy loss of the initial proton energy minus the resonance energy.

The following procedure was adopted to approximately derive the expected direct capture yield from the 309 keV resonance scans: assuming the nominal composition of Na_2WO_4 , the relation $d(E)$ between depth and proton energy was calculated for protons of the initial energy E_p of the measurement. The assumption of the nominal composition is not far from reality in the front of the target, but begins to be inaccurate in the region of the tail of the resonance profile. However, as the direct capture cross section has its largest values at higher proton energies, the front of the target gives the most relevant contribution to the reaction yield, so that the approximation appears justified. In this measurement, another argument is that a peak from the 372 keV resonance covers the contribution of the direct capture signal at lower energies (from reactions towards the back of the target), so that the measurement is primarily sensitive to the DC yield in the front of the target where the approximation works best.

Again considering the nominal composition, the initial proton energy E'_p is calculated that is needed to arrive at the resonance energy $E_{\text{res.}}$ at the same depth as E_p was slowed down to E . The yield at the energy E'_p of the 309 keV resonance scan yields information on the effective stopping power at $E_{\text{res.}}$ at this depth in the target. Still assuming the nominal target composition, this stopping power at $E_{\text{res.}}$ can be related to the stopping power at the energy E . Obviously the approximation of the nominal composition is violated in the parts of the resonance scan where the effective stopping power is larger (i. e. the yield is lower) than determined from the nominal composition. Thanks to a similar energy dependence of the stopping powers of the elements (see Figure 4.17), the ratio $\varepsilon_{\text{eff.}}(E_{\text{res.}})/\varepsilon_{\text{eff.}}(E)$ is fairly robust against limited variations in the stoichiometry. Again it is to our advantage that the target composition in the front of the target does not differ greatly from the nominal composition. With this procedure,

$\varepsilon_{\text{eff.}}(E)$ is obtained for a given initial proton energy E_p and can be used to calculate the expected DC yield with equation (4.4). For the DC S factor, again the values from [14] are adopted.

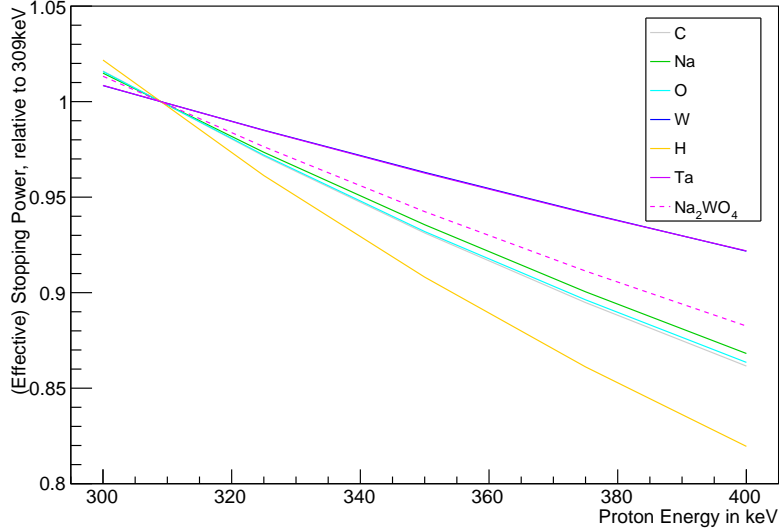


Figure 4.17: (Effective) stopping power of various elements and Na in Na_2WO_4 , relative to the value at 309 keV. The lightest (H) and most heavy elements (Ta and W) diverge by approximately $\pm 5\%$ from the lighter elements and the Na_2WO_4 compound. Stopping power data from [5].

The differential yield dY/dE determines the shape of the gamma ray spectrum emitted in the DC process for the given target. Applying the energy resolution of the detector, a template signal is obtained, whose contribution can be fitted to the experimental spectra. For the direct capture to the ground state, a peak at 12049 keV is visible in the spectrum. This peak corresponds to the excitation energy from the 372 keV resonance in $^{23}\text{Na}(p, \gamma)$. The fit model thus included a gaussian peak at 12049 keV, a flat background and the DC component determined as described above. The background level, the areas of the gaussian and the DC signals and the detector resolution were set as free fit parameters.

Due to the heavy bombardment of the target, the target profiles changed visibly in the course of the measurements. Because of this, the fit to determine the DC component in the spectrum was performed twice for each measurement: once using the resonance profile before the measurement, and once after.

The fit results are shown in Figure 4.18, and the expected and obtained numbers of counts are summarized in Table 4.7. Direct capture to the ground state has been observed in both runs. Compared to the calculated number of direct capture events, the

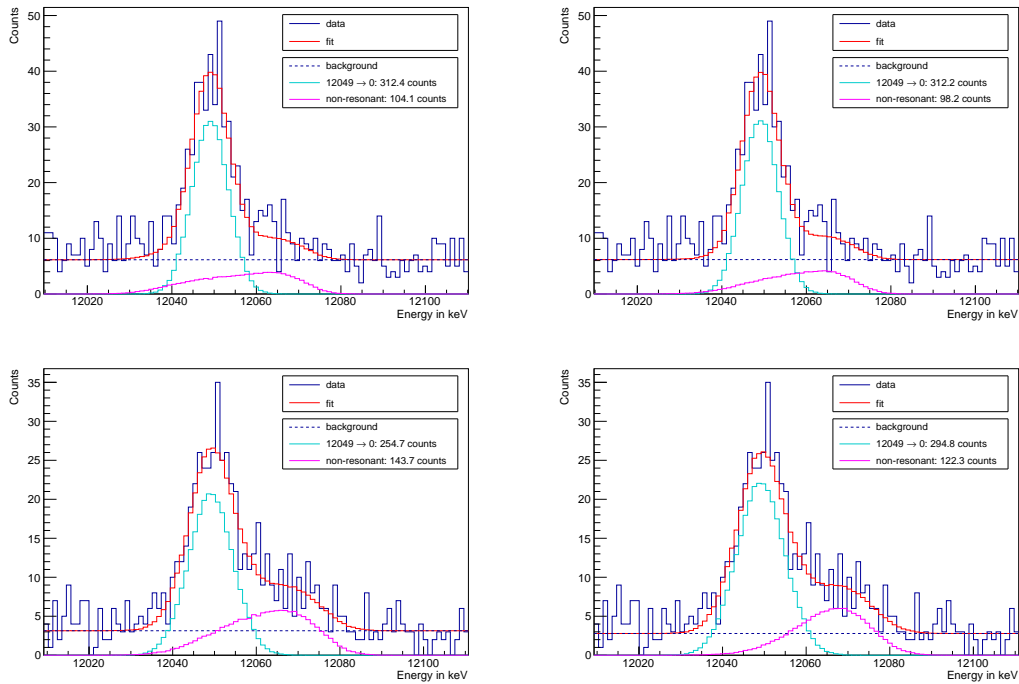


Figure 4.18: Gamma ray spectra in the region of interest for the direct capture to the ground state. The top row shows the measurement at 396.0 keV, the bottom row the measurement at 399.6 keV. The left column uses the target profile as seen before the long run, the right as after the run. “12049→0” is only a short-hand notation, the peak is mostly fed by summing in from the deexcitation cascades of the 12049 keV level.

Table 4.7: Comparison of expected direct capture rate in the two runs, and result of fit to the direct capture to ground state peak.

E_p/keV	309 keV Scan	$N_{\text{calculated}}$	N_{fit}	$N_{\text{fit}}/N_{\text{calculated}}$
396.0	Scan 2	388.1	104.1	0.27
	Scan 3	350.2	98.2	0.28
399.6	Scan 3	509.2	143.7	0.28
	Scan 4	409.7	122.3	0.30

number of observed events in the spectrum are consistently lower. Whilst the absolute numbers depend on whether the target scan before or after the measurement is used as a basis for the yield estimate, the ratio of expected to observed events does not change significantly. This is because the target profiles mainly change in the back (deeper in the target), which affects the direct capture prediction in the energy region that overlaps with the 12049 keV peak. Therefore a change of the prediction in this region is compensated in the fit by an increased number of counts for this peak – in other words: the direct capture component fit is mostly constrained by the counts at higher energies. The ratios of both measurements are compatible within the statistical uncertainty.

The fact that the number direct capture events to the ground state appears consistently smaller than the calculated number of direct capture events could have two explanations. Either a significant fraction of the direct capture goes to excited states, or the S factor for direct capture is smaller than currently assumed.

An analysis of the direct capture to the first excited state is difficult because of the background from $^{23}\text{Na}(p, \gamma)$ resonances that reduces the sensitivity to the DC signal. Figure 4.19 shows the region of interest for the direct capture to the first excited state for the two runs considered here. Apart from the 12076 keV peak that corresponds to the transition from 12049 keV to 1368.672 keV (the gamma ray energy of this transition is given as 12076(4) keV in [16]), both spectra show a smaller structure at around 10705 keV. To guide the eye, a simple model of two gaussian peaks on top of a flat background is fitted and drawn. The direct capture signal, for the assumption that all DC would occur to the first excited state, is then drawn on top of the flat background for a visual comparison. For the run at 396.0 keV, the spectrum is well-described by the background fit, but it is also clear that the sensitivity to the direct capture signal is low due to the background level. For the run at 399.6 keV, the second peak at higher energies comes out broader and is not so well-fitted with a single gaussian. The sensitivity to the DC component is higher for this run because of the reduced background compared to the other run at a lower proton energy. The hypothesis that the smaller peak is not a primary peak is supported by the observation that it did not move to higher energies in the run at 399.6 keV, compared to the run at 396.0 keV (see Figure 4.20). The analysis of this broader structure at 10705 keV for the run at 399.6 keV is ongoing, but making a statement about the DC to the first excited state from this single spectrum is expected to be difficult.

The background situation is even worse for direct capture to higher excited states, which further reduces the sensitivity to these transitions. Measurements with thinner targets could help to reduce the background from $^{23}\text{Na}(p, \gamma)$ resonances, allowing the search for direct capture at least to the first excited state of ^{24}Mg at the highest energies at LUNA. Ultimately a definite statement will be difficult to obtain with the current

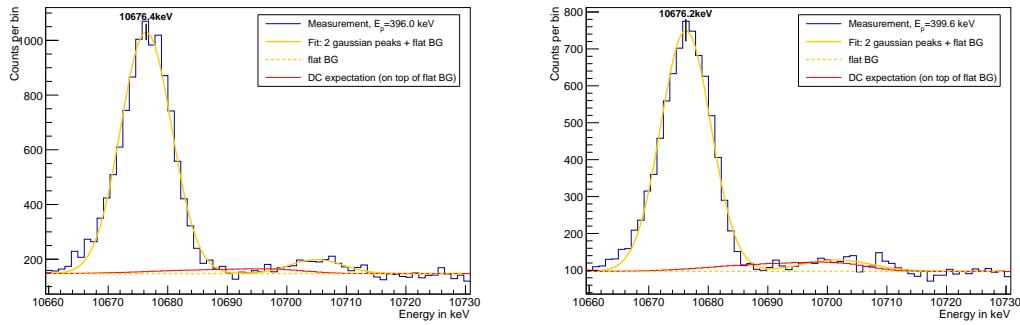


Figure 4.19: Region of interest for $^{23}\text{Na}(p, \gamma)$ direct capture to first excited state of ^{24}Mg for two measurements at 396.0 keV and 399.6 keV proton energy. A simple fit to the signal (two gaussians plus a flat background) is shown in orange, the expectation from direct capture (assuming resonance scan 3 and 100% direct capture to the first excited state) is drawn on top of the flat background.

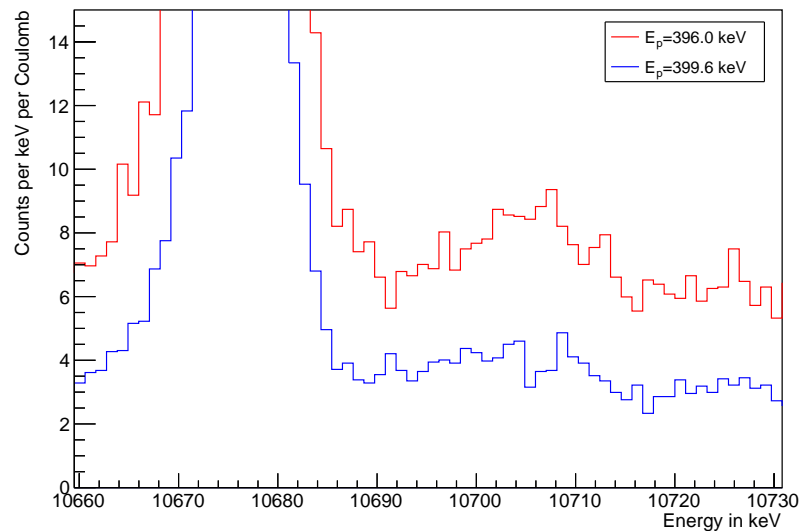


Figure 4.20: Comparison of the gamma ray spectra at proton energies of 396.0 keV and 399.6 keV. The structure at circa 10705 keV does not move with the beam energy. The higher background at lower beam energies is clearly visible.

setup (i. e. targets and accelerator energy range), as there is a very narrow energy range in which the DC to the excited states might be observable. With only a small energy range accessible, the possibility that a part of the observed signal in the ROI for direct capture also contains a contribution of tails of broader $^{23}\text{Na}(p, \gamma)$ resonances at energies higher than 400 keV cannot be excluded. Dedicated measurements of the cross section at higher proton energies would be required, in order to assess the possible influence of resonances at higher energies on the measurements at LUNA. A combination of such measurements at higher energies and possible LUNA data point(s), could potentially isolate the direct capture component of the cross section.

4.2.6 Minor Resonances

Few minor resonances in $^{23}\text{Na}(p, \gamma)$ were studied in single measurements with the HPGe detector. For each of these measurements, the proton energy to be measured was determined from the resonance energy and with the help of a 309 keV resonance scan performed immediately before the measurement, in order to place the measurement of the resonance under study on the expected plateau of the yield curve.

Two measurements at $E_p = 380.0$ keV ($Q = 1.0$ C) and $E_p = 375.0$ keV ($Q = 0.9$ C) were taken to confirm the properties of a resonance at 374.3(4) keV. The strength of this resonance and the branching ratios of four primary transitions are known in literature [17, 16]. The relative uncertainty of the resonance strength is given as 28%. The four known primary transitions were identified in the spectra, and no additional primary transitions were found. Table 4.8 shows the branching ratios derived for these primary transitions by the same method as for the 251 keV resonance. The branching ratios are in agreement with the literature values, with a slight discrepancy for the transition to the 4122.889 keV level, which however still is within the systematic uncertainty range of the measurement. The first run was not used for the determination of the resonance strength, due to an irregular profile in the 309 keV resonance scan preceding the run. The resonance strength was calculated relative to the 309 keV resonance strength, comparing the yield observed in this run with the plateau yield of the 309 keV resonance scan:

$$\omega\gamma(374 \text{ keV}) = \omega\gamma(309 \text{ keV}) \cdot \frac{Y_{\text{measurement}}(374 \text{ keV})}{Y_{\text{plateau}}(309 \text{ keV})} \cdot \frac{374 \text{ keV}}{309 \text{ keV}} \cdot \frac{\varepsilon_{\text{eff.}}(374 \text{ keV})}{\varepsilon_{\text{eff.}}(309 \text{ keV})} \quad (4.6)$$

The yield calculated for the second run results in a resonance strength of 2.1(5) meV, compared to the literature value of 1.4(4) meV. Apart from the 18% relative uncertainty of the 309 keV resonance strength, the main contributions to the uncertainty of the result from this work are the 309 keV resonance scan plateau height and the uncertainty of the detection efficiency.

A measurement at $E_p = 340.0$ keV ($Q = 13.4$ C) was analyzed, searching for gamma

Table 4.8: Results for the branching ratios for the two runs measuring the $E_p = 374$ keV resonance. The uncertainty given for the branching ratios from this work is statistical only.

$E_x \rightarrow$	Run A	Run B	Literature [16]
6010.84	6.3(4)	5.4(5)	5.0(5)
5235.12	25.5(5)	25.5(5)	22.0(10)
4122.889	67.3(6)	67.6(6)	72.0(22)
1368.672	0.9(2)	1.6(2)	1.0(2)

rays from primary transitions corresponding to the $E_p = 338.6$ keV resonance. No branching ratios for the excited state and only an upper limit on the resonance strength were found in literature [17, 16]. The measured spectrum was strongly influenced by the beam-induced background from $^{19}\text{F}(p, \alpha\gamma)$. In the spectrum, a single transition could be identified as a primary transition for the excited state of this resonance. Assuming that this transition to the first excited state of ^{24}Mg is the only primary transition of this resonance state, a resonance strength of $\omega\gamma = 2.7(6) \cdot 10^{-5}$ eV is obtained, compared to a previous upper limit of 10^{-2} eV. The statistical uncertainty from the determination of the number of counts is 8%. Systematic errors include 18% for the reference 309 keV resonance strength, 10% for the detection efficiency, 5% for the plateau yield of the 309 keV resonance, 3% for the stopping power extrapolation, and 3% for the charge collection. However, the background from fluorine bears the risk that primary transitions at lower gamma ray energies were masked, and the value obtained for the resonance strength is underestimated.

In a measurement at $E_p = 292.5$ keV ($Q = 12.8$ C), the four strongest of the 10 primary gamma ray transitions of the excited state [16] corresponding to a resonance at 286 keV proton energy were observed. The statistical uncertainties of these peak areas are large – between 15% and 50%. Neglecting the width of this state of about 2 keV and treating the resonance as narrow, a weighted average of the yield of these gamma lines results in a resonance strength of $63(15) \mu\text{eV}$ (with an error budget similar to the previous resonances, except for a larger statistical uncertainty). The value is compatible with the previous upper limit of $500 \mu\text{eV}$ [17].

4.3 BGO Phase Analysis

4.3.1 Measurements

At energies above the stronger resonances in $^{23}\text{Na}(p, \gamma)$, measurements with the BGO detector are challenging to analyze, because lower-lying resonances can contribute signif-

icantly to the signal, but cannot be resolved with the energy resolution of the detector. In particular the energy region above the 309 keV resonance is difficult, due to the contribution of the 309 keV resonance that has been visible in HPGe measurements even at energies significantly above the plateau region of the 309 keV resonance scan profile. Above 340 keV, the beam-induced background from $^{19}\text{F}(\text{p}, \alpha\gamma)$ increases strongly and the pile-up signal of two $^{19}\text{F}(\text{p}, \alpha\gamma)$ events can significantly contribute to the $^{23}\text{Na}(\text{p}, \gamma)$ region of interest for weak $^{23}\text{Na}(\text{p}, \gamma)$ resonances.

As the energy region above the 309 keV resonance was covered with measurements using the HPGe detector, the BGO detector phase of the experiment focused on the two stronger resonances and the search for the 144 keV resonance. The main purpose of the measurements of the stronger resonance were to monitor the target composition: regular scans of the 309 keV (and occasionally the 251 keV) resonances were performed in between longer measurements. The spectra acquired in these runs were also used to continuously update the energy calibration for the six detector segments, to account for slow changes in the gain or the light yield of the scintillator (which, for example, is sensitive to the temperature of the crystals).

4.3.2 144 keV Resonance

Owing to the expected yields of the order of 10 reactions per Coulomb of protons on target (cf. Table 4.5), the analysis is highly sensitive to any background in the region of interest for $^{23}\text{Na}(\text{p}, \gamma)^{24}\text{Mg}$. As explained in section 3.2, environmental backgrounds were not expected to pose a problem for the sum spectrum signal of the BGO detector. However, beam-induced backgrounds from reactions with Q values larger or comparable to Q of $^{23}\text{Na}(\text{p}, \gamma)^{24}\text{Mg}$ can spoil the signal in the region of interest.

As described in section 4.1, the most critical beam-induced background for this resonance search comes from $^{11}\text{B}(\text{p}, \gamma)^{12}\text{C}$. The reaction has a resonance at a center of mass energy of 148.6(4) keV (proton energy 162.1(4) keV) [66] that, due to its width of 5.3(2) keV (c. m.), has the potential to be relevant at the energy of the resonance under study in $^{23}\text{Na}(\text{p}, \gamma)^{24}\text{Mg}$. This risk is increased by the uncertainty of the $^{23}\text{Na}(\text{p}, \gamma)^{24}\text{Mg}$ resonance energy (cf. Table 1.2): to avoid searching the resonance at a proton energy that is still below the resonance energy, measurements should also cover the upper possible range for the resonance energy. The higher the proton energy is, however, the closer it gets to the boron resonance energy, and thus the beam-induced background is increased.

As a consequence of this energy-dependence, measurements were performed at different proton energies, above and below the energy of the pursued resonance. A number of different targets were used for the measurements, as the targets degraded during the proton bombardment. For the stage of the analysis that is presented here, measurements

with targets that showed a visible beam-induced background contribution from lithium were not considered. An overview of the selected subset of measurements is shown in Table 4.9. Each run was analyzed individually to identify outliers (such as from a significant lithium contribution), and in groups of runs with similar proton energies as shown in the Table.

Table 4.9: Selected measurements for the 144 keV resonance search.

Dataset	Proton Energy / keV	Run	Target	Charge / C
130 (12.8 C)	129.9	2327	Na ₂ WO ₄ -19	2.6
	129.9	2328	Na ₂ WO ₄ -19	10.2
140 (36.2 C)	139.9	2238	Na ₂ WO ₄ -21	14.0
	140.0	2219	Na ₂ WO ₄ -21	14.2
	140.0	3119	Na ₂ WO ₄ -32	4.8
	140.0	3137	Na ₂ WO ₄ -32	2.1
	140.2	3118	Na ₂ WO ₄ -32	1.1
145 (66.4 C)	145.0	1833	Na ₂ WO ₄ -18	2.7
	145.0	1885	Na ₂ WO ₄ -18	11.3
	145.0	1919	Na ₂ WO ₄ -18	9.9
	145.0	2206	Na ₂ WO ₄ -21	8.6
	145.0	2654	Na ₂ WO ₄ -31	7.9
	145.0	2780	Na ₂ WO ₄ -31	9.9
	145.0	2841	Na ₂ WO ₄ -31	10.4
	145.0	4286	Na ₂ WO ₄ -40	5.7
147-148 (66.8 C)	147.0	1938	Na ₂ WO ₄ -18	9.0
	147.0	1998	Na ₂ WO ₄ -20	2.2
	147.0	2010	Na ₂ WO ₄ -20	10.0
	147.0	2022	Na ₂ WO ₄ -20	14.1
	147.0	2266	Na ₂ WO ₄ -19	1.3
	147.0	2294	Na ₂ WO ₄ -19	9.1
	147.9	153	Na ₂ WO ₄ -11	3.2
	147.9	170	Na ₂ WO ₄ -11	13.1
	148.0	3076	Na ₂ WO ₄ -32	4.8
150 (5.4 C)	150.0	3100	Na ₂ WO ₄ -32	5.4

The analysis for the resonance search has to take the background from ¹¹B(p, γ) into consideration and search for a signal (an excess of counts in the region of interest) over this background. As the beam-induced background was seen to vary between targets, and even between runs, the background subtraction had to be done for each run individually.

As the Q value of $^{11}\text{B}(p, \gamma)$ is larger than that of $^{23}\text{Na}(p, \gamma)$, a region of the sum energy spectrum can be defined in the high energy part that is expected to be free of $^{23}\text{Na}(p, \gamma)$ events, and assumed to be dominated by the beam-induced background associated with boron. The excitation energy corresponding to the 161 keV resonance in $^{11}\text{B}(p, \gamma)$ marks the center of this region of interest. The second region is centered around E_x of the 144 keV resonance in $^{23}\text{Na}(p, \gamma)$. The widths of the regions were chosen corresponding to $\pm 3\sigma$ of the energy resolution of the sum energy spectra at these energies. The two regions of interest are illustrated in Figure 4.21 for a spectrum that shows $^{11}\text{B}(p, \gamma)$ only. The numbers of counts in these regions of interest observed in a measurement will be referred to as N_1 ($^{23}\text{Na}(p, \gamma)$ ROI at lower energies) and N_2 (beam-induced background ROI at higher energies).

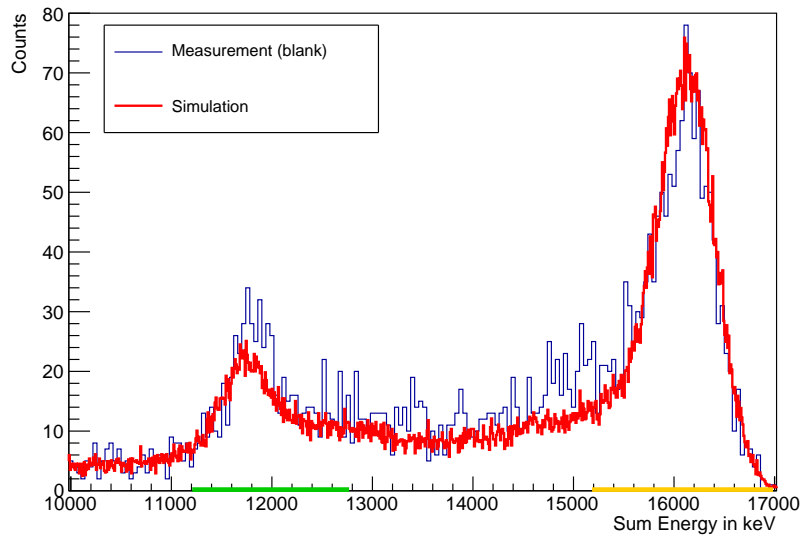


Figure 4.21: Regions of interest in the sum spectrum for the 144 keV resonance search (illustrated for a run with a target without sodium). The orange ROI serves as an estimator for the beam-induced background from boron. The green region of the spectrum corresponds to E_x in ^{24}Mg of the 144 keV resonance.

The number of counts N_2 was assumed to be purely an effect of beam-induced background from $^{11}\text{B}(p, \gamma)$. N_1 is then expected to have contributions from this beam-induced background, and from the signal of $^{23}\text{Na}(p, \gamma)$.

$$N_1 = N_1^{\text{sodium}} + N_1^{\text{boron}} \quad (4.7)$$

$$N_2 = N_2^{\text{boron}} \quad (4.8)$$

As the spectral shape of the background signal can be well-reproduced in the Monte

Carlo simulation, the ratio $N_1^{\text{boron}}/N_2^{\text{boron}} \equiv s$ can be determined from the simulated spectral shape. Knowing this ratio, the influence of the beam-induced background to the number of counts N_1 can be estimated from the observed number of counts N_2 , assuming that N_2 has no other contributions than $^{11}\text{B}(p, \gamma)$.

Considering the spectrum from a single measurement, under the presented assumptions it can be described by two numbers: N_2^{boron} and N_1^{sodium} . The observables N_1 and N_2 can then be derived from equations (4.8) and (4.7), with $N_1^{\text{boron}} = s \cdot N_2^{\text{boron}}$.

To find the two parameters that describe the spectrum best in this model, the likelihood for the observation of N_1 and N_2 given the model parameters N_1^{sodium} and N_2^{boron} can be considered:

$$\mathcal{L}(\{N_1, N_2\} | N_1^{\text{sodium}}, N_2^{\text{boron}}) = P(N_1, N_1^{\text{sodium}} + s \cdot N_2^{\text{boron}}) \cdot P(N_2, N_2^{\text{boron}}) \quad (4.9)$$

Where $P(x, \mu)$ is the probability mass function of the Poisson distribution:

$$P(x, \mu) = \frac{\exp(-\mu) \cdot \mu^x}{x!} \quad (4.10)$$

The number of sodium events N_1^{sodium} is directly related to the strength of the pursued resonance. Written relative to the 309 keV resonance strength, one obtains:

$$N_1^{\text{boron}} = Q \cdot Y(309 \text{ keV}) \cdot \frac{Y(144 \text{ keV})}{Y(309 \text{ keV})} \cdot \eta_1 \quad (4.11)$$

$$= Q \cdot Y(309 \text{ keV}) \cdot \frac{\omega\gamma_{144 \text{ keV}}}{\omega\gamma_{309 \text{ keV}}} \cdot \frac{\varepsilon_{\text{eff.}}(309 \text{ keV})}{\varepsilon_{\text{eff.}}(144 \text{ keV})} \cdot \frac{309 \text{ keV}}{144 \text{ keV}} \cdot \eta \quad (4.12)$$

Here, η_1 is the efficiency, i. e. the probability that a $^{23}\text{Na}(p, \gamma)$ event from the 144 keV resonance yields a count in the region of interest for N_1 . The ratio of the resonance energies emerges from the ratio of the de-Broglie wavelengths in the narrow resonance yield. $Y(309 \text{ keV})$ was derived from the plateau of the 309 keV resonance scan preceding the low-energy measurement. The equation follows from the assumption that the resonance energy is far enough below the proton energy, so that the probed yield of the 144 keV resonance falls in the plateau region of the resonance profile. Although the plateau yields for the 309 keV resonance typically were lower than expected for the nominal yield, the deviation of the ratio of the effective stopping powers is not expected to be great. The robustness of effective stopping power ratios to variations of the stoichiometry have been discussed earlier in this chapter.

In addition to using the number of counts in the $^{23}\text{Na}(p, \gamma)$ region of interest in the sum spectrum as observable N_1 , more complex selection criteria can be applied to get the number of events N_1 . The aim of such cuts is to discriminate background events, in favor of events from $^{23}\text{Na}(p, \gamma)$, to achieve a reduction of the background contribution

to the signal region of interest N_1 . The method that was presented until now will be referred to as "sum energy cut" in the following discussion.

Exploiting the granularity of the detector, a cut that is selective on $^{23}\text{Na}(p, \gamma)$ can be added when defining N_1 as the number of events that have a sum energy in the $^{23}\text{Na}(p, \gamma)$ region of interest, and a an energy deposition in one of the single crystals that corresponds to the 1.37 MeV gamma ray line from the first excited to ground state transition in ^{24}Mg . The probability for such a single crystal energy deposition to occur is much larger for an event in which a single gamma ray of 1.37 MeV is emitted (as for a ^{24}Mg deexcitation passing through the first excited state), than the probability for two gamma rays of larger energies (as from $^{11}\text{B}(p, \gamma)$) to cause this energy deposition in a single crystal by chance. Although this also reduces the efficiency to detect a $^{23}\text{Na}(p, \gamma)$ event as count in N_1 , the stronger reduction of the probability for $^{11}\text{B}(p, \gamma)$ events to pass this cut can enhance the sensitivity to $^{23}\text{Na}(p, \gamma)$ overall. This cut will be referred to as "sum energy plus single energy" or "combined" cut.

There is no information about spin and parity of the excited state in ^{24}Mg that would be populated by the 144 keV resonance in $^{23}\text{Na}(p, \gamma)$, nor are gamma ray branching ratios available for this state. This introduces an uncertainty to the detection efficiency, as the summing efficiency of the BGO detector depends on the gamma ray branchings (e. g. the multiplicity of the cascades) as shown in section 3.3. To estimate the possible range of detection efficiencies, one can consider other levels in ^{24}Mg , which have an energy similar to E_x and for which branching information is available. Considering levels with $E_x > 9$ MeV (moving the ROI for the sum energy according to the level energy) yields a distribution of efficiencies η_1 for the two presented cuts as shown in Figure 4.22. The distributions are fairly broad, as the gamma ray branching schemes of the levels show a large variety. The efficiency of the sum energy cut alone is largely dependent on the average number of gamma rays in the cascades. Levels with strong primary transitions to the ground state or the first excited generally have a larger probability to deposit their full energy, compared to schemes with strong cascades of three or more gamma rays. The efficiency values are in the range between 20% and 60%, with the average at 39.8%. The root mean square for the distribution is 9.0%. The combined cut is designed to be selective on the 1.37 MeV transition in ^{24}Mg , so that the probability to pass this cut strongly depends on the intensity of this transition in the branching scheme. In fact, the efficiencies determined for the levels with known branching information, the efficiency varies in a range between about 5% and 30%, with mean 16.1% and RMS of 6.7%. The mean values of the distributions were used for the following analysis, but the possible variation of the efficiencies has to be taken into account for the interpretation of the results.

A Bayesian approach was used to determine not only the best fit (maximum likeli-

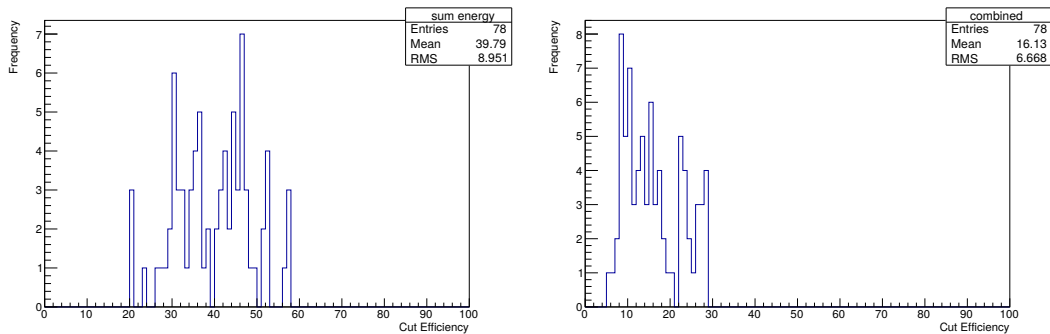


Figure 4.22: Cut efficiency, i. e. probability of $^{23}\text{Na}(p, \gamma)$ events to pass the sum energy cut (left) and the sum energy plus single energy cut (right), see text for details.

hood) values for the resonance strength and the number of boron events, but also determine the probability density function for their values. In the framework of Bayesian statistics (cf. e. g. [68]), a prior probability density function (PDF) is required for the values of the free parameters, to express the current state of knowledge about their possible values. From prior PDFs and data, updated PDFs – the posterior PDFs – are derived, that are interpreted as the probability density function for the “true” value of the parameter:

$$P(\vec{\lambda}|\vec{x}) = \frac{P(\vec{x}|\vec{\lambda}) \cdot P(\vec{\lambda})}{P(\vec{x})} \quad (4.13)$$

Where $\vec{\lambda}$ are the model parameters, and \vec{x} the observables, so that $P(\vec{x}|\vec{\lambda})$ denotes the likelihood of \vec{x} given a parameter set $\vec{\lambda}$ and $P(\vec{\lambda})$ is the prior probability assigned to a parameter set. $P(\vec{x})$ is an abbreviated form of $P(\vec{x}) = \int d\vec{\lambda} P(\vec{x}|\vec{\lambda}) \cdot P(\vec{\lambda})$, so that the posterior probability density function is normalized.

Typically, the calculation of (4.13) is performed numerically. For larger numbers of parameters, i. e. a high-dimensional parameter space, Monte Carlo integration may provide significant advantages in computational speed. For the presented analysis, the Bayesian Analysis Toolkit (BAT [69], version 0.9.4) was used to derive PDFs for the 144 keV resonance strength from the observations in one or multiple measurements. The prior distributions for the resonance strength and the expectation value for the boron counts in the ROI for N_2 for each measurement were assumed to be uniform for non-negative parameter values.

Given a set of measurements, the resonance strength is treated as a common parameter for all measurements, and BAT provides the posterior probability distribution for $\omega\gamma(144\text{ keV})$, given this data set. To characterize the posterior distributions, the mode and the smallest intervals to contain 68% and 95% of posterior probability are used.

The results of the analysis of the single measurements and the data sets are shown in Figures 4.23 for the sum cut and in 4.24 for the combined cut.

The results for the simple sum energy cut show an excess of counts for the data sets at 140, 145, and 147-148 keV. The posterior distributions of the data sets at 130 keV and 150 keV are compatible with a resonance strength of 0 at the 68% confidence level, although the mode of the posterior PDF is non-zero. The analyses of the single measurements within a data set, ordered by mode, do not show any obvious outliers.

With the combined cut on sum and single energies, the modes of the posterior PDFs show a similar pattern as for the simple sum cut. The modes of the three central datasets are, however, at lower values for the resonance strength and the intervals for 95% posterior probability include the value of 0. Again, no single measurement yields results that are very different from the other measurements. Ordering the results by mode, the values increase smoothly.

The results at this stage of the analysis still allow different interpretations. If the excess of counts is seen as a signal from $^{23}\text{Na}(p, \gamma)$, this would have two consequences: first, the resonance energy would appear to be at lower energies than 144 keV, as the excess is already visible in the 140 keV data set. Second, the best-fit values of the resonance strength are about a factor of 2 lower than the current upper limit according to the excess in the analysis after the sum energy cut. Considering the excess in the analysis that combines sum and single energy cut, the best fit values are approximately a factor of 7 lower than the upper limit. Although this factor of 3.5 between the two cuts may appear to be large, the 68% intervals of the PDFs from both analysis could overlap, if certain conditions of the gamma ray branchings of the 144 keV resonance level are met. A branching scheme with a low intensity of the 1.37 MeV transition and a low average multiplicity of the gamma ray cascades, for example, could increase the efficiency for the sum energy cut and decrease the efficiency for the single energy cut, thus moving both results closer together.

Another possible explanation of the excess at the 140 keV dataset and the difference in results between the sum energy cut and the combined cut could be an unaccounted background source that contributes to N_1 , and is more effectively reduced by the combined cut than by the sum energy (as the combined cut is much more selective for $^{23}\text{Na}(p, \gamma)$). At this point, there are two prime candidates for this: One would be a $^{11}\text{B}(p, \gamma)$ source upstream of the target, which – as shown in Figure 4.12 – can reduce the ratio s of the boron signals at 16.11 MeV and 11.67 MeV. Assuming the value for s for a simulated boron source at the target position would then underestimate the boron contribution to the sodium region of interest, leading to an excess of background events that could be misidentified as signal events. Another possible candidate could be a weak contribution from $^7\text{Li}(p, \gamma)$. Targets that have shown a significant contribu-

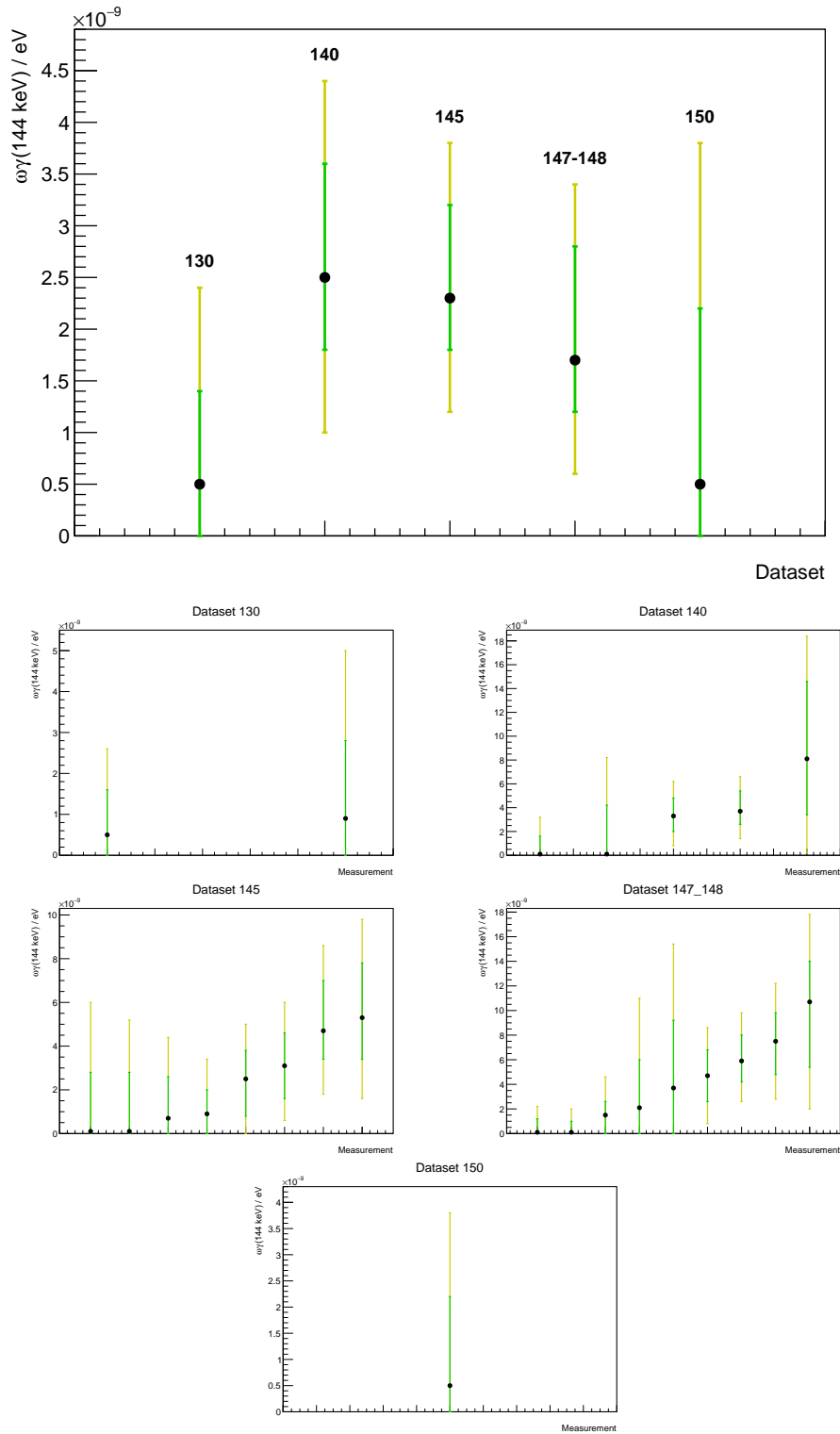


Figure 4.23: Results for the posterior distributions of $\omega\gamma(144 \text{ keV})$ for the sum energy cut as described in the text. Yellow and green bars mark the smallest intervals of 68% and 95% of the posterior PDF. The point is the mode of the PDF. Large plot: results of the combined analysis for each dataset. Smaller plots: results of individual analysis of each measurement for the datasets (ordered by their mode, for easier comparison).

4 Data Acquisition and Analysis

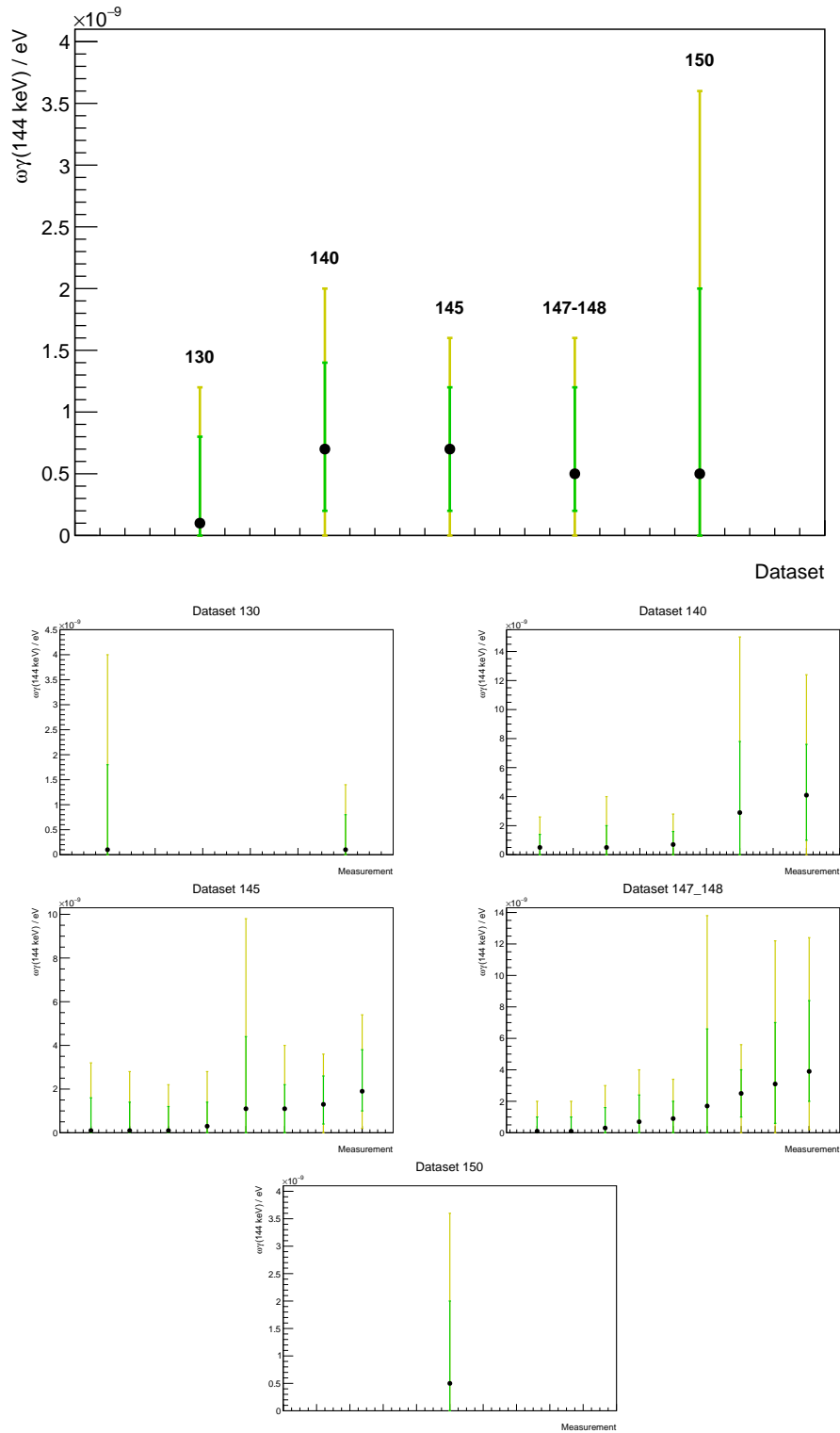


Figure 4.24: Results for the posterior distributions of $\omega\gamma(144 \text{ keV})$ as in Figure 4.23, but for the combined cut of sum energy and single crystal energy deposition as described in the text.

tion of beam-induced background from ${}^7\text{Li}(p, \gamma)$ were discarded for this analysis. As ${}^7\text{Li}(p, \gamma)$ has a stronger transition to the broad state at 3.04 MeV [67], its contribution to the energy region around 14.4 MeV is more significant than to the full energy peak at around 17.4 MeV. A small ${}^7\text{Li}(p, \gamma)$ background, could thus go unnoticed due to a negligible contribution at energies above the ${}^{11}\text{B}$ signal, but still contribute to a broad energy range around 14.4 MeV. As this contribution is located between the ${}^{11}\text{B}(p, \gamma)$ and ${}^{23}\text{Na}(p, \gamma)$ regions of interest, it can also affect the expected ratio between the number of background counts in both ROIs and lead to an underestimation of background in the ${}^{23}\text{Na}(p, \gamma)$ region of interest.

An ideal case to support the detection of the resonance would be the observation of a resonance scan, i. e. a decrease in yield again at higher energies. This, however, is complicated in this case by the finite target thickness that would place an off-resonance run close to the resonances in ${}^{11}\text{B}(p, \gamma)$ (162 keV) and ${}^{18}\text{O}(p, \gamma)$ (150.5 keV)

The next steps of the analysis will thus have to focus on a more detailed study of beam-induced backgrounds. A possibility is to consider the intermediate energy region between the ROIs for ${}^{23}\text{Na}(p, \gamma)$ and ${}^{11}\text{B}$ to check for an excess over the expectation for boron (derived from the 16.7 MeV ROI), which could indicate an influence of either ${}^7\text{Li}$ or ${}^{11}\text{B}$ upstream. A binned fit to the sum energy spectrum above the ${}^{23}\text{Na}(p, \gamma)$ signal will be a generalization of the approach with the multiple regions of interest, trying to maximize the information obtained from the generally low number of counts in this energy region for the low-energy measurements.

Furthermore, the robustness of the analysis against shifts of the energy calibration will need to be studied, as the energy calibration is known to drift slowly in time and can only reliably be checked periodically up to 12 MeV (from the ${}^{23}\text{Na}$ resonance scans). If a major non-linearity or shift in energy calibration above 12 MeV occurred, the regions of interest were misplaced and the predicted background rates would be incorrect.

4.3.3 251 keV and 309 keV Resonances

The 251 keV resonance scans performed with the BGO detector can be used to infer the resonance strength relative to the 309 keV resonance following the same line of argument as for the resonance scans from the HPGe phase: measuring both resonances, one shortly after the other, systematic uncertainties from the target composition are largely reduced and the ratio of the resonance strengths can be determined with a much smaller uncertainty than for an absolute resonance strength determination.

To obtain the BGO detector efficiency for the gamma ray cascades from the deexcitation of the 251 keV resonance level, the primary branchings are required. The adopted branching ratios determined from the HPGe measurements were used. The spectral shape, compared to the 309 keV resonance is shown in Figure 4.25.

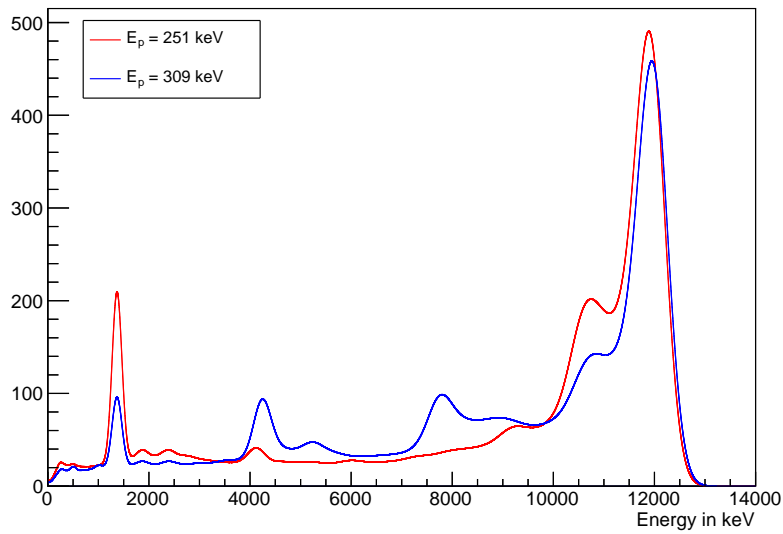


Figure 4.25: Comparison of the simulated sum spectra in the BGO detector for the 251 keV and 309 keV resonances in $^{23}\text{Na}(p, \gamma)^{24}\text{Mg}$, using the gamma ray branching ratios determined in this work for the 251 keV resonance.

An absolute determination of the resonance strength is difficult with only data from this phase of the experiment, due to the lack of an ex situ composition analysis of two “sister” targets as described for the HPGe phase. The ratio of the resonance strengths, however, should be largely independent of that, and provide a cross-check for the determined resonance strength ratio from the HPGe measurements.

5 Conclusions

5.1 Results

The two major resonances in $^{23}\text{Na}(p, \gamma)$ at proton energies of 251 keV and 309 keV were studied with an HPGe detector setup. The gamma ray branching ratios for 7 primary transitions from the ^{24}Mg level corresponding to the 251 keV resonance were determined.

The absolute strengths of the 251 keV and 309 keV resonances were determined from the HPGe measurements and found to be in agreement with the present literature values. The obtained relative uncertainty for the 309 keV resonance strength of 18% is comparable to the uncertainty of the literature value. The uncertainty of the 251 keV resonance strength was reduced from 33% to 18%.

Single measurements of three minor resonances provided previously missing gamma ray branching information or resonance strengths. More precise values, in particular for the strengths, could be achieved in systematic studies, but were not pursued in this work, due to the limited astrophysical impact of these resonances.

As a benefit of the underground location and a massively shielded setup, the BGO detector setup used in this campaign provides a great sensitivity to the study of $(*, \gamma)$ reactions with large Q values thanks to the very low levels of intrinsic and environmental backgrounds in the energy region of interest. The remaining backgrounds are well-understood, and further improvements of the shielding against thermal neutrons have been suggested on this basis, to enhance the sensitivity for the study of other reactions in future experiments.

The search for the 144 keV resonance with the BGO detector was complicated by beam-induced backgrounds, and further analysis of these backgrounds is required to arrive at a reliable conclusion about the strength of this resonance. If the currently observed excess of counts over the background prediction was interpreted as a signal, a resonance strength on the order of 1-2 neV would be the result (depending on the assumptions on the unknown gamma ray branching ratios). Using the results of the combined sum and single energy cut, an upper limit of the resonance strength of 1.5 neV would follow for the average cut efficiency considering neighboring gamma ray branchings, or between 2 and 3 neV for branching ratio assumptions that are less favorable for this cut. A better description and subtraction of the beam-induced backgrounds is expected to improve this situation, and to obtain more strict constraints on the resonance strength.

The direct capture to the ground state of ^{24}Mg has been observed directly for the first time. Its intensity was found to be significantly lower than the total direct capture rate derived from the currently assumed direct capture S -factor from indirect measurements. Due to the influence of the $^{23}\text{Na}(p, \gamma)$ resonances, the sensitivity to the direct capture to the excited states in ^{24}Mg is limited for the proton energies that are achievable at LUNA. The observation of the direct capture motivates future experiments at higher proton energies.

5.2 Astrophysical Reaction Rates

In this section, the possible implications of the results from this work for the reaction rate of $^{23}\text{Na}(p, \gamma)$ will be discussed. To calculate the reaction rate, the input data presented in [4] was used as a reference, only with upper limit of the 144 keV resonance changed to the more recent upper limit from [18].

The approach of [70] was followed to determine the median reaction rates and their uncertainties for the given set of resonances and the non-resonant component. The uncertainty of the reaction rate is obtained by a Monte Carlo approach: Resonance energies, are sampled randomly from a normal distribution according to their uncertainty. Resonance strengths and DC S -factors are sampled from a log-normal distribution, with the square root of the variance corresponding to the quoted uncertainty. In the case of an upper limit for a resonance strength, the value is determined by random sampling from a truncated Porter-Thomas distribution (more precisely the reduced width is sampled from this distribution, see [4] for a detailed discussion), which assigns larger probabilities to smaller resonance strengths. For each randomly sampled set of parameters, the reaction rates are calculated. Repeating the procedure many times, a distribution of reaction rates for a given temperature T is obtained. To characterize the distribution, the median and the 16% and 84% quantiles are quoted. When reading and interpreting these values, the method by which they were obtained has to be kept in mind. The bands which will be presented in the following figures show the median reaction rate and the quantiles as a function of temperature. The bands are divided by the median value of the reaction rate that follows from the reference parameter set described above, to compare the relative deviation between two models more easily. Especially in the case of an upper limit for a resonance, one has to be aware that the lower edge of the band does not present a lower limit on the reaction rate, but merely the value for which the probability to obtain a reaction rate smaller than this is lower than 16%.

The resonance strengths for the 309 keV and 251 keV resonances found in this work were in good agreement with the previous literature value. Hence the median reaction rate is very weakly affected by these findings. The reduced uncertainty of the 251 keV resonance, however, reduces the uncertainty of the reaction rate in the temperature

range where the 251 keV resonance is the dominant contribution, i. e. around 120 MK as demonstrated in Figure 5.1. Clearly visible in this plot is the large uncertainty of the reaction rate in the temperature range between 50 and 90 MK, coming from the contribution of the 144 keV resonance.

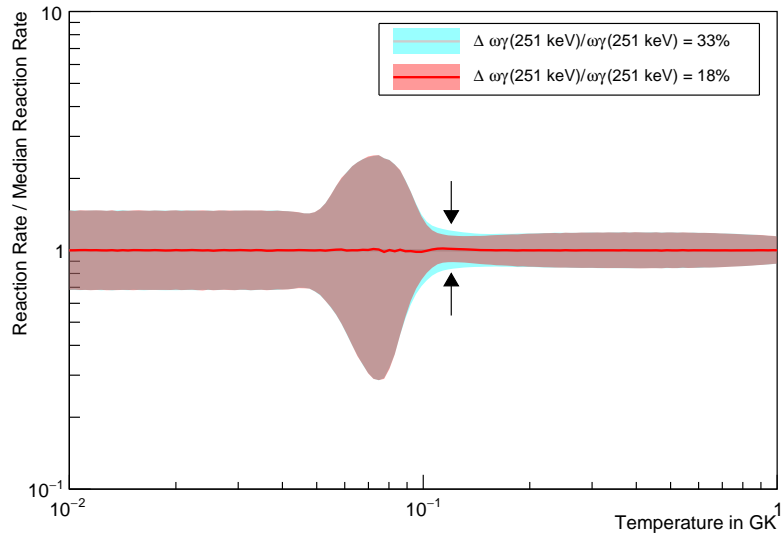


Figure 5.1: Influence of the reduced uncertainty of the 251 keV resonance strength.

As the results of the 144 keV resonance in this work are tentative, the general influence of the 144 keV resonance strength will be discussed, using exemplary values implicated by the analysis presented in the previous chapter. To illustrate a comparison between an upper limit and a (statistically uncertain) hint of a signal, the upper limit and possible observation from [18] are compared in Fig. 5.2. A resonance strength according to the hint would increase the median reaction rate, even though the value for the strength is lower than the given upper limit. This is a consequence of the asymmetric Porter-Thomas distribution that is used for sampling in the case of the upper limit of the resonance strength, and underlines that the interpretation of the median rates and error bands is not always intuitive.

In a similar manner, Figure 5.3. shows a comparison between the reference reaction rate and the rates obtained when assuming an upper limit of 2.0 neV or a value of 0.8(6) neV for the resonance strength. The vales are taken from the discussion of the results of the “combined cut” data analysis of this work. Both solutions would reduce the median reaction rate, compared to the reference reaction rate.

If the observed excess of counts at 140 keV corresponded (at least partially) to a signal from the resonance in $^{23}\text{Na}(p, \gamma)$, the resonance energy would be smaller than currently

5 Conclusions

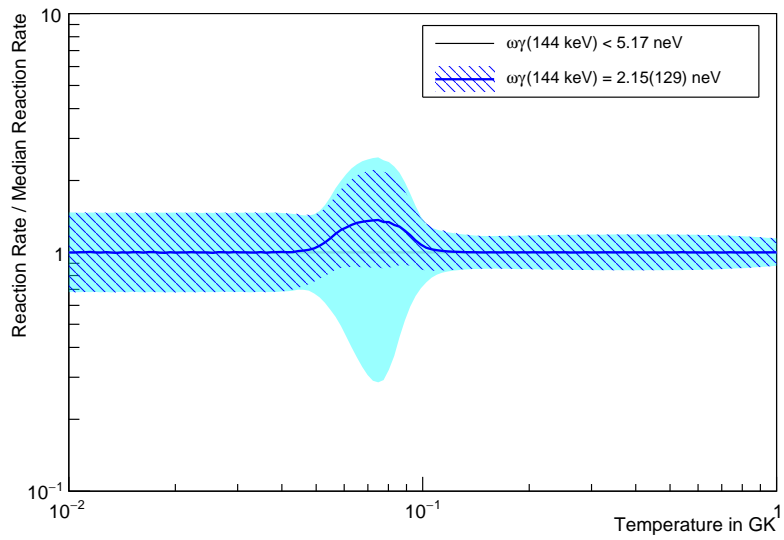


Figure 5.2: Influence of the 144 keV resonance strength on the reaction rate, considering the observed excess of counts in [18] as a signal.

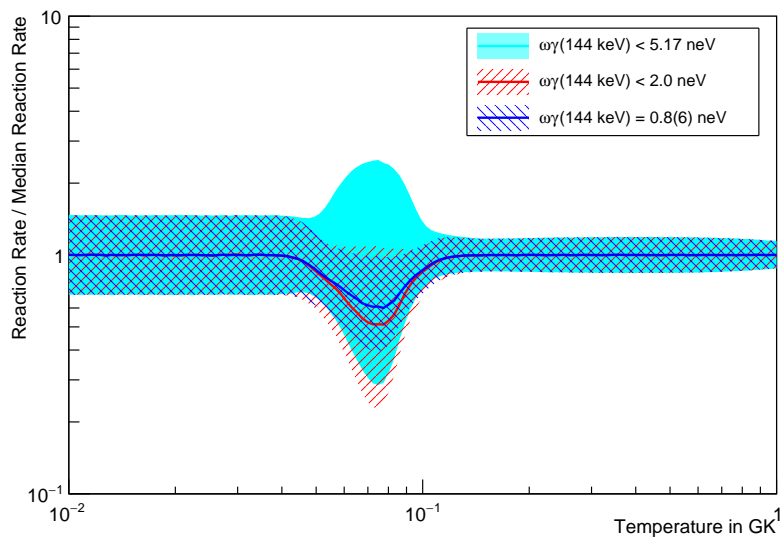


Figure 5.3: Influence of the 144 keV resonance strength on the reaction rate, for two possible interpretations of the analysis of this experiment.

assumed. Figure 5.4 shows the influence of a hypothetical change of the resonance energy from 144 keV to 140 keV (proton energy). The onset of the influence of the resonance is slightly shifted towards lower energies, and the median reaction rate is increased by up to 40%.

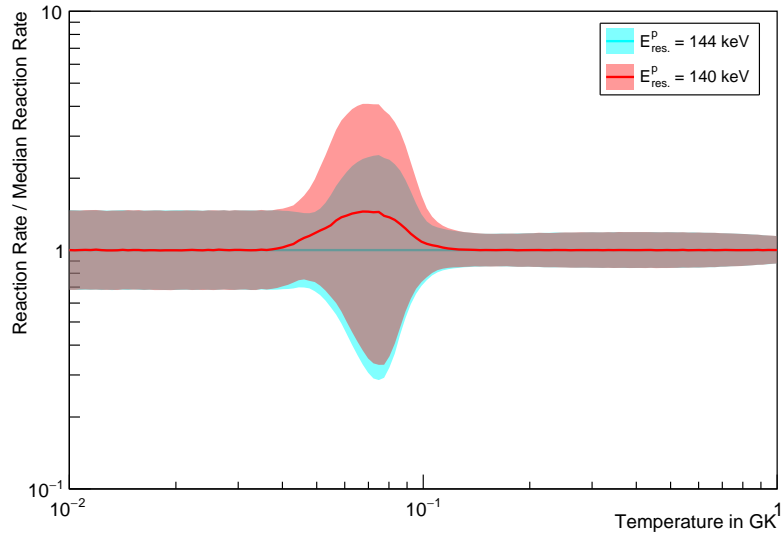


Figure 5.4: Influence of the resonance energy on the reaction rate.

To illustrate the influence of a reduction of the direct capture S -factor, Figure 5.5 shows the reaction rates for the reference case and for a parameter set in which the S -factor is reduced by 50%. As expected, this directly reflects in a reduction of the reaction rate in the lower temperature range where direct capture is the dominant contribution to the cross section. With the weaker direct capture, the temperature range in which the 144 keV resonance is the dominant contribution becomes larger.

The interplay of the direct capture process and the resonance at 144 keV determines the reaction rate for temperatures up to about 80 MK. Their influence motivates a more detailed analysis of the 144 keV search data in this work, and a dedicated study of the direct capture cross section in a separate experiment.

5.3 Outlook

In spite of its large efficiency and low intrinsic and environmental backgrounds, the sensitivity of the BGO detector setup in the 144 keV resonance search was impaired by beam-induced background from mostly $^{11}\text{B}(p, \gamma)$, with its unfavorable spectral shape in the $^{23}\text{Na}(p, \gamma)$ region if interest, and possibly also from $^7\text{Li}(p, \gamma)$. It is hoped that a more detailed analysis of these backgrounds will yield improvements in the sensitivity of this

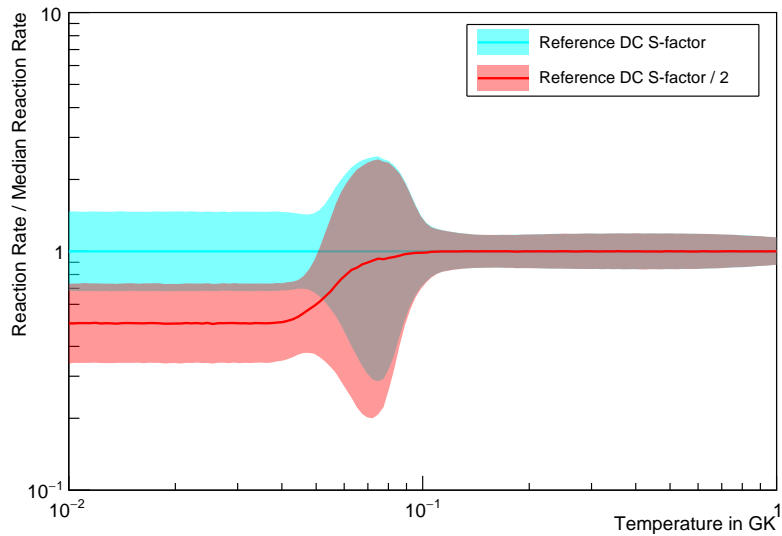


Figure 5.5: Influence of a reduced direct capture S -factor on the reaction rate.

search and help to either firmly establish, or exclude the observation of this resonance in this experiment.

Experimental efforts to reduce the beam-induced $^{11}\text{B}(p, \gamma)$ background were only successful up to a certain background level. A dedicated work to locate and reduce the remaining background contribution could significantly enhance the sensitivity for the 144 keV resonance search in $^{23}\text{Na}(p, \gamma)$, and can also be important for the study of other reactions with this setup.

The missing gamma ray branching ratio information for the excited state in ^{24}Mg that corresponds to the 144 keV resonance introduces a systematic uncertainty to analysis of the measurements obtained with the BGO detector. A determination of these branching ratios (by populating the state using a different channel) would reduce the uncertainty in detection efficiency, and also allow to design more specific event cuts to enhance the sensitivity in the 144 keV resonance search and better distinguish the $^{23}\text{Na}(p, \gamma)$ signal from beam-induced backgrounds. An auxiliary measurement of these branching ratios could thus greatly improve the sensitivity of the experiment presented in this work.

An improvement in the absolute determination of the 251 keV resonance strength was achieved in this experiment, but the main limiting factor for precise absolute measurements was the uncertainty of the target compositions. To reduce these uncertainties in a future experiment, the reproducibility of the target properties or the target analysis techniques would need to be improved.

As discussed in the previous section, the results of this work motivate a dedicated direct

study of the non-resonant cross section. This study will need to include measurements at higher proton energies than those accessible at LUNA400. First measurements of the $^{23}\text{Na}(p, \gamma)$ cross section were already conducted at the Nuclear Structure Lab at the University of Notre Dame, and are to be analyzed to disentangle the various $^{23}\text{Na}(p, \gamma)$ resonances from the direct capture contribution.

Bibliography

- [1] F. Herwig. “Evolution of Asymptotic Giant Branch Stars”. In: *Annual Review of Astronomy and Astrophysics* 43.1 (Sept. 2005), pp. 435–479. DOI: 10.1146/annurev.astro.43.072103.150600.
- [2] C. E. Rolfs and W. S. Rodney. *Cauldrons in the cosmos: nuclear astrophysics*. Theoretical astrophysics. Chicago: University of Chicago Press, 1988.
- [3] C. Iliadis. *Nuclear Physics of Stars*. 1st. Weinheim: Wiley-VCH, 2007.
- [4] C. Iliadis et al. “Charged-particle thermonuclear reaction rates: III. Nuclear physics input”. In: *Nuclear Physics A* 841.1-4 (Oct. 2010), pp. 251–322. DOI: 10.1016/j.nuclphysa.2010.04.010.
- [5] J. F. Ziegler and J. P. Biersack. *SRIM 2013*. <http://srim.org/>, accessed: October 3, 2016.
- [6] R. Longland et al. “Nuclear astrophysics studies at the LENA facility: The gamma-ray detection system”. In: *Nuclear Instruments and Methods in Physics Research Section A: Accelerators, Spectrometers, Detectors and Associated Equipment* 566.2 (Oct. 2006), pp. 452–464. DOI: 10.1016/j.nima.2006.07.006.
- [7] S. Ahlen et al. “Study of penetrating cosmic ray muons and search for large scale anisotropies at the Gran Sasso Laboratory”. In: *Physics Letters B* 249.1 (Oct. 1990), pp. 149–156. DOI: 10.1016/0370-2693(90)90541-D.
- [8] D. Bemmerer et al. “Feasibility of low-energy radiative-capture experiments at the LUNA underground accelerator facility”. In: *The European Physical Journal A* 24.2 (May 2005), pp. 313–319. DOI: 10.1140/epja/i2004-10135-4.
- [9] A. Best et al. “Low energy neutron background in deep underground laboratories”. In: *Nuclear Instruments and Methods in Physics Research Section A: Accelerators, Spectrometers, Detectors and Associated Equipment* 812 (Mar. 2016), pp. 1–6. DOI: 10.1016/j.nima.2015.12.034.
- [10] C. G. Bruno et al. “Resonance strengths in the $^{17,18}\text{O}(p,\alpha)^{14,15}\text{N}$ reactions and background suppression underground: Commissioning of a new setup for charged-particle detection at LUNA”. In: *The European Physical Journal A* 51.8 (Aug. 2015). DOI: 10.1140/epja/i2015-15094-y.

- [11] G. Bellini, C. Brogini, and A. Guglielmetti. “Topical issue on underground nuclear astrophysics and solar neutrinos: Impact on astrophysics, solar and neutrino physics”. In: *The European Physical Journal A* 52.4 (Apr. 2016). DOI: 10.1140/epja/i2016-16088-y.
- [12] M. Wang et al. “The Ame2012 atomic mass evaluation”. In: *Chinese Physics C* 36.12 (Dec. 2012), pp. 1603–2014. DOI: 10.1088/1674-1137/36/12/003.
- [13] C. Rowland et al. “Does an NeNa Cycle Exist in Explosive Hydrogen Burning?” In: *The Astrophysical Journal* 615.1 (Nov. 2004), pp. L37–L40. DOI: 10.1086/425964.
- [14] S. E. Hale et al. “Investigation of the $^{23}\text{Na}(p, \gamma)^{24}\text{Mg}$ and $^{23}\text{Na}(p, \alpha)^{20}\text{Ne}$ reactions via ($^3\text{He}, d$) spectroscopy”. In: *Physical Review C* 70.4 (Oct. 2004), p. 045802. DOI: 10.1103/PhysRevC.70.045802.
- [15] R. G. Izzard et al. “Reaction rate uncertainties and the operation of the NeNa and MgAl chains during HBB in intermediate-mass AGB stars”. In: *Astronomy and Astrophysics* 466.2 (May 2007), pp. 641–648. DOI: 10.1051/0004-6361:20066903.
- [16] N. N. D. Center. *information extracted from the NuDat 2 database*. <http://www.nndc.bnl.gov/nudat2/>.
- [17] P. Endt. “Energy levels of $A = 21-44$ nuclei (VII)”. In: *Nuclear Physics A* 521 (Dec. 1990), pp. 1–400. DOI: 10.1016/0375-9474(90)90598-G.
- [18] J. M. Cesaratto et al. “Measurement of the $E_r^{\text{c.m.}} = 138$ keV resonance in the $^{23}\text{Na}(p, \gamma)^{24}\text{Mg}$ reaction and the abundance of sodium in AGB stars”. In: *Physical Review C* 88.6 (Dec. 2013), p. 065806. DOI: 10.1103/PhysRevC.88.065806.
- [19] M. Uhrmacher et al. “Energy calibration of the 500 kV heavy ion implanter Ionas”. In: *Nuclear Instruments and Methods in Physics Research Section B: Beam Interactions with Materials and Atoms* 9.2 (May 1985), pp. 234–242. DOI: 10.1016/0168-583X(85)90688-3.
- [20] Z. E. Switkowski et al. “Total Yield Measurements in $^{23}\text{Na}(p, \gamma)^{24}\text{Mg}$ ”. In: *Australian Journal of Physics* 28.2 (1975), p. 141. DOI: 10.1071/PH750141.
- [21] B. M. Paine, S. R. Kennett, and D. G. Sargood. “ (p, γ) resonance strengths in the s-d shell”. In: *Physical Review C* 17.5 (May 1978), pp. 1550–1554. DOI: 10.1103/PhysRevC.17.1550.
- [22] B. Paine and D. Sargood. “ (p, γ) Resonance strengths in the s-d shell”. In: *Nuclear Physics A* 331.2 (Nov. 1979), pp. 389–400. DOI: 10.1016/0375-9474(79)90349-X.
- [23] C. Moss. “Excitation energies of levels in ^{23}Na , ^{24}Mg and ^{26}Mg ”. In: *Nuclear Physics A* 269.2 (Oct. 1976), pp. 429–442. DOI: 10.1016/0375-9474(76)90691-6.

- [24] W. Vermeer, D. Pringle, and I. Wright. “Measurements of Γ_γ/Γ for states of ^{24}Mg in the excitation region $10 < E_x < 12\text{ MeV}$ ”. In: *Nuclear Physics A* 485.2 (Aug. 1988), pp. 380–398. DOI: 10.1016/0375-9474(88)90109-1.
- [25] J. M. Cesaratto. “Resonant Proton Capture on ^{23}Na and Elemental Variations in Globular Cluster Stars”. PhD. Chapel Hill: University of North Carolina at Chapel Hill, 2011.
- [26] A. Formicola et al. “The LUNA II 400 kV accelerator”. In: *Nuclear Instruments and Methods in Physics Research Section A: Accelerators, Spectrometers, Detectors and Associated Equipment* 507.3 (July 2003), pp. 609–616. DOI: 10.1016/S0168-9002(03)01435-9.
- [27] A. Boeltzig. “Cross Section Measurements for the $^{23}\text{Na}(p,\gamma)^{24}\text{Mg}$ Reaction at LUNA”. In: *Journal of Physics: Conference Series* 689 (Feb. 2016), p. 012014. DOI: 10.1088/1742-6596/689/1/012014.
- [28] G. F. Knoll. *Radiation Detection and Measurement*. 3rd ed. 2000.
- [29] ORTEC. *Quality Assurance Data Sheet*. Dec. 2001.
- [30] A. M. T. ORTEC. *Quality Assurance Data Sheet*. July 2016.
- [31] A. Boeltzig and A. Best. “Hands on LUNA: Detector Simulations with Geant4”. In: *Proceedings of Science Gran Sasso Summer Institute 2014 Hands-On Experimental Underground Physics at LNGS* (2015).
- [32] C. Casella et al. “A new setup for the underground study of capture reactions”. In: *Nuclear Instruments and Methods in Physics Research Section A: Accelerators, Spectrometers, Detectors and Associated Equipment* 489.1-3 (Aug. 2002), pp. 160–169. DOI: 10.1016/S0168-9002(02)00577-6.
- [33] C. Casella et al. “First measurement of the $d(p,\gamma)^3\text{He}$ cross section down to the solar Gamow peak”. In: *Nuclear Physics A* 706.1-2 (July 2002), pp. 203–216. DOI: 10.1016/S0375-9474(02)00749-2.
- [34] D. Bemmerer et al. “Low energy measurement of the $^{14}\text{N}(p,\gamma)^{15}\text{O}$ total cross section at the LUNA underground facility”. In: *Nuclear Physics A* 779 (Nov. 2006), pp. 297–317. DOI: 10.1016/j.nuclphysa.2006.09.001.
- [35] F. Strieder et al. “The $^{25}\text{Mg}(p,\gamma)^{26}\text{Al}$ reaction at low astrophysical energies”. In: *Physics Letters B* 707.1 (Jan. 2012), pp. 60–65. DOI: 10.1016/j.physletb.2011.12.029.

- [36] V. T. Jordanov and G. F. Knoll. “Digital synthesis of pulse shapes in real time for high resolution radiation spectroscopy”. In: *Nuclear Instruments and Methods in Physics Research Section A: Accelerators, Spectrometers, Detectors and Associated Equipment* 345.2 (June 1994), pp. 337–345. DOI: 10.1016/0168-9002(94)91011-1.
- [37] CAEN. *Application Note AN2508: Digital Pulse Height Analyser - a digital approach to Radiation Spectroscopy*. Sept. 2011.
- [38] S. Agostinelli et al. “Geant4 - a simulation toolkit”. In: *Nuclear Instruments and Methods in Physics Research Section A: Accelerators, Spectrometers, Detectors and Associated Equipment* 506.3 (July 2003), pp. 250–303. DOI: 10.1016/S0168-9002(03)01368-8.
- [39] J. Allison et al. “Geant4 developments and applications”. In: *IEEE Transactions on Nuclear Science* 53.1 (Feb. 2006), pp. 270–278. DOI: 10.1109/TNS.2006.869826.
- [40] S. Carson et al. “Ratio of germanium detector peak efficiencies at photon energies of 4.4 and 11.7MeV: Experiment versus simulation”. In: *Nuclear Instruments and Methods in Physics Research Section A: Accelerators, Spectrometers, Detectors and Associated Equipment* 618.1-3 (June 2010), pp. 190–198. DOI: 10.1016/j.nima.2010.02.128.
- [41] G. Imbriani et al. “S-factor of $^{14}\text{N}(p,\gamma)^{15}\text{O}$ at astrophysical energies”. In: *The European Physical Journal A* 25.3 (Sept. 2005), pp. 455–466. DOI: 10.1140/epja/i2005-10138-7.
- [42] C. Iliadis et al. “Low-energy resonances in $^{25}\text{Mg}(p,\gamma)^{26}\text{Al}$, $^{26}\text{Mg}(p,\gamma)^{27}\text{Al}$ and $^{27}\text{Al}(p,\gamma)^{28}\text{Si}$ ”. In: *Nuclear Physics A* 512.3 (June 1990), pp. 509–530. DOI: 10.1016/0375-9474(90)90084-Y.
- [43] T. A. Lewis. “The reduction of background signal in bismuth germanate scintillators”. In: *Nuclear Instruments and Methods in Physics Research Section A: Accelerators, Spectrometers, Detectors and Associated Equipment* 264.2-3 (Feb. 1988), pp. 534–535. DOI: 10.1016/0168-9002(88)90955-2.
- [44] K. Fukuda and T. Asano. “Radioisotopic Impurity of ^{207}Bi in BGO Scintillators”. In: *RADIOISOTOPES* 46.3 (1997), pp. 161–164. DOI: 10.3769/radioisotopes.46.161.
- [45] D. Bemmerer. “Experimental study of the $^{14}\text{N}(p,\gamma)^{15}\text{O}$ reaction at energies far below the Coulomb barrier”. PhD. Berlin: Technische Universität Berlin, Aug. 2004.

- [46] R. Glasow et al. “Light particle detection by BGO scintillators with photodiode readout”. In: *Nuclear Instruments and Methods in Physics Research Section A: Accelerators, Spectrometers, Detectors and Associated Equipment* 228.2-3 (Jan. 1985), pp. 354–358. DOI: 10.1016/0168-9002(85)90281-5.
- [47] J. Tammen et al. “Quenching comparison of BGO and BSO for heavy ions”. In: *Nuclear Instruments and Methods in Physics Research Section B: Beam Interactions with Materials and Atoms* 360 (Oct. 2015), pp. 129–138. DOI: 10.1016/j.nimb.2015.07.127.
- [48] D. Grigoriev et al. “Incidental radioactive Background in BGO crystals”. In: *Proceedings of the 1st International Workshop “Radiopure Scintillators for EURECA” (RPScint 2008)* (Sept. 2008).
- [49] S. Seuthe et al. “Production and properties of implanted targets”. In: *Nuclear Instruments and Methods in Physics Research Section A: Accelerators, Spectrometers, Detectors and Associated Equipment* 260.1 (Oct. 1987), pp. 33–42. DOI: 10.1016/0168-9002(87)90385-8.
- [50] J. Keinonen et al. “Short lifetimes in ^{24}Mg for test of rotational collectivity in shell-model wave functions”. In: *Nuclear Physics A* 493.1 (Feb. 1989), pp. 124–144. DOI: 10.1016/0375-9474(89)90536-8.
- [51] T. Brown et al. “Properties of ^{23}Na implanted targets”. In: *Nuclear Instruments and Methods in Physics Research Section B: Beam Interactions with Materials and Atoms* 267.19 (Oct. 2009), pp. 3302–3308. DOI: 10.1016/j.nimb.2009.06.122.
- [52] S. Wagner and M. Heitzmann. “Resonanzenergien für den Protoneneinfang II. Natrium”. In: *Zeitschrift für Naturforschung A* 15.1 (Jan. 1960), pp. 74–78. DOI: 10.1515/zna-1960-0111.
- [53] P. Glaudemans and P. Endt. “Gamma-ray branching of energy levels in ^{24}Mg from the $^{23}\text{Na}(p, \gamma)^{24}\text{Mg}$ reaction”. In: *Nuclear Physics* 30 (Feb. 1962), pp. 30–48. DOI: 10.1016/0029-5582(62)90030-5.
- [54] P. Glaudemans and P. Endt. “The $^{23}\text{Na}(p, \gamma)^{24}\text{Mg}$ reaction (II)”. In: *Nuclear Physics* 42 (Mar. 1963), pp. 367–382. DOI: 10.1016/0029-5582(63)90742-9.
- [55] S. Boydell and D. Sargood. “Accurate Branching Ratio Measurements in $^{23}\text{Na}(p, \gamma)^{24}\text{Mg}$ ”. In: *Australian Journal of Physics* 28.4 (1975), p. 369. DOI: 10.1071/PH750369.
- [56] M. Meyer, J. Reinecke, and D. Reitmann. “A study of the $^{23}\text{Na}(p, \gamma)^{24}\text{Mg}$ reaction and the excited states of ^{24}Mg ”. In: *Nuclear Physics A* 185.2 (May 1972), pp. 625–643. DOI: 10.1016/0375-9474(72)90037-1.

- [57] F. W. Prosser et al. “Gamma Radiation from Proton Capture in ^{23}Na ”. In: *Physical Review* 125.2 (Jan. 1962), pp. 594–599. DOI: 10.1103/PhysRev.125.594.
- [58] G. Gyurky. *Private communication*. 2016.
- [59] R. Huszank et al. “Determination of the density of silicon–nitride thin films by ion-beam analytical techniques (RBS, PIXE, STIM)”. In: *Journal of Radioanalytical and Nuclear Chemistry* 307.1 (Jan. 2016), pp. 341–346. DOI: 10.1007/s10967-015-4102-9.
- [60] M. Mayer. *SIMNRA version 6.06*. <http://home.mpcdf.mpg.de/~mam/>, accessed: October 3, 2016.
- [61] F. Munnik. *Analysis Report: Proposal Nr. 15000474*. Helmholtz-Center Dresden-Rossendorf, Aug. 3, 2015.
- [62] F. Munnik. *Private communication*. 2016.
- [63] N. P. Barradas, C. Jeynes, and R. P. Webb. “Simulated annealing analysis of Rutherford backscattering data”. In: *Applied Physics Letters* 71.2 (1997), p. 291. DOI: 10.1063/1.119524.
- [64] F. Munnik. *Analysis Report: Proposal Nr. 16000823*. Helmholtz-Center Dresden-Rossendorf, Sept. 30, 2016.
- [65] S. Croft. “The absolute yield, angular distribution and resonance widths of the 6.13, 6.92 and 7.12 MeV photons from the 340.5 keV resonance of the $^{19}\text{F}(p,\alpha\gamma)^{16}\text{O}$ reaction”. In: *Nuclear Instruments and Methods in Physics Research Section A: Accelerators, Spectrometers, Detectors and Associated Equipment* 307.2-3 (Oct. 1991), pp. 353–358. DOI: 10.1016/0168-9002(91)90204-4.
- [66] F. Ajzenberg-Selove. “Energy levels of light nuclei $A = 11-12$ ”. In: *Nuclear Physics A* 506.1 (Jan. 1990), pp. 1–158. DOI: 10.1016/0375-9474(90)90271-M.
- [67] F. Cecil et al. “Radiative capture of protons by light nuclei at low energies”. In: *Nuclear Physics A* 539.1 (Mar. 1992), pp. 75–96. DOI: 10.1016/0375-9474(92)90236-D.
- [68] P. C. Gregory. *Bayesian logical data analysis for the physical sciences: a comparative approach with Mathematica support*. Cambridge ; New York: Cambridge University Press, 2010.
- [69] A. Caldwell, D. Kollár, and K. Kröninger. “BAT – The Bayesian analysis toolkit”. In: *Computer Physics Communications* 180.11 (Nov. 2009), pp. 2197–2209. DOI: 10.1016/j.cpc.2009.06.026.
- [70] R. Longland et al. “Charged-particle thermonuclear reaction rates: I. Monte Carlo method and statistical distributions”. In: *Nuclear Physics A* 841.1-4 (Oct. 2010), pp. 1–30. DOI: 10.1016/j.nuclphysa.2010.04.008.